Technical University of Munich

TUM School of Natural Sciences

TUM

Defining the roles of Nafion/solvent formulations in copper-assisted CO$_2$ electrolysis

Pan Ding

Complete reprint of the dissertation approved by the TUM School of Natural Sciences

of the Technical University of Munich for the award of the

Doktor der Naturwissenschaften (Dr. rer. nat.)

Contents

Abstract

Electrochemical CO_2 reduction to value-added chemical feedstocks is of tremendous interest for storing chemical energy from renewable sources while reducing CO_2 emissions from human activities. Copper is one of the most effective catalysts for converting carbon dioxide (CO_2) into hydrocarbons or oxygenates, although it suffers from low product selectivity and limited long-term durability. To address this, CO_2 reduction catalyst layers (CLs) are often prepared from inks containing catalyst nanoparticles and organic binders that can improve stability while also impacting the local reaction environment. In this regard, Nafion ionomer, composed of hydrophobic perfluorocarbon backbones and hydrophilic sulfonic acid side chains, is the most widely used additive for preparing CLs for electrochemical CO_2 reduction, but its impact on the performance of CO_2 electrolysis remains poorly understood.

Here, we first systematically investigate the role of the catalyst ink formulation on CO_2 electrolysis using commercial CuO nanoparticles as the model pre-catalyst and carbon paper as a high surface area support. We find that the presence of Nafion is essential for achieving stable product distributions due to its ability to stabilize the catalyst morphology under reaction conditions. Moreover, the Nafion content and solvent composition (water/alcohol fraction) regulate the internal structure of Nafion films, as well as the catalyst morphology, thereby significantly impacting CO_2 electrolysis performance, resulting in variations of C_{2+} product FE by >3×, with C_{2+} FE ranging from 17% to 54% on carbon paper substrates. Using a combination of ellipsometry and *in situ* Raman spectroscopy during CO_2 reduction, we find that such selectivity differences stem from changes to the local reaction microenvironment. In particular, the combination high water/alcohol ratios and low Nafion fractions in the catalyst ink result in stable and favorable microenvironments, increasing the local CO_2/H_2O concentration ratio and promoting high CO surface coverage to facilitate C_{2+} production in long-term CO_2 electrolysis.

Building upon these insights regarding Nafion/solvent formulations, we utilized a systematic methodology to optimize electrochemical CO_2 reduction on planar glassy carbon substrates, which represent another widely used substrate for preparing CLs for electrochemical CO_2 reduction. We demonstrate that by simply tailoring the Nafion/solvent formulations of catalyst slurries, one can modify the properties of Nafion films on CuO-derived catalysts, thereby enabling the CO_2 reduction performance in CO_2 electrolysis to be tuned. With the optimal formulation, efficient mass transport and favorable electrochemical fragmentation of catalyst particles can be realized on glassy carbon substrates, which progressively enhances the production of C_{2+} products with a remarkably high Faradaic efficiency of 87% for over 200 h.

Overall, this work provides insights into the critical role of Nafion binders on optimizing Nafion/solvent formulations as a means of enhancing performance of electrochemical CO_2 reduction systems. These findings highlight the importance of engineering Nafion films to enhance electrochemical performance in varied electrochemical applications.

Zusammenfassung

Die elektrochemische CO_2-Reduktion zu wertschöpfenden chemischen Rohstoffen ist von großem Interesse für die Speicherung chemischer Energie aus erneuerbaren Quellen bei gleichzeitiger Verringerung der CO_2-Emissionen aus menschlichen Aktivitäten. Kupfer ist einer der wirksamsten Katalysatoren für die Umwandlung von Kohlendioxid (CO_2) in Kohlenwasserstoffe oder sauerstoffhaltige Verbindungen, leidet jedoch unter einer geringen Produktselektivität und einer begrenzten Langzeitbeständigkeit. Aus diesem Grund werden CO_2-Reduktionskatalysatorschichten (CLs) häufig aus Tinten hergestellt, die Katalysator-Nanopartikel und organische Bindemittel enthalten, die die Stabilität verbessern und gleichzeitig die lokale Reaktionsumgebung beeinflussen können. In dieser Hinsicht ist Nafion-Ionomer, das aus hydrophoben Perfluorkohlenstoff-Grundgerüsten und hydrophilen Sulfonsäure-Seitenketten besteht, das am häufigsten verwendete Additiv für die Herstellung von CLs für die elektrochemische CO_2-Reduktion, aber seine Auswirkungen auf die Leistung der CO_2-Elektrolyse sind noch wenig bekannt.

Hier untersuchen wir zunächst systematisch die Rolle der Katalysatortintenformulierung bei der CO_2-Elektrolyse unter Verwendung von handelsüblichen CuO-Nanopartikeln als Modell-Präkatalysator und Kohlenstoffpapier als Träger mit großer Oberfläche. Wir stellen fest, dass die Anwesenheit von Nafion für die Erzielung stabiler Produktverteilungen wesentlich ist, da es die Katalysatormorphologie unter den Reaktionsbedingungen stabilisiert. Darüber hinaus regulieren der Nafion-Gehalt und die Lösungsmittelzusammensetzung (Wasser-/Alkoholanteil) die innere Struktur der Nafion-Filme sowie die Katalysatormorphologie, was sich erheblich auf die Leistung der CO_2-Elektrolyse auswirkt, was zu Schwankungen des C_{2+}-Produkts FE um mehr als das Dreifache führt, wobei C_{2+} FE auf Kohlepapiersubstraten zwischen 17 % und 54 % liegt. Mithilfe einer Kombination aus Ellipsometrie und In-situ-Raman-Spektroskopie während der CO_2-Reduktion stellen wir fest, dass solche Selektivitätsunterschiede auf Veränderungen der lokalen

Reaktionsmikroumgebung zurückzuführen sind. Insbesondere die Kombination aus hohen Wasser/Alkohol-Verhältnissen und niedrigen Nafion-Anteilen in der Katalysatortinte führt zu stabilen und günstigen Mikroumgebungen, die das lokale CO_2/H_2O-Konzentrationsverhältnis erhöhen und eine hohe CO-Oberflächenbedeckung fördern, um die C_{2+}-Produktion in der langfristigen CO_2-Elektrolyse zu erleichtern.

Aufbauend auf diesen Erkenntnissen über Nafion/Lösungsmittel-Formulierungen haben wir eine systematische Methodik zur Optimierung der elektrochemischen CO_2-Reduktion auf planaren Glaskohlenstoffsubstraten angewandt, die ein weiteres weit verbreitetes Substrat für die Herstellung von CLs für die elektrochemische CO_2-Reduktion darstellen. Wir zeigen, dass durch einfache Anpassung der Nafion/Lösungsmittel-Formulierungen von Katalysatoraufschlämmungen die Eigenschaften von Nafion-Filmen auf CuO-Katalysatoren verändert werden können, wodurch die CO_2-Reduktionsleistung bei der CO_2-Elektrolyse eingestellt werden kann. Mit der optimalen Formulierung können ein effizienter Massentransport und eine günstige elektrochemische Fragmentierung der Katalysatorpartikel auf Glaskohlenstoffsubstraten erreicht werden, was die Produktion von C_{2+}-Produkten mit einem bemerkenswert hohen Farada-Wirkungsgrad von 87 % über 200 Stunden schrittweise verbessert.

Insgesamt bietet diese Arbeit Einblicke in die kritische Rolle von Nafion-Bindemitteln bei der Optimierung von Nafion/Lösungsmittel-Formulierungen als Mittel zur Steigerung der Leistung elektrochemischer CO_2-Reduktionssysteme. Diese Ergebnisse unterstreichen die Bedeutung der Entwicklung von Nafion-Filmen zur Verbesserung der elektrochemischen Leistung in verschiedenen elektrochemischen Anwendungen.

Chapter 1. Introduction

1.1 Background

The increasing levels of CO_2 in the atmosphere are a significant concern for the environment, as they contribute to climate change and global warming. The Intergovernmental Panel on Climate Change (IPCC) has recommended that global greenhouse gas emissions need to be reduced by 50% by 2030 and reach net-zero by 2050 to limit the increase of global temperatures to 1.5 °C above pre-industrial levels.[1]

One promising approach to decrease CO_2 emissions is through electrochemical CO_2 reduction. This process ideally uses renewable energy sources, such as wind or solar, to convert CO_2 into value-added chemicals and fuels in electrochemical cells containing catalyst-coated electrodes immersed in electrolyte solutions. Electrochemical CO_2 reduction has several advantages over traditional chemical processes. First, it does not require high temperatures and pressures, which reduces the energy consumption and operating costs. Second, it can use renewable electricity sources, which can reduce the environmental impact and carbon footprint of the process. Third, it has potential to sustainably close the carbon cycle by utilizing atmospheric CO_2 as a carbon source. Finally, it can produce a wide range of value-added chemicals and fuels, such as methane, ethylene, formic acid, and ethanol.[2]

Despite this promise, electrochemical CO_2 reduction technology is still in the early stages of development, and there are several challenges that need to be addressed. One of the main challenges is to increase the selectivity of the process to produce specific chemicals and fuels. Another challenge is to develop efficient and stable electrocatalysts that can operate at low voltages and high currents. Additionally, the cost of the materials used in the electrochemical cell needs to be reduced to make the process economically viable.[3,4]

1.2 Motivation

Electrochemical CO_2 reduction to multicarbon products such as ethylene, ethanol, acetate, and propanol is of great interest. Particularly, ethylene is an essential chemical used in the production of various industrial products, such as plastics, rubber, and textiles. The demand for ethylene and other multicarbon products is of great significance, and it is expected to continue to grow in the foreseeable future. According to the International Energy Agency (IEA), global ethylene demand was around 170 million tonnes in 2020, and it is projected to grow at an average annual rate of 3.5% through 2025 (IEA Global Energy Review 2021).[5] However, the traditional techniques for producing ethylene involve the steam cracking of hydrocarbons, such as ethane, propane, and butane, followed by purifying procedures, which are energy-intensive processes that generate significant amounts of greenhouse gases.[6] As a promising alternative, the electrochemical CO_2 reduction process offers a solution to produce ethylene using renewable electricity, while reducing greenhouse gas emissions at the same time.[7,8]

Nevertheless, the intrinsic electrochemical CO_2 reduction process to produce ethylene is not cost-effective and remains challenging, as it requires a high activation energy to produce multicarbon products. This means that the process requires high voltages to drive high current densities, which can result in low energy efficiency and high costs. Additionally, the electrocatalysts used in the process need to be selective and stable to avoid the production of unwanted byproducts.

To address these challenges, researchers have focused on developing efficient and selective electrocatalysts for the electrochemical CO_2 reduction process. Copper (Cu)-based electrocatalysts have shown promise in selectively producing ethylene with high energy efficiency. Researchers have explored numerous approaches to enhance the selectivity and stability of Cu-based electrocatalysts, such as structural engineering and modulation of the local reaction environment. However, highly selective and stable production of specific multicarbon products on Cu-based catalysts remains problematic.[4,9,10]

On the other hand, Nafion, a perfluorinated ionomer, is a widely used additive in preparing electrodes or membranes for many electrochemical applications due to its high proton conductivity, excellent chemical stability, and durability under harsh conditions.[11] When added into catalyst inks for electrode preparation, the Nafion ionomer can act as a stabilizing agent for the electrocatalyst, preventing its degradation and improving its durability. More importantly, the formulation of the catalyst ink in terms of solvent composition and Nafion content can modify the structures and properties (e.g., thickness and porosity) of catalyst layers (CLs), as well as the properties of Nafion itself at the catalyst surface. Previous studies have recognized that interactions between Nafion ionomers and different solvents can alter the connectivity/tortuosity, conductivity, and water uptake of Nafion thin films, enabling the regulation of the environment surrounding the catalyst. It is expected that these variations can have a profound impact on the reaction microenvironment. For example, changes in CL thickness and porosity can significantly affect mass transport and the reaction microenvironment during steady-state operation, thereby influencing the production of multicarbon products in CO_2 electrolysis.[12] However, systematic analyses of the role of catalyst ink formulations on CO_2RR performance characteristics are lacking, and clear design rules for optimization of activity, selectivity, and stability are required.

1.3 Scope of this work

This work aims to systematically investigate the effect of catalyst ink formulations in terms of Nafion content and solvent composition on the basic properties of hybrid Cu/Nafion catalyst layers and their corresponding performance for CO_2 electrolysis, as well as the structural evolution of these catalysts and the local reaction environment under working conditions. With the resulting insights, Nafion/solvent formulations are tailored to enhance the selective and stable production of multicarbon products in CO_2 electrolysis. The main foci can be outlined in four main topics as follows:

1. A fundamental study of the structure and properties of Nafion thin films prepared with different Nafion/solvent formulations,
2. Investigation of the effect of Nafion/solvent formulations on Cu-catalyzed CO_2 electrolysis on carbon paper-based electrodes,
3. Rational design of Nafion/solvent formulations for enhanced production of multicarbon products in Cu-catalyzed CO_2 electrolysis on glassy carbon-based electrodes,
4. Investigation of underlying mechanisms by which Nafion/solvent formulations impact Cu-catalyzed CO_2 electrolysis.

First, the fundamentals of electrochemical CO_2 reduction will be introduced in Chapter 2, in particular highlighting the current strategies developed for enhancing CO_2 electrolysis and the importance of copper (Cu)-based catalysts for CO_2 electrolysis. Considerable attention has been given to devising methods for achieving selective and efficient synthesis of specific products in CO_2 electrolysis. In addition to optimizing the electrochemical cell configuration, such efforts typically focus on designing catalyst materials with tailored structures and modifying the local reaction environment. These approaches will be discussed in Section 2.2. Next, the importance of the electrochemical CO_2 reduction on Cu is underlined. By summarizing the performance characteristics of state-of-art Cu-based catalysts,

the problems concerning limited activity, low selectivity, and poor durability are introduced in Section 2.3.

Chapter 3 presents a comprehensive overview of Nafion, covering its origin, structure, morphology, and properties. Additionally, an introduction is provided on the use of Nafion in CO_2 electrolysis. Generally, the information from the first three sections of Chapter 3 indicates that the structure and properties of Nafion can be greatly influenced by Nafion/solvent formulations (namely, the Nafion content and solvent composition of Nafion dispersions). These critical dependencies comprise several aspects, including the dispersion behavior of Nafion ionomers in liquid solvent, as well as the morphology, structure, and corresponding properties (e.g., proton and water transport) of prepared Nafion films or membranes. This body of knowledge has therefore led to the utilization of Nafion in various electrochemical applications, and particularly, inspire researchers to modulate the local reaction environment on catalyst surfaces using Nafion films to improve the performance of CO_2 electrolysis (Section 3.4).

Having introduced the fundamentals and importance of both electrochemical CO_2 reduction and Nafion, the mains results of this work are presented in Chapters 4 to 6. Briefly, these chapters detail systematic investigations of the effects of Nafion/solvent formulations on pure Nafion films, catalyst layers, and the performance of CO_2 electrolysis in terms of activity, selectivity, and stability on two commonly used substrates (i.e., carbon paper and glassy carbon). In addition, the mechanisms of how Nafion/solvent formulations affect the structural evolution of Cu catalysts and the local reaction environment on Cu surfaces in the course of CO_2 electrolysis are studied by the combination of *ex situ* structural characterization methods and *in situ* Raman spectroscopy.

In Chapter 4, we focus on the effect of Nafion/solvent formulations on the structure and properties of casted Nafion thin films on Si substrates. First, a review of Nafion/solvent formulations employed for the production of catalyst inks in recent literature concerning CO_2 electrolysis is presented. As a result, we establish that the reported formulations are mostly empirically chosen and currently there exist no established guidelines for rational usage of Nafion and solvent mixtures in

preparing catalyst inks. To overcome this important knowledge gap, a systematic investigation of the influence of Nafion/solvent formulations (i.e., Nafion weight content and water volume fraction in mixed water-isopropanol solvents) on casted Nafion thin films on Si substrates is carried out, which comprises a complementary set of characterization methods aimed at examining how Nafion/solvent formulations impact the properties and structure of the resulting Nafion films.

As a next step, the research focus moves from pure Nafion films to Nafion-coated catalyst layers incorporating commercial CuO nanoparticles as the model catalyst. In Chapter 5, the effects of Nafion/solvent formulations on Cu-catalyzed CO_2 electrolysis on carbon paper substrates are systematically investigated from the following perspectives: the fundamental properties of the catalyst layers, the CO_2 electrolysis performance (activity, selectivity, and stability), and the local reaction environment during operation (local concentration of CO_2 and H_2O, and surface adsorption of intermediates). Our results suggest that the Nafion/solvent formulations used for preparing catalyst inks in CO_2 electrolysis significantly influence the activity, selectivity, and stability of the electrochemical CO_2 reduction process. The impact of Nafion on the reaction outcomes is pronounced and includes three major aspects: the evolution of catalyst structure, modulation of local microenvironment, and accumulation of surface adsorbates. The use of high-water content of 50-75 vol.% in catalyst inks is found to optimize the quality of Nafion films for improved CO_2 electrolysis performance. Although this study focused on carbon paper-based electrodes, it is hypothesized that the dependence of ink formulations on catalyst performance characteristics will also be observed on other supports, such as commonly investigated glassy carbon substrates.

In Chapter 6, we extend our major findings obtained on carbon paper-based electrodes to glassy carbon-based ones. The impact of Nafion/solvent formulations on Cu-catalyzed CO_2 electrolysis is first examined again on glassy carbon substrates. Interestingly, we find markedly different dependencies of CO_2 reduction performance on the catalyst ink formulations on the two different substrates. Nevertheless, the performance of CO_2 electrolysis on glassy carbon is also greatly affected by tuning the catalyst ink formulations. Finally, the optimal formulation is

14

determined for the glassy carbon-based electrode, which is then subject to long-term CO_2 electrolysis over a period of 200 h. The robust durability of the catalyst is confirmed by post-reaction structural characterization and the constantly improving selectivity for multicarbon products is monitored over 200 h. Moreover, the selectivity of ethylene production is constantly enhanced throughout 200 h due to the electrochemical fragmentation of Cu nano-catalysts. These results successfully demonstrate the concept of engineering Nafion/solvent formulations for enhanced production of multicarbon products in CO_2 electrolysis and provide a basis for rational tuning of reaction outcomes in hybrid ionomer/catalyst layers.

Chapter 2. Overview of electrochemical CO_2 reduction

Electrochemical CO_2 reduction represents a promising approach to convert CO_2 molecules into value-added chemical feedstocks and fuels using green electricity generated from various renewable energy sources such as solar, wind, and tidal. In this section, the fundamentals of CO_2 electrolysis are first introduced, after which a literature review regarding strategies that have been developed for enhancing CO_2 electrolysis and copper (Cu)-based catalysts for CO_2 electrolysis is provided.

2.1   Fundamentals of CO_2 electrolysis

It is noted that throughout this thesis, CO_2 electrolysis exclusively refers to the redox reaction consisting of the electrochemical CO_2 reduction reaction (denoted as CO_2RR) and the water oxidation reaction (i.e., oxygen evolution reaction, OER), carried out in aqueous electrolytes.

2.1.1 Basic properties of CO_2

Carbon dioxide, with the chemical formula CO_2, is a chemical compound consisting of a carbon atom covalently double bonded to two oxygen atoms. At room temperature and standard pressure, it exists as a gas. In its equilibrium geometry, the carbon dioxide molecule exhibits linear and centrosymmetric symmetry and, thus, lacks an electric dipole moment (Fig. 2.1). The length of the carbon-oxygen bond in CO_2 is 116.3 pm, which is significantly shorter than the average length of a single C-O bond, which is approximately 140 pm, and shorter than most other multiply-bonded C-O functional groups, such as carbonyls. More importantly, the highly stable molecular structure of CO_2 molecules introduces a large

thermodynamic barrier for the CO_2 reduction reactions, which is further discussed in Section 2.1.2.

Figure 2.1 (**a**) The chemical formula of carbon dioxide, CO_2. (**b**) The space-filling model of a single CO_2 molecule.

While transparent to visible light, CO_2 absorbs infrared radiation as a consequence of excited asymmetric vibrational modes that possess dipole moments. Since these vibrational transitions lie within the range of Earth's blackbody emission spectrum, CO_2 acts as a powerful greenhouse gas in the atmosphere. Currently, it is a trace gas present in Earth's atmosphere, accounting for a concentration of approximately 0.04% by volume (or 421 ppm, based on data as of Feb 2023). Nevertheless, this value represents a drastic increase of CO_2 concentration in the atmosphere compared to levels of ~280 ppm since the beginning of industrialization. The primary cause is the combustion of fossil fuels, which is also the main contributor to climate change. In addition, CO_2 is soluble in water and upon dissolution forms carbonate and bicarbonate ions (HCO_3^-), leading to ocean acidification as atmospheric CO_2 concentrations increase. The aqueous solubility of CO_2 (34 mmol L^{-1}, 300 K, neutral pH) is dependent on several factors, including temperature, pressure, and the presence of other solutes.[13,14] However, one of the most significant factors affecting CO_2 solubility in water is pH. At lower pH values (acidic conditions), the solubility of CO_2 in water is increased. This is because when CO_2 dissolves in water, it forms carbonic acid (H_2CO_3), which can further dissociate into protons (H^+) and HCO_3^-:

$$CO_2 + H_2O \leftrightarrow H_2CO_3 \leftrightarrow H^+ + HCO_3^- \qquad 2.1$$
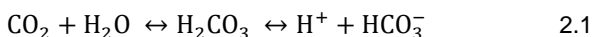
At lower pH, the equilibrium of this reaction is shifted to the right, resulting in the formation of more carbonic acid and an increase in the concentration of dissolved CO_2.

Conversely, at higher pH values (alkaline conditions), the solubility of CO_2 in water is decreased. This is because, under alkaline conditions, bicarbonate ions can further dissociate to form carbonate ions (CO_3^{2-}):

$$2HCO_3^- \leftrightarrow CO_2 + H_2O + CO_3^{2-} \qquad\qquad 2.2$$
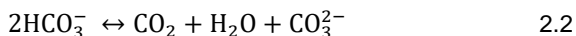
This shifts the equilibrium of the reaction to the left, reducing the concentration of dissolved CO_2. In summary, the aqueous solubility of CO_2 is positively correlated to the acidity of the solution, and inversely correlated to the alkalinity of the solution.

2.1.2 Introduction to CO_2 electrolysis

2.1.2.1 Thermodynamics

The electrochemical CO_2 reduction reaction is the cathodic reduction reaction of a complete redox process and is usually coupled with an anodic oxidation reaction. It should be noted that dissolved CO_2 molecules rather than bicarbonate or carbonate ions are subject to the electrochemical CO_2 reduction reaction at the cathode in aqueous electrolytes.[15] At the cathode, CO_2 molecules utilize electrons (e^-) and H^+ or water (H_2O) to produce various products (Reaction 2.3 and 2.4):

$$x CO_2 + n H^+ + n e^- \rightarrow \text{product} + y H_2O \quad \text{(under acidic conditions)} \qquad 2.3$$

$$x CO_2 + n H_2O + n e^- \rightarrow \text{product} + y OH^- \text{(under alkaline conditions)} \quad 2.4$$
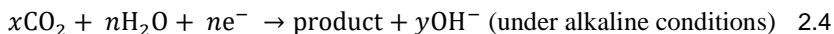
Meanwhile, at the anode, water molecules or hydroxide ions (OH^-) lose electrons and are oxidized into oxygen (Reaction 2.5 and 2.6):

$$2H_2O \rightarrow 4e^- + 4H^+ + O_2 \quad \text{(under acidic conditions)} \qquad 2.5$$

$$4OH^- \rightarrow 4e^- + 2H_2O + O_2 \quad \text{(under alkaline conditions)} \qquad 2.6$$
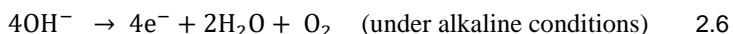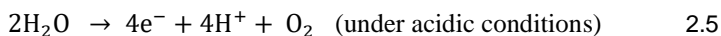
In CO_2 reduction to hydrocarbons, aldehydes, and alcohols on Cu, CO plays a crucial role as an intermediate (Reaction 2.7 and 2.8):

$$x\text{CO} + n\text{H}^+ + n\text{e}^- \rightarrow \text{product} + y\text{H}_2\text{O} \quad \text{(under acidic conditions)} \qquad 2.7$$

$$x\text{CO} + n\text{H}^+ + n\text{e}^- \rightarrow \text{product} + y\text{H}_2\text{O} \quad \text{(under alkaline conditions)} \qquad 2.8$$
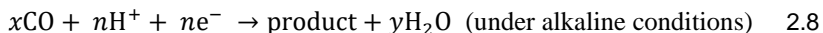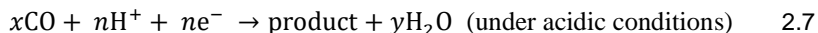
Therefore, CO electroreduction (COR) is an important reaction and the equilibrium potentials for COR to various products are of interest as well.

Table 2.1 Summarized equilibrium potentials of reactions involved in CO_2 electrolysis: the oxygen evolution reaction (OER), the hydrogen evolution reaction (HER), and electrochemical CO_2/CO reduction reactions to various products.

Reaction formulation	E^0 (V vs RHE)	Product
$2H_2O \rightarrow O_2 + 4H^+ + 4e^-$	1.23	Oxygen
$2H^+ + 2e^- \rightarrow H_2$	0	Hydrogen
$CO_2 + 2e^- + 2H^+ \rightarrow HCOOH_{(aq)}$	-0.12	Formic acid
$CO_2 + 2e^- + 2H^+ \rightarrow H_2O + CO_{(g)}$	-0.10	Carbon monoxide
$CO_2 + 6e^- + 6H^+ \rightarrow H_2O + CH_3OH_{(g)}$	0.03	Methanol
$CO_2 + 8e^- + 8H^+ \rightarrow 2H_2O + CH_{4(g)}$	0.17	Methane
$2CO_2 + 2e^- + 2H^+ \rightarrow (COOH)_{(s)}$	-0.47	Oxalic acid
$2CO_2 + 8e^- + 8H^+ \rightarrow 2H_2O + CH_3COOH_{(aq)}$	0.11	Acetic acid
$2CO_2 + 10e^- + 10H^+ \rightarrow 3H_2O + CH_3CHO_{(aq)}$	0.06	Acetaldehyde
$2CO_2 + 12e^- + 12H^+ \rightarrow 3H_2O + C_2H_5OH_{(aq)}$	0.09	Ethanol
$2CO_2 + 12e^- + 12H^+ \rightarrow 4H_2O + C_2H_{4(g)}$	0.08	Ethylene
$2CO_2 + 14e^- + 14H^+ \rightarrow 4H_2O + C_2H_{6(g)}$	0.14	Ethane
$3CO_2 + 16e^- + 16H^+ \rightarrow 5H_2O + C_2H_5CHO_{(aq)}$	0.09	Propionaldehyde
$3CO_2 + 18e^- + 18H^+ \rightarrow 5H_2O + C_3H_7OH_{(aq)}$	0.10	Propanol
$CO + 6e^- + 6H^+ \rightarrow H_2O + CH_{4(g)}$	0.26	Methane
$2CO + 8e^- + 8H^+ \rightarrow H_2O + C_2H_5OH_{(aq)}$	0.19	Ethanol
$2CO + 8e^- + 8H^+ \rightarrow 2H_2O + C_2H_{4(g)}$	0.17	Ethylene

Table 2.1 summaries the equilibrium potentials of various reactions that can be involved in CO_2 electrolysis.[4] The equilibrium potentials for an electrochemical

CO_2 reduction reaction to various gas and liquid products are calculated using the Nernst equation, which relates the equilibrium potential to the standard reduction potential (E^o), the gas constant (R, at standard atmospheric pressure $R = 8.314$ J mol^{-1} K^{-1}), the temperature (T in Kelvin), and the concentrations of the reactants ([reactant]) and products ([product]).

The general form of the Nernst equation for a reaction involving n electrons is:

$$E = E^o - \frac{RT}{nF}\ln Q \qquad\qquad 2.9$$

where Q is the reaction quotient, which is the ratio of the concentrations of the products to the concentrations of the reactants raised to their stoichiometric coefficients, n is the number of electrons transferred in the reaction, and F is Faraday's constant of 96485 C mol^{-1}. The standard reduction potential can be derived from the Gibbs free energy change (ΔG^o) of the redox reaction, using the equation:

$$E^o = -\frac{\Delta G^o}{nF} \qquad\qquad 2.10$$

The value of ΔG^o can be obtained from thermodynamic tables or can be calculated using the standard enthalpy and entropy changes of the reaction.

Notably, the equilibrium potential for electrochemical CO_2 reduction reactions is commonly reported relative to the standard hydrogen electrode (SHE) or the reversible hydrogen electrode (RHE). The RHE is a widely used reference potential for electrochemical reactions in aqueous solutions, and it is preferred for CO_2 reduction reactions since HER can compete with the CO_2 reduction reaction on the surface of the electrode. The equilibrium potential for electrochemical CO_2 reduction reactions relative to RHE can be calculated as follows:

$$E_{vs\ RHE} = E_{vs\ SHE} + \Delta E(\text{SHE} - \text{RHE}) \qquad\qquad 2.11$$

where ΔE(SHE-RHE) is the potential difference between SHE and RHE, which is approximately 0.059 V at 25 °C.

2.1.2.2 Electrochemical cells

There are several types of electrochemical cells that can be used for CO_2 electrolysis, each with its own advantages and disadvantages. Three common types of cells used for CO_2 electrolysis are H-type cells, flow cells, and membrane electrode assemblies (MEAs, Figure 2.2).
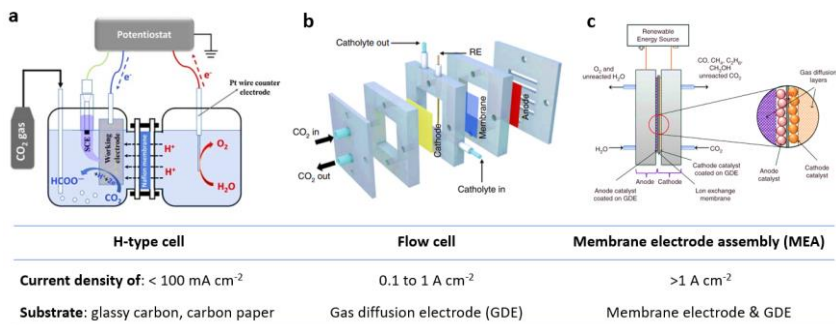

H-type cell	Flow cell	Membrane electrode assembly (MEA)
Current density of: < 100 mA cm^{-2}	0.1 to 1 A cm^{-2}	>1 A cm^{-2}
Substrate: glassy carbon, carbon paper	Gas diffusion electrode (GDE)	Membrane electrode & GDE

Figure 2.2 Comparison of three different electrochemical cell types, namely (**a**) H-type cell, (**b**) flow cell, and (**c**) membrane electrode assembly (MEA). Along with the cell configuration, the typical operating current density and the substrate used for the working electrode are provided in the table. Reproduced from Ref.[16–18]

The H-type cell is a simple and widely used cell for fundamental analysis of CO_2 electrolysis performance (Figure 2.2a). It typically consists of two compartments separated by an ion exchange membrane, with the anode in one compartment and the cathode, usually accompanied by a reference electrode, in the other. The working electrodes, namely the cathodes, are typically made of a conductive material, such as carbon, and are coated with catalyst materials to facilitate CO_2RR. The anode compartment is typically equipped with a counter electrode, such as a platinum wire/mesh/foil electrode. Both compartments are filled with electrolytes, which are normally aqueous buffer solutions, and are bubbled with CO_2 gas to achieve CO_2 saturation in the electrolyte. Buffer solutions are frequently used in electrolysis because they help to maintain a stable pH and can also help to prevent corrosion of the electrodes during electrolysis. In CO_2 electrolysis, bicarbonate or carbonate buffer solutions are most commonly used.

In the H-type cell, control of the reaction conditions is relatively straightforward. For example, the flow rate of CO_2 and the composition of the electrolyte can be easily controlled. However, the mass transfer of CO_2 to the cathode surface can be limited in the H-type cell, which can reduce the efficiency of the process. To improve mass transfer of CO_2 to the cathode surface, electrode materials and catalysts with different morphologies, as well as different electrode geometries, can be used. In addition, given the rather low solubility of CO_2 gas in aqueous electrolytes,[19] the CO_2 availability to catalysts can be severely limited at high operational current densities, thus restricting the activity of CO_2 electrolysis in H-type cells. For example, the measured current density in H-type cells is usually less than 100 mA cm^{-2}.[20] Moreover, H-type cells are normally limited to near-neutral operation for CO_2 electrolysis due to the reduced CO_2 solubility under alkaline conditions, as described before in Reaction 2.2. In brief, the H-type cell is a relatively simple and cost-effective cell for CO_2 electrolysis, making it a popular choice for many fundamental studies. However, its efficiency may be limited, and other types of cells, such as flow cells and membrane electrode assemblies, may be more suitable for certain applications.

Flow cells are typically designed with two porous gas-diffusion electrodes (GDEs) separated by a membrane, with electrolytes flowing between the electrodes (Figure 2.2b). The CO_2 is fed into the cell through the cathode compartment, and the flow rate can be adjusted to optimize the reaction conditions. Notably, on GDEs catalysts can directly utilize CO_2 at a solid-liquid-gas, namely solid catalyst-liquid electrolyte-gaseous CO_2, three-phase interface owing to the porous microstructures of the gas diffusion layers (GDLs). In this case, the activity of CO_2RR would not be limited by the poor solubility of CO_2 in aqueous electrolyte. Instead, the current density of CO_2 electrolysis can be enhanced to ~1 A cm^{-2}, with mass transport limitations eliminated and the large surface area of such porous electrodes providing an abundant loading of active sites.[21] The flow of the electrolyte also provides a continuous supply of fresh reactants to the electrode surface, which can increase the reaction rate and improve the product selectivity. In addition, the flow of the electrolyte can help to remove reaction products from

the electrode surface, which can prevent the accumulation of reaction intermediates and increase the stability of the process.

The use of alkaline aqueous electrolytes, such as potassium hydroxide (KOH) and sodium hydroxide (NaOH) solutions, is a common practice in CO_2 electrolysis using flow cells. This approach provides a significant advantage, as basic electrolytes can reduce the concentration of protons (H^+) in the electrolyte, thus minimizing the competing hydrogen evolution reaction (HER) and promoting CO_2 reduction reaction (CO_2RR). However, long-term operation of the gas diffusion electrodes (GDEs) in these cells often leads to flooding problems, as electrolytes can leak into the gas diffusion chambers and disrupt the three-phase interface, ultimately interrupting the CO_2 electrolysis process. Additionally, the residual CO_2 molecules at the interface tend to react with KOH or NaOH to form solid carbonate or bicarbonate salts, which gradually obstruct the porous structures of the GDEs and impede CO_2 gas diffusion.[20]

The membrane electrode assembly (MEA) has shown promise as an effective and efficient method for highly efficient CO_2 electrolysis (Figure 2.2c). The MEA for CO_2 electrolysis has a configuration resembling that of a proton exchange membrane-based water electrolyzer or a fuel cell. Ideally, in a zero-gap MEA setup the polymer membrane is sandwiched between the anode and cathode, resulting in minimized ohmic resistance and improved energy efficiency. The scaling up of the electrolyzer is made easy by stacking the MEA or expanding the electrode area. Humidified gaseous CO_2 is provided to the MEA, creating a three-phase-interface between the catalyst and the membrane. Careful control of the relative humidity of gaseous CO_2 is vital when operating MEA-based CO_2 electrolyzers. Inadequate CO_2 humidity may cause membrane dehydration problems and reduce durability, while excessively high humidity levels may promote HER, resulting in poor product selectivity. The elimination of the catholyte layer in the MEA-based CO_2 electrolysis system helps to prevent electrolyte flooding in the cathodic GDL. However, liquid products may accumulate in the GDL, clogging the pores and obstructing mass transport. Consequently, numerous studies have focused on optimizing the MEA-based gaseous CO_2 electrolysis system and developing specialized electrodes.[3]

In general, the use of three different types of electrochemical cells is determined by the specific application requirements. H-type cells are commonly utilized in laboratory-based investigations to assess the efficacy of new catalysts under relatively low current densities. In contrast, flow cells and MEAs incorporating GDLs are designed to facilitate the scaling up of CO_2 electrolysis processes, enabling electrosynthesis to be performed at an industrial scale. However, numerous challenges such as the formation of carbonate salts, water flooding, anode/membrane deterioration, low CO_2 conversion efficiency, and ion crossover still need to be addressed before CO_2 electrolysis can be commercialized using flow cells or MEAs, as summarized in Figure 2.3.
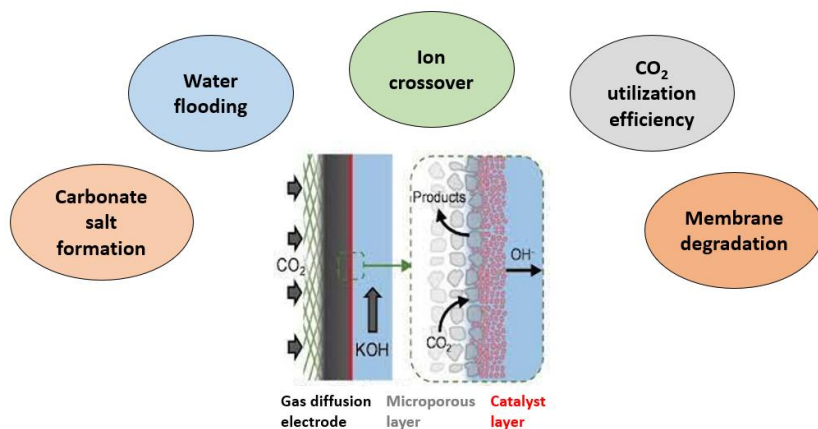
Figure 2.3 Schematic illustration of possible problems in gas diffusion layer (GDL) based electrochemical cells, namely flow cells and MEAs, in the course of CO_2 electrolysis. Reproduced from Ref.[3,21]

2.2 Strategies for enhancing CO_2 electrolysis

Numerous efforts have been devoted to developing strategies to enable highly efficient and selective production of specific products in CO_2 electrolysis. In addition to engineering electrochemical cell setups, these strategies mainly comprise the structural design of catalyst materials and the modification of local reaction environments, which are introduced in this subsection.

2.2.1 Rational design of catalyst materials

Various catalyst design strategies, such as reducing the size to the nanoscale, constructing a porous hierarchical structure, exposing specific facets, quantum confinement, doping, alloying, and defect engineering have been developed to manipulate the adsorption of reaction intermediates.[3,4,9,22–31] All of these strategies modify the electronic and geometric properties of the catalyst, which play a vital role in CO$_2$RR.

Figure 2.4 depicts the catalyst design strategies for CO$_2$RR. In general, the electronic structure of a catalyst surface significantly influences the overpotential and selectivity of the CO$_2$RR by directly modifying the binding energies of reaction intermediates. The geometric structure is usually associated with the catalytic site density and arrangement, which can impact the product selectivity and current density. However, it should be noted that these structural properties are often inherently interconnected. For instance, nano-porous materials frequently contain numerous grain boundary defects that possess unique electronic and geometric properties. Doping or alloying one metal surface with a second metal inevitably alters both the electronic and local geometric properties. In addition, quantum confinement is another example of how nanoscale geometry can fundamentally alter the electronic properties by restricting the spatial extent of the electronic wavefuntion.
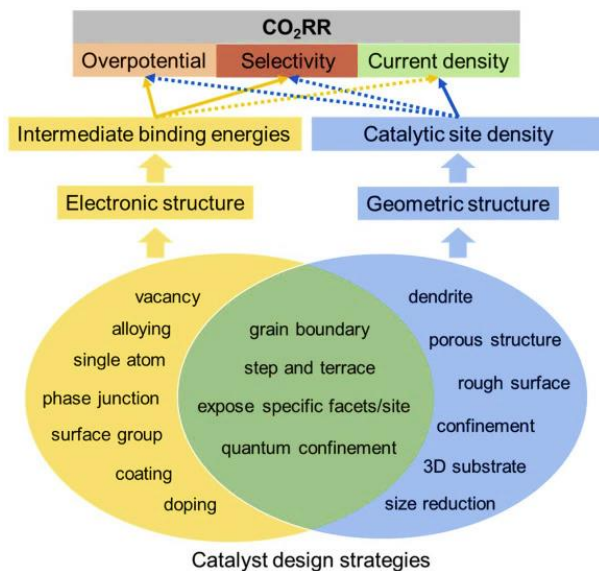
Figure 2.4 Illustration of catalyst structural design strategies for the CO₂RR. Copyright 2020, Elsevier.[22]

2.2.2 Modulating local reaction environment

In addition to the structure of the catalyst itself, the local reaction environment around the catalyst has a significant impact on the performance of CO_2 electrolysis. The term "local reaction environment" refers to various physicochemical effects that affect interfacial CO_2RR near the catalytic site. The first group of effects includes those that modify the intrinsic catalytic activity by altering the potential energy landscape (Figure 2.5a). These effects can be further classified into those that indirectly influence the reaction by changing the binding thermodynamics of the catalyst (electronic modification, EM) and those that affect the reactivity of the active center through spectator ligands or the interface with the electrode surface (EM-spec and EM-supp, respectively). For heterogenized molecular catalysts, the anchoring group can also influence the reactivity (EM-anch).
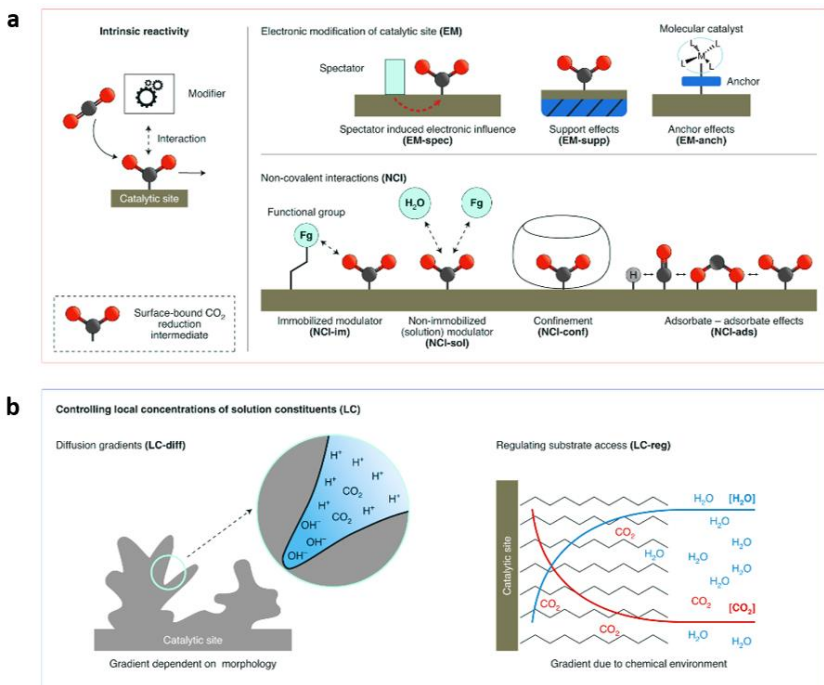
Figure 2.5 Classification of the local chemical environment effects in CO_2RR. (**a**) Infuencing factors that affect the intrinsic activity of catalysts through either an elelctronic modification of catalystic site or via non-covalent interactions with modulators or reacrion intermediates. (**b**) Effects that control the local contentration of solution constituents include the build-up of diffusion gradients to the surface due to morphological effects and gradients formed due to the changes of chemical environment on the surface. Copyright 2020, Springer Nature.[32]

The second group of effects, demonstrated in Figure 2.5a, includes those that directly influence the intrinsic catalytic activity through non-covalent stabilizing or destabilizing interactions, termed as non-covalent interactions (NCI), with substrate/product/intermediates. Such strategies make use of various modifiers, including immobilized ligands, non-immobilized modulators, solvent-adsorbate effects, confinement effects, and adsorbate-adsorbate interactions (NCI-immobilized modulator, NCI-solution modulator, NCI-confinement, and NCI-adsorbate effects, respectively). These effects modulate the immediate chemical

environment of the reaction, and depending on the initial intrinsic material-adsorbate energy, they can enhance or decrease the reaction rate.

The distinction between these two groups of effects is crucial as they have different capacities to modulate catalysis. Universal changes in the energetics of the catalyst and the binding energy of all intermediates occur due to electronic modifications (EM). Conversely, molecular effects (i.e., NCI) are more nuanced, as the stabilizing and destabilizing interactions vary for each intermediate.

The third group of effects involves the impact of the local concentration (LC) of solution constituents such as CO_2, H^+/OH^-, CO_3^{2-}, HCO_3^-, H_2CO_3, counterions, and water, which affect CO_2RR and HER (Figure 2.5b). LC can be influenced by diffusion gradients that arise due to surface-mediated reactions (LC-diff) or concentration gradients that form as a result of differences in the local chemical environment (LC-reg). The consumption of protons in CO_2RR and HER increases alkalinity in the vicinity of the electrode, reducing the concentration of hydronium (H_3O^+) as a competent proton donor and thus affecting the CO_2 equilibrium. The impact of this effect is greater for morphologies that reduce fast diffusion towards the catalytic site. LC-reg, on the other hand, directly impacts the concentration profiles of solution constituents at equilibrium without the reaction occurring by introducing factors such as hydrophobicity that influence the hydrogen-bonding network of H_2O and solubility of CO_2.

More importantly, in continuous CO_2 electrolysis both the evolution of catalyst structures and local reaction environment are dynamic and are highly correlated with each other, which accounts for the dynamic evolution of CO_2RR performance. In most cases, a constant degradation of catalytic reactivity is monitored over time. However, the underlying effects of the catalyst structural evolution and the change of local environment remain to be investigated with the help of various in situ characterization techniques, as discussed throughout this thesis.

2.3 Cu-based catalysts for CO_2 electrolysis

Electrochemical reduction of CO_2 has been a topic of study since the 1950s. In 1985, Yoshio Hori and colleagues were the first to quantify both gaseous and liquid products in CO_2 electrolysis in order to account for 100% of the Faradaic efficiency (FE, Figure 2.6).[33,34] FE is a measure of the effectiveness of an electrochemical process in converting reactants into a desired product. It is defined as the ratio of the amount of electrons needed for the desired product generated by an electrochemical reaction to the total amount of electrons consumed in the reaction, taking into account any side reactions or losses. A FE of 100% means that all of the participating electrical charge was converted to the desired product, with no side reactions or losses.
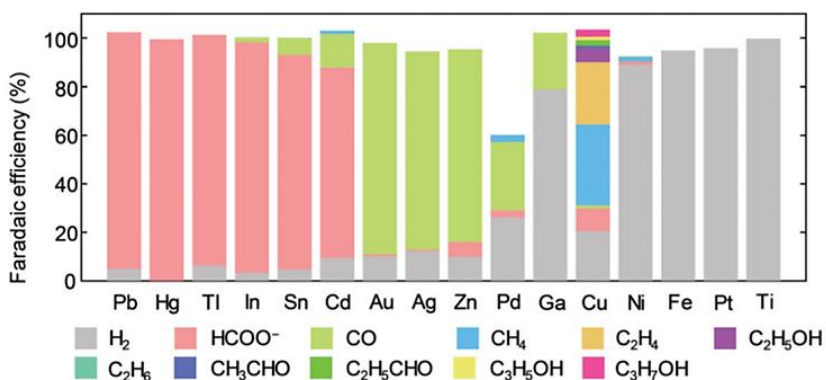
Figure 2.6 Product distribution of CO_2 electrolysis at a constant current density of 5 mA cm^{-2} (based on geometric area) on various polycrystalline metal electrodes. Copyright 2008, Springer.[34]

In that work, Hori and co-workers performed constant-current electrolysis of CO_2-saturated 0.5 M $KHCO_3$ at 5 mA cm^{-2} for up to an hour on various polycrystalline metal electrodes. Subsequent studies using similar methods led to the classification of metal electrodes into four groups based on their selectivity towards different CO_2 reduction products: (1) Pb, Hg, Tl, In, Sn, Cd, and Bi produce primarily formate ($HCOO^-$); (2) Au, Ag, Zn, Pd, and Ga produce mainly carbon monoxide

(CO); (3) Ni, Fe, Pt, and Ti reduce a very small fraction of CO_2 and instead almost exclusively favor HER; and (4) Cu produces hydrocarbons, aldehydes, and alcohols. Remarkably, Cu was found to uniquely produce complex multicarbon products with relatively high Faradaic efficiency. As such, CO_2 reduction research has largely focused on Cu-based materials, which remain the most active for multicarbon products to this day, as described below.

2.3.1 Importance of Cu-based catalysts

Following studies have revealed that more than 16 different chemical products can be detected in Cu-assisted CO_2 electrolysis under different potentials (Table 2.1 and Figure 2.7).[4,10]

These products include single carbon (C_1) products such as carbon monoxide (CO), methane (CH_4), formate/formic acid ($HCOO^-$/$HCOOH$), and methanol (CH_3OH), as well as multicarbon (C_{2+}) products such as ethylene (C_2H_4), ethanol (C_2H_5OH), acetate/acetic acid (CH_3COO^-/CH_3COOH), ethane (C_2H_6), n-propanol (PrOH), acetone, acetaldehyde, ethylene glycol, propionaldehyde, etc.

Such a complex product distribution originates from the varied binding energies of key CO_2RR and HER intermediates, including *H, *OCHO (bound to the surface through O), *COOH (bound to the surface through C), and *CO, which results in complicated reaction pathways in Cu-catalyzed CO_2 electrolysis. These intermediates are of great importance as they are related in the initial activation of CO_2 molecules at the beginning of CO_2RR, as indicated in the following reactions:

$$* + CO_2 + H^+ + e^- \rightarrow * COOH \qquad 2.12$$

$$* + CO_2 + H^+ + e^- \rightarrow * OCHO \qquad 2.13$$

$$* + CO_2 + e^- \rightarrow * CO_2^- \qquad 2.14$$

$$* + H^+ + 2e^- \rightarrow * H^- \qquad 2.15$$

In these equations, the symbol " * " is used to represent active sites on catalyst surfaces. The reactions described in Equations 2.12 and 2.13 are known as concerted proton-electron transfer (CPET) reactions. CPET reactions are important for reducing reaction barriers because they allow for the transfer of both a proton and an electron in a single step, which can decrease the overall energetic barrier for the reaction. By transferring both the proton and electron together, the reaction avoids intermediate steps that would require higher energy input. This makes CPET an efficient mechanism for many chemical reactions, particularly those involving redox processes.
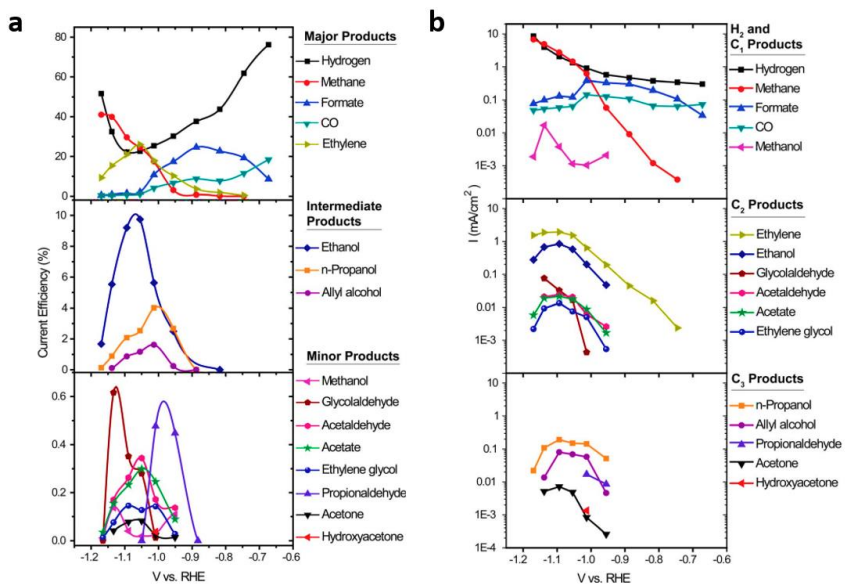
Figure 2.7 (**a**) Current efficiency for each product as a function of potential is shown for major, intermediate range, and minor products. The current efficiency was calculated by determining the number of Coulombs needed to produce the measured amount of each product and dividing by the total charge passed during the reaction time. (**b**) Partial current density as a function of potential for products containing different numbers of carbon atoms, namely C_1, C_2, and C_3 products. Adapted from Ref.[10]

Generally, these reactions have been computationally studied to determine trends in selectivity among post-transition metal surfaces. Previous findings suggest that the intermediate *COOH is more likely to produce CO, while *OCHO is more likely to form formic acid.[35,36] This assertion is widely accepted in the literature. Through calculated binding energies, it has been found that such proposed mechanisms generally agree with experimental results.

Specifically, post-transition metals such as Pb and Sn tend to bind CO_2 via oxygen and are selective towards formic acid, whereas transition-metal electrodes tend to bind via carbon. By only considering the hydrogen binding energy of the metal as the key descriptor, it is possible to classify metals into three groups. The first group includes metals that form primarily H_2 with under potential-deposited hydrogen (H_{upd}), the second group includes metals with H* at the CO_2 reduction potential that form mostly CO, and the third group includes metals with little or no H* at the CO_2 reduction potentials that produce formic acid (Figure 2.8).

The binding energy refers to the energy required to adsorb an atom or molecule onto a catalyst surface and is frequently used as a descriptor to understand catalytic activity and selectivity. It is typically measured in electron volts (eV) and represents the strength of the interaction between the catalyst surface and the adsorbate. For the production of multicarbon products from further reduction of CO on Cu, the ΔE_{CO^*} and ΔE_{H^*} binding energies are considered. This distinguishes Cu from all other metals examined here since Cu does not enable H_{upd} while it also binds CO* (Figure 2.8b). As such, Cu catalysts can further reduce CO to hydrocarbon products or partially reduce it to alcohol products.

Metals that exhibit excessive binding strength with CO can be deactivated due to poisoning by this intermediate. Conversely, metals that have weak CO binding ability will release it from the surface before it has a chance to undergo further reactions. Hence, in agreement with the Sabatier principle, the intermediate CO binding energy on Cu plays a critical role in its ability to act as a catalyst for CO_2 reduction to products that have a greater reduction potential than CO.[37]
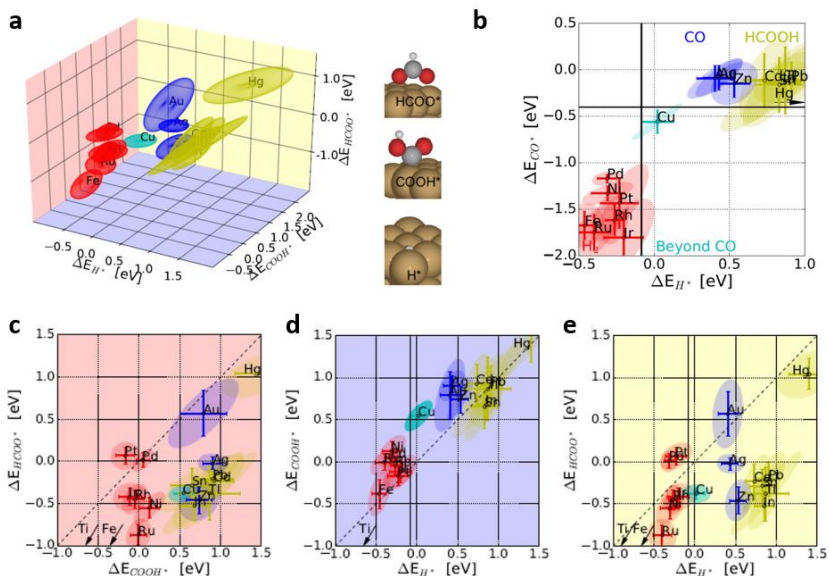
Figure 2.8 Combined plot of the four proposed descriptors in CO_2 electroreduction towards H_2, CO, and HCOOH. (**a**) The three-dimensional space of descriptors is plotted with the coupled binding-energies (ΔE_{H^*}, ΔE_{COOH^*}, *and* ΔE_{HCOO^*}) with respect to Au. (**b**) The plot of binding energies of the intermediates ΔE_{CO^*} versus ΔE_{H^*}. Data points for metals are color-coded on the basis of their classification group and each background plane is colored to match the 2D projections of energies and ellipses in (**c**), (**d**), and (**e**) for the ΔE_{HCOO^*} vs. ΔE_{COOH^*}, ΔE_{COOH^*} vs. ΔE_{H^*}, and ΔE_{HCOO^*} vs. ΔE_{H^*} planes, respectively. Four groups of metals are identified based on types of products: H_2 (red), formic acid (yellow), CO (blue) and beyond CO* (cyan). Reproduced from Ref.[38]

Additionally, various investigations have demonstrated that CO adsorption on Cu inhibits the competing HER by either blocking active sites or altering the binding energy of H* (Figure 2.9). The extent of CO coverage on Cu is usually very high, at least until transport limitations arise. Therefore, CO-induced poisoning of HER is an important mechanism by which Cu sustains a high Faradaic efficiency for CO_2 reduction in aqueous electrolytes.[39,40]
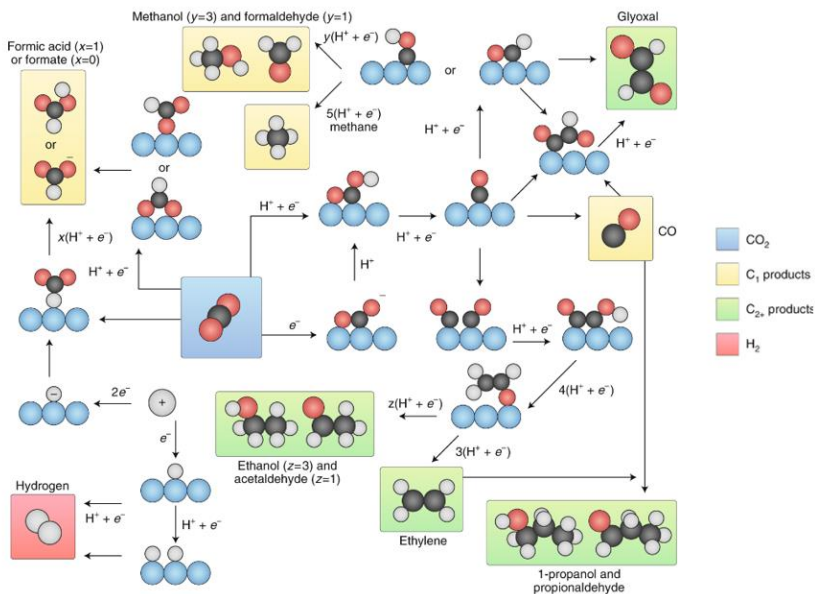
Figure 2.9 Overview of CO_2 reduction reaction pathways on Cu towards different products. Copyright 2018, Elsevier.[41]

Since Hori's discovery in 1985 of the ability of Cu electrodes to reduce CO_2 to hydrocarbons with high FE, a significant amount of research has been dedicated to uncovering the underlying reaction mechanisms. Nevertheless, despite over three decades of investigation, there is still a lack of agreement among researchers regarding the reaction pathways for CO_2 reduction, particularly for the pathways towards multicarbon products. The reduction of CO_2 to multicarbon products on Cu involves the formation of different surface intermediates, including *CH_x ($x = 1 - 3$) and *COH. These surface intermediates are subsequently reduced to form different hydrocarbons such as methane, ethylene, and ethane, among others, as depicted in the reaction network scheme in Figure 2.9.

Overall, the electrochemical CO_2RR on Cu is a complex process that involves multiple intermediate steps, and the formation of different products depends on the applied potential and reaction conditions. Accurate comprehension of the product

formation mechanisms during CO_2 reduction is imperative for the advancement of more effective catalysts that can better satisfy industrialization requirements.

2.3.2 Performance of Cu-based catalysts in literature

The selective production of multicarbon products through deep reduction of CO_2 is highly important due to the superior energy density and broader applications of these products.[7,8,42,43] One example is ethylene, which serves as a precursor to various chemicals, including polyethylene, and can also be used directly as fuel for welding or as a component of natural gases. Traditionally, ethylene is produced through CO or CO_2 hydrogenation, which requires significant energy consumption and has unavoidable environmental impacts. Conversely, utilizing renewable electricity for the selective reduction of CO_2 to ethylene represents a sustainable and environmentally friendly pathway.[28]

Another significant C_{2+} product is ethanol, which finds widespread use in fields such as medicine, industrial chemical synthesis, food production, and as a fuel for vehicles. Currently, the production of ethanol relies on either ethylene or agricultural feedstocks, which both demand substantial energy inputs.[44] Selective CO_2 reduction to produce ethanol not only reduces CO_2 emissions but also generates economic benefits, making it a promising and sustainable alternative approach.

Table 2.2 summarizes the performance of various Cu-based catalysts for electrosynthesis of ethylene and ethanol from CO_2 based on recent publications. Remarkably, a record-high FE of ~87% for ethylene was achieved on polyamine-incorporated Cu electrodes in an extremely alkaline electrolyte of 10 M KOH.[45] As for the selective production of ethanol, a maximum FE of ~91% was realized on Cu clusters.[46] Despite of high selectivity for production of ethylene and ethanol, the production yield and durability of catalysts are currently still rather low. In most cases, the measured current densities are less than 50 mA cm^{-2}, and the durability of catalysts is usually estimated within 24 h of operation.

Table 2.2 Overview of various Cu-based catalysts for electrochemical CO_2 reduction to multicarbon products, particularly ethylene and ethanol, based on recent publications.

Electrocatalyst	Product	FE	Current density	Condition	Ref
Au@Cu	C_2H_4	44.9%	~ 32.1 mA cm^{-2} @−1.11 V vs. RHE	H cell; 0.1 M KHCO$_3$	[47]
Cu clusters	C_2H_4	45%	262 mA cm^{-2} @−1.07 V vs. RHE	Flow cell; 1 M KOH	[48]
Reconstructed Cu	C_2H_4	56%	17 mA cm^{-2} @−2.0 V vs. Ag/AgCl	H cell; 0.05 M KHCO$_3$	[49]
Hydrophobic Cu dendrites	C_2H_4	56%	30 mA cm^{-2} @−1.1-1.5 V vs. RHE	H cell; 0.1 M CsHCO$_3$	[50]
Abrupt Cu	C_2H_4	70%	75-100 mA cm^{-2} @ −0.55 V vs. RHE	Flow cell; 7 M KOH	[51]
Surface modified Cu	C_2H_4	72%	~ 319 mA cm^{-2} @−0.83 V vs. RHE	Flow cell; 1 M KHCO$_3$	[52]
Activated Cu nanowires	C_2H_4	77.4%	~ 22.4 mA cm^{-2} @−1.01 V vs. RHE	H cell; 0.1 M KHCO$_3$	[53]
Cu-Al	C_2H_4	80%	400 mA cm^{-2} @−1.5 V vs. RHE	Flow cell; 1 M KOH	[54]
Defective Cu nanosheets	C_2H_4	83.2%	60 mA cm^{-2} @−1.18 V vs. RHE	H cell; 0.1 M K$_2$SO$_4$	[55]
Polyamine-Cu	C_2H_4	87% ± 3%	~30 mA cm^{-2} @2.02 V	Full cell, 10 M KOH	[45]
Ce(OH)$_x$ modified Cu	C_2H_5OH	43%	300 mA cm^{-2} @−0.7 V vs RHE	Flow cell; 1 M KOH	[56]
Cu$_5$Zn$_8$	C_2H_5OH	46.6%	~ 4.9 mA c.m^{-2} @−0.8 V vs. RHE	H cell; 0.1 M KHCO$_3$	[57]
Cu$_n$ clusters	C_2H_5OH	91%	1.2 mA cm^{-2} @−0.7 V vs. RHE	Single cell; 0.1 M KHCO$_3$	[46]

Overall, copper-based catalysts have attracted increasing attention in the study of CO_2RR due to their unique ability to produce various multicarbon (C_{2+}) products, such as ethylene, ethanol, and n-propanol, which can be readily upgraded into commercial products through established industrial catalytic processes.[1,4] While several CO_2RR catalysts can generate single-carbon (C_1) products (e.g., carbon

monoxide and formate) with nearly 100% selectivity,[58–62] selective conversion of CO_2 to multicarbon products on Cu-based catalysts remains challenging.[63] As summarized in Table 2.2, numerous strategies have been reported to enhance the formation of C_{2+} products, while also suppressing the production of both C_1 products and the competing HER. These approaches mainly include structure and morphology engineering of Cu-based materials by surface modification,[31,45,64,65] shape/size control,[66,67] and alloying[68,69], as well as the regulation of reaction environments by adapting the electrolyte composition,[26,70,71] means of gas transport,[71,72] and types of ionomer films.[12,73,74] However, determining genuine limits to catalytic performance remains challenging since several factors beyond the nature of the catalyst itself can impact reaction outcomes. This is especially true for the case of catalytic nanomaterials, where different deposition methods, substrates, and ink formulations can influence key catalytic performance metrics, such as activity, stability, and selectivity. Understanding how these factors affect the electrochemical CO_2RR and leveraging these dependencies to engineer optimized systems is essential for further improving the performance of state-of-art catalyst materials.

In the typical approach to preparing cathodes for electrochemical CO_2 reduction, inks are first created by dispersing catalyst powders into water/alcohol solvent mixtures, after which they are deposited onto conductive substrates such as carbon paper. Ionomers are often added to these ink formulations to prevent agglomeration of nanoparticles, as well as to improve their adhesion to substrates. Nafion (perfluorosulfonic acid) is the most widely used ionomer for electrode preparation in various electrochemical applications, including water splitting, oxygen reduction, and nitrogen reduction, as well as for carbon dioxide reduction.[11] The work presented in this thesis systematically investigates how the tuning of synthesis parameters can be used to improve both the activity and stability of Cu-based catalysts modified by Nafion films for production of multicarbon products while maintaining or even improving their high selectivities. As a basis for understanding these effects, a detailed description of Nafion is introduced in the next chapter.

Chapter 3. Fundamentals of Nafion

In this chapter, a comprehensive introduction to Nafion is given, including the origin of Nafion, its structure, morphology, and properties, and its application in CO_2 electrolysis.

3.1   Origin of Nafion

Nafion is the registered trademark of the first commercial perfluorinated sulfonic-acid (PFSA) ionomer that was developed in the 1970s by the company DuPont. PFSA belongs to a class of synthetic polymers with ionic properties that are called ionomers, and is known for its remarkable ionic conductivity and chemical-mechanical stability. Nafion and its derivatives were first synthesized by the copolymerization of tetrafluoroethylene (TFE) (the monomer in Teflon) and a derivative of a perfluoro molecule (alkyl vinyl ether) with sulfonyl acid fluoride (Figure 3.1). The resulting product is a $-SO_2F$ containing thermoplastic that is extruded into films. Hot aqueous NaOH is then used to convert sulfonyl fluoride ($-SO_2F$) groups into sulfonate groups ($-SO_3^-$ Na^+). Finally, this Nafion precursor is converted to Nafion through ion exchange in acidic solutions, resulting in its common form, which contains sulfonic acid ($-SO_3H$) groups.[75] Importantly, Nafion can be dispersed into solution by heating in aqueous alcohol at 250 °C in an autoclave. Such solutions are useful for subsequent casting into thin films, modification of electrodes, or as polymeric binders for preparing composite electrodes,[76] which is the focus of the present work.

In their bulk form, Nafion membranes are well known proton conductors that have been used extensively for proton exchange membrane (PEM) fuel cells due to the excellent chemical and mechanical stability of this material under harsh aqueous reaction conditions. In recent years, with the increasing interest in a variety of

electrochemical synthesis (electrosynthesis) processes, such as the production of hydrogen, oxygen, and ammonia, as well as the conversion of carbon dioxide or carbon monoxide to higher order chemicals, Nafion ionomer solutions have been widely used as binders in the preparation of electrodes, especially for electrodes based on nanomaterials.
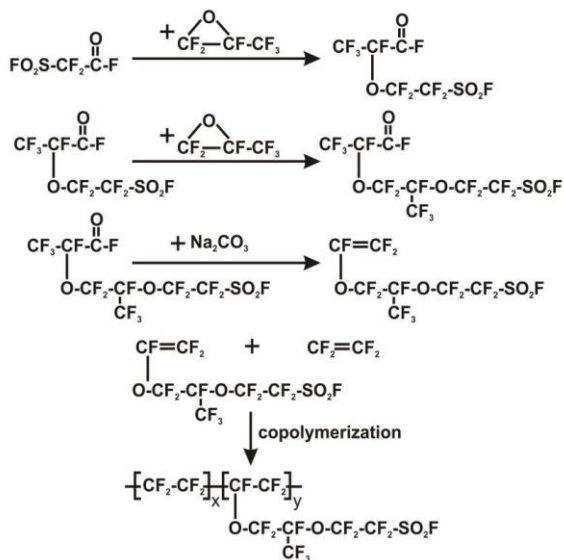

Figure 3.1 Synthesis scheme for production of Nafion according to the DuPont process. Copyright 2006, Elsevier.[75]

3.2   Structure and morphology

The general chemical structure of Nafion is that of a random copolymer composed of an electrically neutral semi-crystalline polymer backbone (polytetrafluoroethylene (PTFE)) and a randomly tethered side-chain with a pendant ionic group, SO_3^- (polysulfonyl fluoride vinyl ether), as shown in Figure 3.2. Such functional groups are related to a specific counterion, namely $SO_3^- + H^+ \rightarrow SO_3H$. The highly dissimilar nature of the hydrophobic PTFE backbones and hydrophilic terminal groups leads to natural phase separation, which is particularly

enhanced via the solvation effect upon interaction with solvents (e.g., water). Therefore, it is the intrinsic phase difference within the structure of Nafion that gives it unique ion- and solvent-mediating properties.
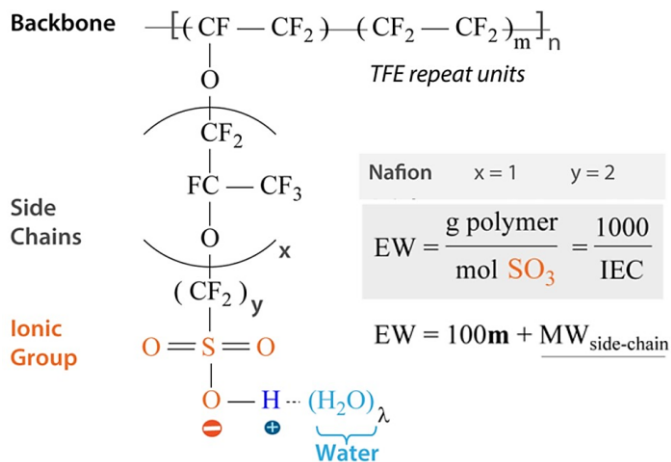

Figure 3.2 The molecular structure of Nafion. The equivalent weight (EW) of Nafion can be either defined as the grams of dry ionomer per ionic group, which is inversely proportional to the ion-exchange capacity (IEC), or characterized in terms of side chain properties via the equation EW = 100m + MW$_{side-chain}$, where m is the number of TFE units and MW$_{side-chain}$ is the molecular weight of side-chain. Adapted from Ref.[11]

Due to variability in the repeating sequence of the Teflon backbone and lengths of its side chains, Nafion can be produced in various chemical configurations, which necessarily means the molecular weight (MW) is variable. Though the MW has been estimated to be around 10^5-10^6 Dalton (note: one Dalton corresponds to one-twelfth of the mass of an unbound neutral atom of carbon-12 in its nuclear and electronic ground state and at rest), Nafion is more frequently described by the equivalent weight, EW, defined as the grams of dry polymer per ionic group (i.e., g polymer / mol SO$_3$). The EW is directly related to the number of TFE units in the backbone, m, via the relation EW = 100m + MW$_{side-chain}$, where the final term is the side-chain molecular weight. For a given EW, the shorter the side-chain (or the

lower its MW) of the Nafion, the higher its backbone fraction. Thus, both side-chain length (size) and backbone length (m) control the EW and chemical structure of the Nafion ionomer, as well as its phase separation behavior. From the typical bond lengths, the extended side chain length can be estimated to be on the order of 0.8 nm and the extended backbone spacing between two side chains, uniformly distributed along the backbone, can be estimated to be on the order of 0.6-1.2 nm for Nafion possessing an EW of 1100 g/mol.[11]

Despite the clear molecular-level understanding of the chemical composition of Nafion, the structure and morphology of Nafion in its two general forms, including in ionomer dispersions and in casted thin films, are not yet fully understood. The reason for this is the complex structure and morphology over different length scales and their strong dependencies on preparation routes, as well as their interactions at interfaces and under operational conditions. As a consequence, numerous studies have focused on this research topic in the past decades, and some important findings of particular relevance to this thesis are introduced below.

3.2.1   Nafion ionomer dispersions

Owing to the considerable chemical and physical dissimilarity of its backbone and side groups, Nafion cannot be completely dissolved in any solvent. However, it can be dispersed well in the form of colloidal ionomer particle suspensions in a wide range of liquids, such as water or organic solvents. The structure of Nafion ionomer in dispersions has been shown to be governed by both the polarity of the solvent and the solubility of the polymer backbone. The structural analysis of Nafion dispersions by small-angle X-ray scattering (SAXS) techniques began in the mid-1980s, soon after the basic procedures for creating dispersions of Nafion in liquid media had been established. Welch et al. utilized small angle neutron scattering (SANS) and fluorine (^{19}F) nuclear magnetic resonance (^{19}FNMR) to examine the morphology of Nafion ionomer (EW = 1000 g/mol, Na$^+$ form, 2.5 wt.%) aggregates in different solvents.[77] As shown in Figure 3.3, three alternative forms of solvated Nafion ionomer aggregates are revealed by SANS modeling, including a well-defined cylindrical form in glycerol and ethylene glycol with varying solvent

penetration, a less-defined but highly solvated large particle form (>200 nm) in water/n-propanol mixtures, and a random-coil conformation (real solution behavior) in N-Methyl-2-pyrrolidone (NMP).[78] Generally, for the case of dilute dispersions, Nafion ionomers form aggregates at the nanoscale and their size and shape depend on the type of solvents. In contrast, concentrated Nafion ionomer dispersions are characterized by the bundling of ionomer aggregates to produce larger secondary aggregates.
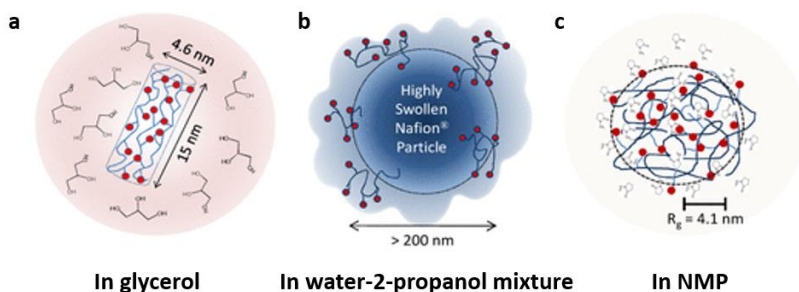

Figure 3.3 Illustrations of the morphologies of Nafion ionomer aggregates in different solvents, including glycerol (**a**), a mixture of water and 2-propanol (**b**), and N-Methyl-2-pyrrolidone (NMP, **c**). Reproduced from Ref. [78]

For electrochemical applications, the Nafion ionomer dispersions are typically manufactured using mixtures of water and alcohol as the solvent. Therefore, detailed understanding regarding the dispersion behavior of Nafion ionomer in water/alcohol mixtures is of great importance as it is critical to the properties of subsequently prepared Nafion thin films and films in solid form. Thus, the structural characterization of Nafion ionomer aggregates in water/alcohol mixtures has been extensively explored using various techniques such as SAXS, SANS, wide-angle neutron scattering, dynamic light scattering (DLS), and nuclear magnetic resonance (NMR) spectroscopy.[79–83]

Berlinger et al. corelated the structure of Nafion ionomer aggregates in water/alcohol mixtures with its inherent acidity (Figure 3.4).[81] In particular, it is known that PFSA is a superacid in solid form, with the side chain pK_a (pK_a = -

$\log_{10}K_a$ where K_a is the acid dissociation constant of the solution) reported to be approximately −6.[84] It is thus predicted that PFSA will exhibit some acidity as well in dispersions. This inherent acidity is crucial to comprehending the electrostatic interactions in ink systems, as the level of electrostatic repulsion is dependent on the surface charge, or Zeta potential. It is well established that the Zeta potential is heavily impacted by pH (for systems where protons are the determining ions, which applies to the majority of systems). Thus, pH is a key factor in determining particle aggregation. By adjusting the composition of water/alcohol solvents, the numbers of accessible protons of Nafion ionomer can be varied. The acidity of dispersions in water-rich solvents is found to be higher compared to those in solvents with a higher proportion of n-propanol. For example, the proton dissociation in a dispersion containing 90% water can be as much as 55% higher than a dispersion containing 30% water. The differences in acidity result in variations in electrostatic interactions and subsequently affect particle aggregation in dispersions (Figure 3.4). In particular, by combining cryo-TEM imaging with such pH-dependent data, Berlinger and co-workers elucidated the ionomer aggregate conformation in dispersion, particularly with respect to the orientation of the side chains versus the backbone. Figure 3.4a schematically depicts this: at low Nafion and high water concentrations, the backbones cluster together and then extend outward, allowing nearly all the side chains to be solvated. In solvents that are rich in n-propanol, there is a reduced driving force for the backbones to aggregate or for the side chains to extend into solution, leading to the formation of rod-like aggregates with a more basic pH. Additionally, as the ionomer concentration increases and secondary aggregates form, there are fewer accessible protons, explaining why higher weight percent dispersions exhibit lower pH values for all water contents.

In summary, the solvent used to disperse Nafion ionomer can have a significant impact on the structures and properties of the resulting Nafion dispersion. Selecting a solvent that is compatible with Nafion ionomer and results in the desired properties is crucial for achieving optimal performance in applications.
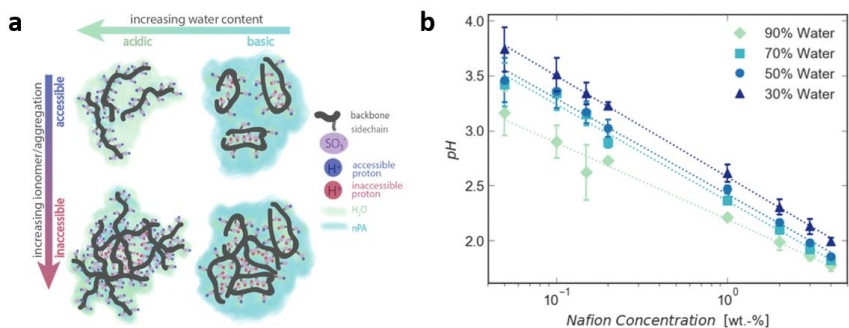
Figure 3.4 (**a**) Schematic of two-dimensional slice of possible structures representing individual chains and aggregates of Nafion ionomers, showing the side-chain orientation differences (pH differences) as a function of aggregation and solvent content. (**b**) Measured pH of Nafion dispersions as a function of Nafion and water concentrations. Reproduced from Ref.[81]

3.2.2   Casted Nafion thin films

3.2.2.1 Effect of dispersion solvent type

Nafion films are typically prepared by casting Nafion dispersions onto a substrate by means of spin-, dip-, or spray-coating, followed by drying and post-treatments. The preparation methods and conditions, including the drying temperature, significantly impact the characteristics of the resulting Nafion film. More importantly, the influence of the solvent compositions on Nafion dispersions can persist even after the dispersions are dried. Thus, the physical properties of a solvent, including dielectric constant, solubility parameter, viscosity, surface tension, boiling point and vapor pressure, will not only alter the structures of Nafion ionomer aggregates in dispersion but also have a great impact on the formation of Nafion films by influencing the interactions between Nafion ionomers themselves and with substrates during the drying process (Figure 3.5).
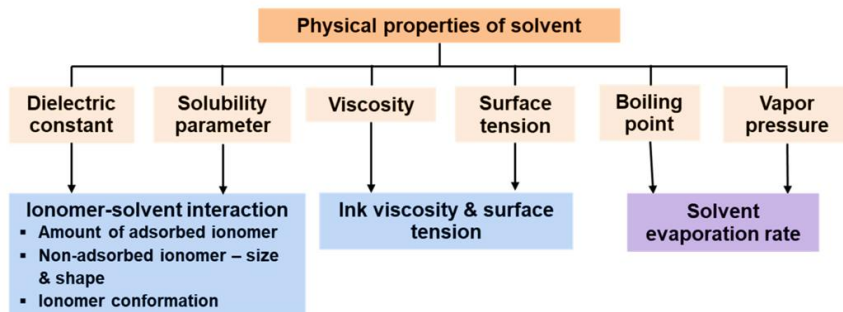
Figure 3.5 The physical properties of solvent and their effects on the microstructure and macroscopic properties of Nafion dispersions, as well as evaporation rate. Copyright 2023, MDPI.[85]

Controlling the physical properties of the solvent is a straightforward pathway to tailor the microstructure and macroscopic properties of casted Nafion films. Indeed, the physical properties of the dispersion medium can be finely altered by varying the type of solvent or by using mixed solvents and varying their ratios. As described above, water/alcohol mixtures are commonly used as solvents for various commercial Nafion ionomer dispersions. However, the ratio of water and alcohol is not necessarily optimal considering the varied requirements for Nafion films in different applications. Therefore, the effect of the water/alcohol ratio on Nafion thin films produced from dispersion must be carefully considered.

Berlinger and coworkers conducted a systematic examination of the effect of dispersion solvent, which was varied by adjusting the water to alcohol ratios, on the transformation of film morphology from dispersions to thin films, observed in real-time using GISAXS. The aggregation behavior of Nafion ionomer in dispersion is found to vary with water concentration, which influences the coalescence of the films and the resulting nanoscale structure. As the water concentration in the dispersion increases, the interactions between Nafion aggregates and their ordering become more regular. The findings indicate that the films produced from high water content dispersions have better inner network connectivity within a more organized structure upon drying, leading to larger network domains compared to

those made from low water content dispersions (Figure 3.6). This stronger interaction is reflected in improved conductivity and reduced swelling (water absorption) in subsequently hydrated films. Importantly, these differences caused by the solvent remain unchanged even after thermal treatment, indicating that annealing locks-in the differences in film formation caused by the varying solvent compositions in the dispersion. In contrast, for unannealed films, the solvent history can be at least partially eliminated upon exposure to pure solvents via reconstruction.[86]
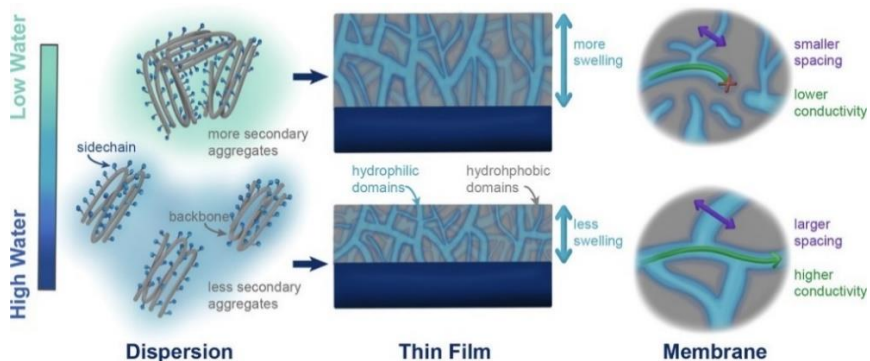

Figure 3.6 Proposed schematic depicting conclusions of structural measurements of dispersion aggregation, thin films, and membranes for Nafion derived from high- and low water/alcohol ratio solvents. Features are not drawn to scale. The thin film diagram zooms into possible nanoscale/mesoscale structure (not meant to depict the entire film), and depict the important role of increased inner network connectivity from high water/alcohol solvents for improving ionic transport and reducing water uptake and swelling. Copyright 2020, American Chemical Society.[86]

Gao et al. also studied the water/alcohol ratio effect in Nafion thin films with thicknesses of 50 to 110 nm in terms of the morphology and proton transport properties using GISAXS and GIWAXS.[87] The decrease in isopropanol (IPA) fraction from 54% to 2% by weight was found to promote formation of hydrophilic domains in tightly packed Nafion thin films, accompanied by the formation of a crystalline-rich phase in the hydrophobic domain, indicating strong hydrophilic/hydrophobic domain separation (Figure 3.7). On the other hand, Nafion

thin films casted with a 54 wt.% IPA solvent presented loosely packed structures, the lowest degree of phase separation, and the smallest proton conductivity value. The close arrangement of sulfonic groups on the exterior of Nafion molecules was found to promote hydrophilic/hydrophobic phase separation in tightly packed Nafion thin films. This was found to arise from specific adsorption of Nafion molecules due to the interaction between the sulfonic groups and the surface of the Pt substrate used in that work. Indeed, previous studies have shown that the interaction between sulfonic groups and substrates affects the morphology of Nafion thin films on these substrates, which will be further introduced in the next subsection.
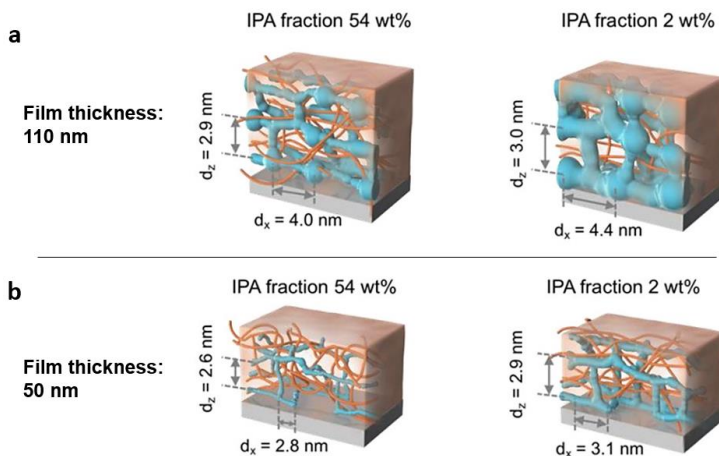

Figure 3.7 Schematic models of 110 nm (**a**) and 50 nm (**b**) thick Nafion thin films on Pt substrates casted from dispersion with different fractions of isopropanol (IPA) in the solvent comprising water-isopropanol mixtures. Reproduced from Ref.[87]

3.2.2.2 The impact of substrate

As suggested above, the substrate can greatly influence the morphology and performance of Nafion thin films. The interaction between Nafion molecules and the substrate surface is crucial, as it affects the specific adsorption of Nafion molecules, which can lead to the development of hydrophilic/hydrophobic phase

separation and shape the overall structure of the film. The properties of the substrate, such as its surface roughness, charge, and hydrophobicity, also play a role in determining the final outcome of the Nafion thin film. By understanding the interplay between Nafion and the substrate, researchers can gain insights into how to optimize the deposition of Nafion thin films for specific applications.

Based on current studies on PFSA thin films,[11,88–90] three thickness regimes can be identified, as given in Figure 3.8: (a) an ultrathin film regime (< 15 to 20 nm thick) with dispersion-like behavior, which is characterized by reduced phase separation between the hydrophilic and hydrophobic domains and decreased hydrophobic-domain elastic forces, (b) a thin-film regime in which confinement-induced changes are observed in the film's structure and transport properties, leading to reduced swelling, limited transport, and anisotropic nanostructure. The specific interactions between the ionomer moieties and substrate result in further changes in morphology, including local ordering of the domains at the substrate/film interface, and (c) a bulk-like regime ranging from micrometers to hundreds of nanometers, in which the ionomer film behaves like a bulk membrane and the substrate effect is suppressed.[91]

Between the ultra-thin (a) and thin film (b) regimes, there is a suggested critical thickness of 50 to 60 nm where confinement effects become more pronounced, but the transitions between regimes are not clearly defined. In particular, the impact of annealing and substrate interactions on this critical thickness and transitions should be noted. Properties such as diffusivity, permeability, and mechanical properties may also deviate as a result of larger-scale morphological reorganization. Likewise, the interaction between the substrate and the hydrophilic domains, as well as the hydrophobic-domain forces via the main-chain (controlled by EW and crystallinity), play a key role in defining the boundary between thin (Figure 3.8b) and thick (Figure 3.8c) film regimes for a given substrate. Reducing the EW could lead to better phase separation and domain orientation by enhancing favorable interactions between the ionic moieties and the substrate.[88]
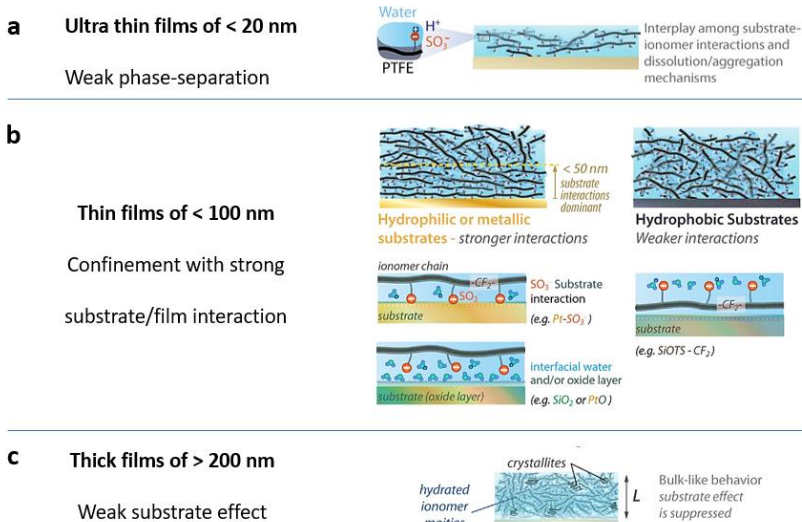
Figure 3.8 Illustration of the thickness-substrate interplay controlling the nanostructure of Nafion thin films. The dominate influcening effect in interaction between Nafion and substrate is (**a**) the weak phase-sparation for ultra thin Nafion films of < 20 nm, (**b**) the confinement with strong substrate/film interaction, and (**c**) the weak substrate effect for thick Nafion films of >200 nm, respectively. Reproduced from Ref.[11]

3.2.2.3 The effect of post-treatment

It has been well documented that the morphology and properties of PFSA films and membranes (whether extruded or cast) are strongly influenced by post-treatment process (e.g., thermal treatment and ion exchange). Such post-treatments have been shown to alter the water uptake, and transport coefficients (e.g., diffusivity), density, permeability, ionic conductivity, selectivity, mechanical properties, and thermal stability.[11]
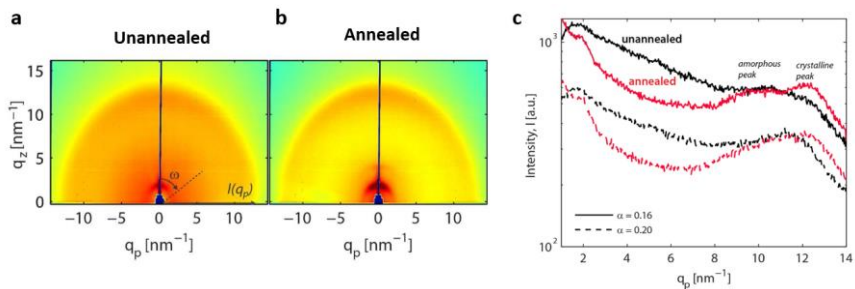
Figure 3.9 2D GIWAXS patterns of (**a**) unannealed and (**b**) annealed Nafion films spin-cast on carbon supports. (**c**) Intensity profiles from the line cuts on 2D patterns for these samples at angles of 0.160° and 0.200°. The nominal thicknesses of the sample is ~232 nm and the annealing procedure was performed at 146 °C for 60 min. Reproduced from Ref.[89]

To highlight the impact of thermal treatments on the structural properties of Nafion films, Figure 3.9 shows GIWAXS profiles for spin-cast films on carbon, both annealed and unannealed. The impact of the annealing process is evident from the change of the strong and anisotropic WAXS scattering ring, which suggests crystalline order (Figure 3.9a & b). Associated line profiles reveal that annealing results in the formation of a crystalline peak at $q = 12$ nm^{-1}, next to the amorphous peak at 10.5 nm^{-1}. This annealing-induced crystalline order with a spacing of 0.5 nm corresponds to the CF_2 chains of PTFE crystallites and has been widely observed in bulk Nafion membranes. The formation of such crystallites reduces water uptake by increasing the backbone physical crosslinking, as seen in Figure 3.9c by shifts in the ionomer peak around $q = 1.5$ nm^{-1}. As the films reach the size of the crystallites, the impact of annealing is expected to decrease because the chains become confined at these thicknesses.

In addition to thermal treatment, ion exchange processes also have a significant impact on the structures and properties of Nafion films. The majority of commercial Nafion ionomers are in the protonated form ($-SO_3^-$–H^+), which has the lowest permeability but highest sensitivity to temperature changes. Replacing the H^+ counterion in Nafion ionomer with larger cations reduces diffusivity due to changes in connectivity and domain size, while also increasesing solubility because of

stronger cation/sulfonate interactions that lower entropy.[92] Moreover, such ion exchange can improve the thermal stability of Nafion films. This is because the elastic moduli of cation exchange films increase linearly with the increase of the cation radius as a result of large cations interacting with more sulfonate groups, which leads to a further stabilization of the ionic cross-links and a reduction in the side-chain mobility.[93]

3.3 Properties of Nafion films

Extensive studies have focused on various properties of Nafion films and membranes, including water uptake and water transport, proton conductivity, gas permeability, mechanical strength, thermal stability, and chemical stability.[11] These studies have helped to advance the understanding of Nafion films and have contributed to the development of new and improved materials for various applications. Transport processes in Nafion involve multiple mechanisms and species that move through the matrix at various time and length scales. These processes are often interrelated and have been studied using a diverse range of diagnostic techniques that offer complementary data to identify and comprehend the governing mechanisms and structure-function relationships. In this thesis, the emphasis will be placed on the examination of specific transport properties, namely water transport and proton transport, as these properties have significant implications for electrochemical applications.

3.3.1   Water transport

Understanding the water transport behavior, including diffusion and uptake, in Nafion films and membranes is crucial for optimizing their performance in various applications. Here, it is important to consider that Nafion comprises hydrophilic domains containing sulfonic acid groups that attract and hold water molecules, as well as hydrophobic domains that consist of fluorocarbon chains that repel water. As a result, water diffusion in Nafion is a complex process that involves both the

transport of water molecules through the hydrophilic domains of the membrane and the diffusion of water clusters or aggregates through the hydrophobic domains.

As depicted in Figure 3.10a, as water transports through the material, the nanostructured morphology of Nafion facilitates both the swelling and growth of water at the nanoscale, as well potential dissolution of the polymer chains, while also providing a pathway for water molecule movement. The time required to reach equilibrium water uptake at a given humidity level provides insight into the time scale of water transport and interactions within the polymer (Figure 3.10b).[11]
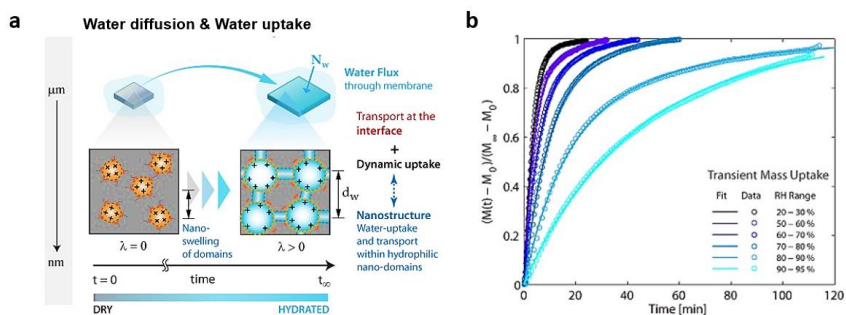

Figure 3.10 (**a**) Schematic comparison of water diffusion and uptake in Nafion films. (**b**) Dynamic-vapor-sorption curves at different humidity intervals showing the normalized mass change with time. Reproduced from Ref.[11]

In general, water transport and the hydration state are closely correlated. To quantify this hydration state, the water uptake (WU, %) is commonly expressed as

$$\text{WU} = \frac{W_w - W_d}{W_d} \times 100 \qquad 3.1$$

where W_w and W_d are the weights of the humidified and dry Nafion membranes, respectively. The hydration number λ, defined as the number of water molecules per sulfonic acid group, is given by

$$\lambda = \frac{\text{WU} \times 10}{\text{IEC} \times \text{MW}_w} \times 100 \qquad 3.2$$

where IEC is the ion-exchange capacity of the membrane (e.g., for Nafion 117 membranes, IEC = 0.91 meq H$^+$ g^{-1}), and MW$_w$ is the molecular weight of water (18.01 g mol^{-1}).[94] A step-by-step mechanism has been established for the process of water uptake within Nafion membranes and involves different hydration levels, expressed in terms of this hydration number λ, with λ = 0 being the dry state, λ = 1-3 being the low hydration level with isolated water molecules within Nafion, and λ > 3 being the high hydration level with H-bonded water molecule clusters (Figure 3.11). The molecular surroundings of water molecules, protonic substances, and polar groups are analyzed in detail based on the hydration number of the membrane.[94]
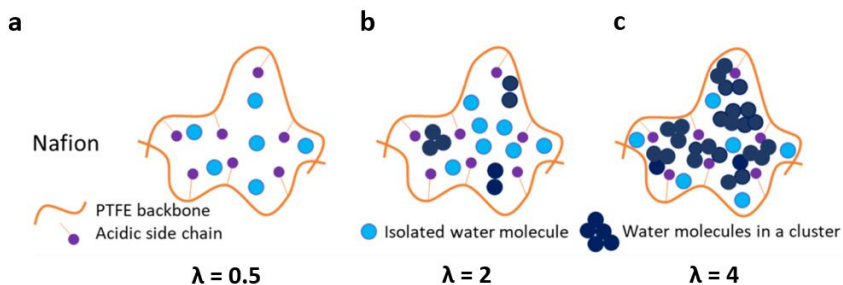

Figure 3.11 Schematic representation of water transport in Nafion 117 membranes at 70 °C. At λ = 0.5, few water molecules are included in a cluster and most water molecules are located in the vicinity of ionic functions. At λ = 2, only 20% of water molecules are included in clusters. At λ = 5, 70% of water molecules are included in clusters, respectively. Reproduced from Ref.[94]

NMR studies of Nafion have revealed the dynamic water behavior in terms of the relaxation time, which refers to the time it takes for the nuclear spin system within a sample to return to its equilibrium state after being perturbed by an external magnetic field. The relaxation time of Nafion typically increases with increasing hydration (λ) (from ~10 to 200 ms), and temperature. At low hydration levels, the molecular movement of water is dominantly affected by the acidity and mobility of the SO$_3$H groups to which the water molecules are coordinated, making water reorientation easier in confined hydrophilic domains, as proved by the low NMR

relaxation time. At higher hydration levels, the water transport behavior is more influenced by the size of the hydrophilic domains and approaches that of bulk-water.[95]

In practical applications, the water uptake and diffusion properties of Nafion can be influenced by a range of factors, including temperature, pressure, and the presence of other molecules or ions. For example, higher temperatures can increase the mobility of water molecules and lead to faster diffusion, while the presence of other ions can compete with the sulfonic acid groups for water molecules and reduce water uptake.

3.3.2 Proton transport

Owing to its remarkable ionic conductivity, ion transport within Nafion films and membranes has been extensively studied over the past ~3 decades. The transport of water and ions, particularly protons, in Nafion is closely correlated and is illustrated below in Figure 3.12.
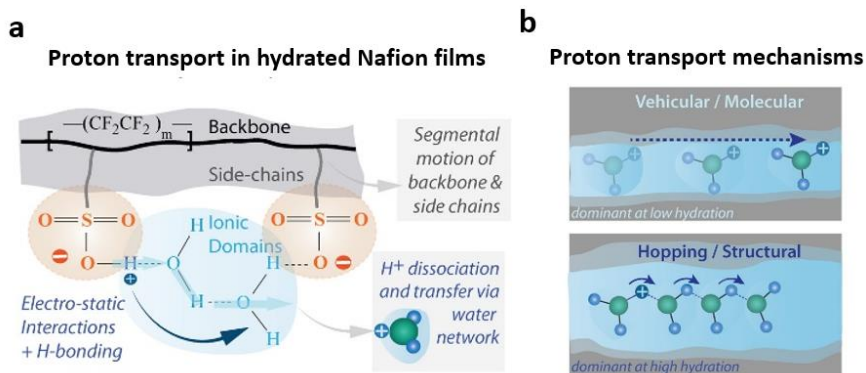

Figure 3.12 Proton conduction mechanism in hydrated Nafion membranes. (**a**) Chemical structure and key structural factors influencing the proton transport, (**b**) Illustration of vehicular/molecular and hopping/structural mechanisms for proton conduction in Nafion. Reproduced from Ref.[11,96–98]

The transport of protons depends not only on the presence of water, but also on the nature of water, its interaction with the SO_3^- groups, the length and hydrophilicity of the side-chain, and the movements of the polymer chains (Figure 3.12a). This results in a complex process of proton conduction that involves multiple sequential steps and interrelated processes. The process begins with the dissociation of protons and the formation of ion-pairs with water or solvent at the molecular scale, followed by water-mediated transport through hydrated domains at the nanoscale and mobility within the water network at the mesoscale, where the overall macroscopic conductivity is extensively influenced by restrictions imposed by the internal tortuosity. The proton conduction in Nafion is typically due to two main mechanisms: vehicular and hopping mechanisms. At low hydration, the vehicular mechanism is dominant and the proton conductivity is realized through the sluggish transport of solvated protons due to the relatively large steric hindrance and incomplete hydrogen-bond network (Figure 3.12b). At high hydration, the hopping mechanism dominates and involves a series of proton-transfer reactions (bond breaking and forming) across an array of water molecules interacting via hydrogen bonds. (Figure 3.12b). This hopping requires a faster rotation and reorientation of water molecules, which contributes to promoted proton conduction because the proton that enters the network is not the one that goes out.[99]

The proton conductivity of Nafion ionomers can be measured using various techniques, such as electrical impedance, dielectric spectroscopy, or indirectly through self-diffusion. However, the self-diffusion measurement only provides vehicular conductivity and fails to account for hopping/structural diffusion. The ionic conductivity can be calculated by determining the resistance (R), either in the plane or through the thickness of a film, and converting it to conductivity (κ) by considering the transport length (L) and cross-sectional area (A):

$$\kappa = \frac{L}{R \times A} \qquad\qquad 3.3$$

Studies on Nafion conductivity have looked at factors such as hydration, thickness, interfacial resistance, pretreatment, annealing, compression, stretching, and EW

effects. It has been shown that conductivity increases as the EW decreases, a trend that is more pronounced at higher hydration levels and temperatures due to the higher water uptake of low EW Nafion membranes.[11,100,101]

The proton conductivity of Nafion films or membranes is also strongly dependent on the water content within them. The water molecules facilitate proton transport by acting as a medium for the movement of protons between the sulfonic acid groups in the membrane. Therefore, the higher the water content, the higher the proton conductivity of the membrane (Figure 3.13a). However, there is a limit to the amount of water that can be held by Nafion. At low water content, the sulfonic acid groups may not have sufficient water molecules to facilitate proton transport, leading to a decrease in proton conductivity. At very high water content, the water molecules may begin to cluster together and impede the movement of protons, leading to a decrease in proton conductivity.
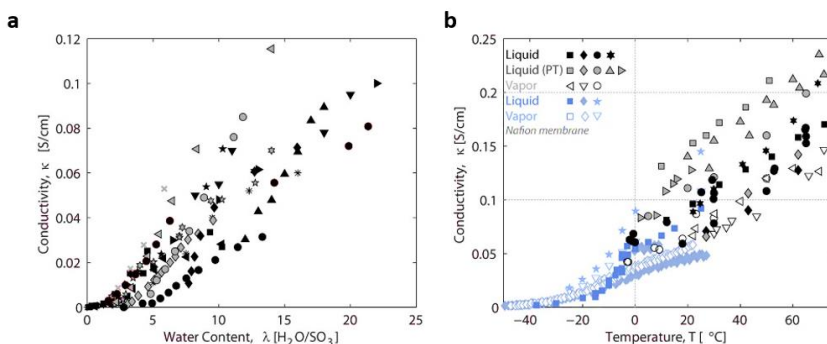
Figure 3.13 The effects of water content (**a**) and temperature (**b**) on conductivity of Nafion films or membranes. Adapted from Ref.[11]

The temperature also plays a critical role in the proton conductivity of Nafion. As the temperature increases, the mobility of water molecules and protons in the membrane increases, resulting in a higher proton conductivity. This temperature dependence is related to the activation energy required for proton transport in the membrane (Figure 3.13b).[11]

Overall, the water content and temperature have a significant impact on the proton conductivity of Nafion films or membranes. The optimum water content and temperature range for maximum proton conductivity depend on the specific application and operating conditions of Nafion films or membranes. In the present work, all electrocatalysis measurements are performed at room temperature and under exposure to liquid water. Particularly, in CO_2 electrolysis the availability of water molecules and protons is of great importance to the local microenvironment near catalysts.

3.4   Applications of Nafion in CO_2 electrolysis

In the final section of this chapter, the two main applications of Nafion ionomers in CO_2 electrolysis are introduced. Namely, these take the form of: i) Nafion ionomer dispersions used for producing catalyst inks that are deposited onto solid supports to form catalysts layers, and ii) the application of Nafion films for modulating the local reaction environment. While the former approach is extremely common in the field, such preparations naturally lead to the latter effects, though they are often not considered or understood in detail.

3.4.1 The usage of Nafion in preparing catalyst layers

As mentioned above, Nafion is the most widely used ionomer for preparing catalyst inks and catalyst layers (CLs) in various electrochemical applications. CLs are normally fabricated by casting the catalyst inks or slurries on conductive substrates, followed by a drying process. Catalyst inks are usually prepared by uniformly mixing solid catalyst powders, solvents, and Nafion ionomer into dispersions. In such catalyst dispersions, Nafion ionomers help to improve the dispersity of catalyst particles. Despite effective dispersion efforts, the complex interactions between catalyst, Nafion ionomer, and solvent can still lead to the presence of undispersed primary and secondary agglomerates. For instance, in the most commonly used water/alcohol (1-propanol, isopropanol, methanol or ethanol)-based catalyst inks, primary catalyst agglomerates surrounded by ionomer (known

as primary catalyst-ionomer agglomerates), primary ionomer agglomerates that are not absorbed, and secondary agglomerates formed by primary agglomerates may exist (Figure 3.14).[85] During the film and drying process, these primary and secondary agglomerates assemble into a porous structure that forms the multiscale structure of CLs.
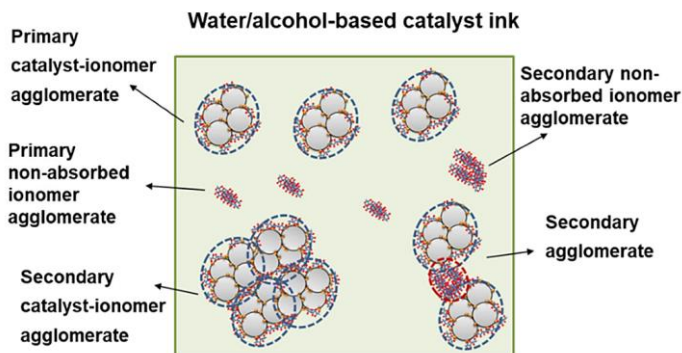

Figure 3.14 Illustration of the microstructure of the water/alcohol-based catalyst ink. In such catalyst ink, possible agglomerates include primary catalyst agglomerates surrounded by ionomer (i.e., primary catalyst-ionomer agglomerates), non-absorbed primary ionomer agglomerates, and secondary agglomerates formed by primary agglomerates. Copyright 2023, MDPI.[85]

The composition or microstructure of the catalyst ink affects a variety of macroscopic properties of the ink, including its rheology (viscosity and thixotropy), surface tension, and stability (material stability and colloidal stability). These properties play a significant role in the film process and the resulting deposited ink film, which in turn affects the multiscale structure of CLs. Therefore, the size, size distribution, and shape of various agglomerates, absorbed ionomer content on the catalyst, and the interface of catalyst/ionomer in the catalyst ink are crucial factors that can affect the performance and durability of CLs (Figure 3.15). [85]
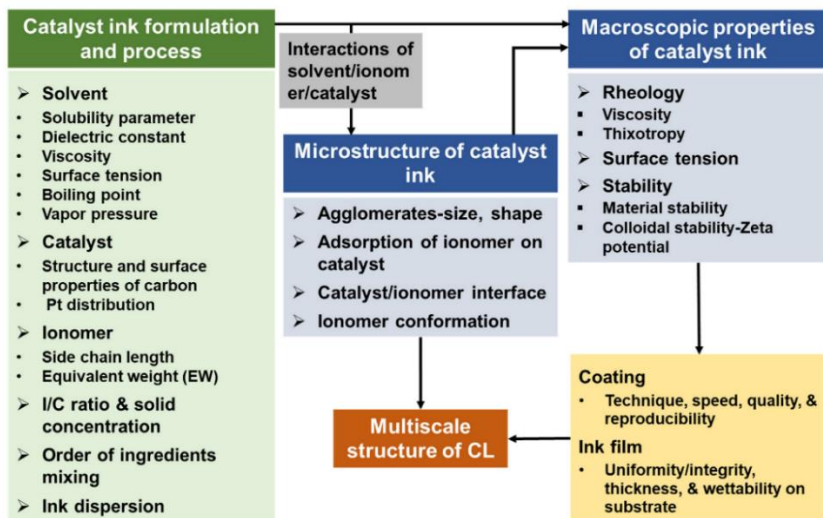
Figure 3.15 The microstructure and macroscopic properties of the catalyst ink, as well as the resulting CLs, are influenced by the catalyst ink formulation and preparation processes. Copyright 2023, MDPI.[85]

3.4.2 Tailoring local reaction environment with Nafion

Despite Nafion ionomers having been extensively used in preparing CLs for CO_2 electrolysis for decades, their effects on CO_2 electrolysis and underlying mechanisms remain poorly understood. Very recently, several studies reported the modification of Nafion ionomer films on Cu-based catalysts and its influence on electrochemical CO_2RR, especially for the production of multicarbon products.[12,21,74,102] Two main representatives are introduced in detail below.

Pelayo et al. presented a novel catalyst-Nafion ionomer bulk heterojunction (CIBH) architecture that enables the independent transport of gas, ions, and electrons (Figure 3.16).[21] This design consisted of a thin metal layer and an ultra-fine ionomer layer that possess both hydrophobic and hydrophilic properties, allowing for gas and ion transport at the nanometer to micrometer scale. As shown in Figure 3.16, the gaseous reactant availabilities in different gas-phase electrolysis scenarios were compared based on modeling. The Nafion ionomer layer is

estimated to facilitate gas flow until the gas is either converted at the catalyst surface or diffused into the electrolyte, promoting CO_2 diffusion on a larger scale of several micrometers. In contrast, for a typical catalyst configuration, CO_2 diffusion is limited to around 1 µm (as shown in Figure 3.16a-d).
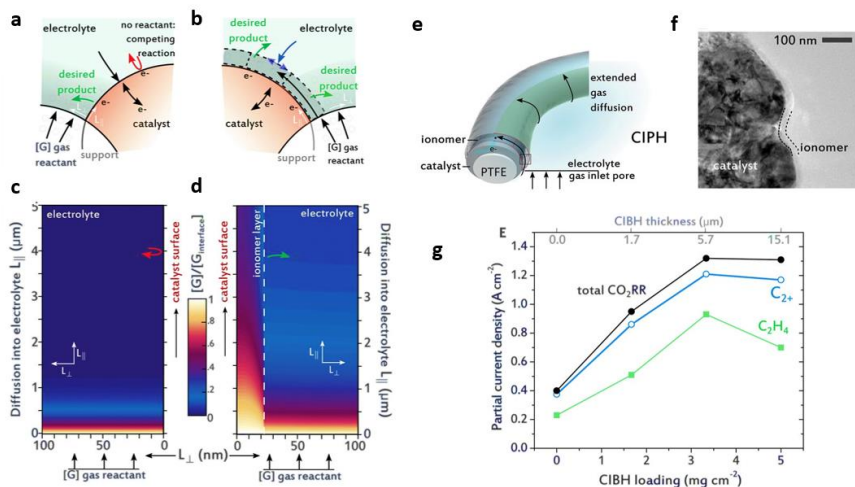

Figure 3.16 The limiting current in gas-phase electrocatalysis and ionomer gas-liquid decoupled transport channels on catalyst without (**a**) and with (**b**) Nafion films. Modeled gas reactant availability along the catalyst surface for standard (**a**) and decoupled (**b**) gas transport into a 5 M KOH electrolyte. The scheme (**e**) and TEM images (**f**) of the catalyst-Nafion ionomer bulk heterojunction (CIBH) highlight the internal structure and mechanisms. (**g**)The performance of CIBH with different loadings in CO_2 electrolysis. Reproduced from Ref.[21]

With this in mind, the authors utilized the Nafion ionomer layer that has both hydrophobic and hydrophilic properties, and it forms distinctive domains on the metal surface that enhance gas and ion transportation routes. This happens because gas transport is facilitated by hydrophobic domains present in the side chain, which leads to a more extensive gas diffusion (Figure 3.16e). On the other hand, water uptake and ion transport occur through hydrated hydrophilic domains. The result of this is an increase in the reaction interface regime from the

submicrometer to the several micrometer length scale, where gaseous reactants, ions, and electrons come together at catalytically active sites.

When operating at 800 mA cm^{-2} in a flow cell, the FE of H_2 was less than 10%, but the FE for ethylene was beyond 60%. The total partial current for C_{2+} products (ethylene, ethanol, acetate, and propanol) reached ~1.21 A cm^{-2} at a CIBH loading of 3.33 mg cm^{-2} (Figure 3.16g). According to previous findings from modeling analysis, the enhancement observed in the process could be attributed to a ~400-fold increase in the diffusion of CO_2 compared to that in the bulk electrolyte.

In another example, Kim and coworkers demonstrated a favorable modification of the microenvironment for CO_2 reduction by utilizing ionomer films with bilayer cation- and anion-conducting properties to manage the nearby pH levels (via Donnan exclusion) and CO_2/H_2O ratio (via ionomer characteristics).[12] By combining this customized microenvironment with pulsed electrolysis, the authors achieved even greater enhancements in the localized CO_2/H_2O ratio and pH, resulting in selective C_{2+} production. This approach resulted in a 250% increase in C_{2+} production (with 90% FE and only 4% for H_2) compared to static electrolysis over bare Cu (Figure 3.17).
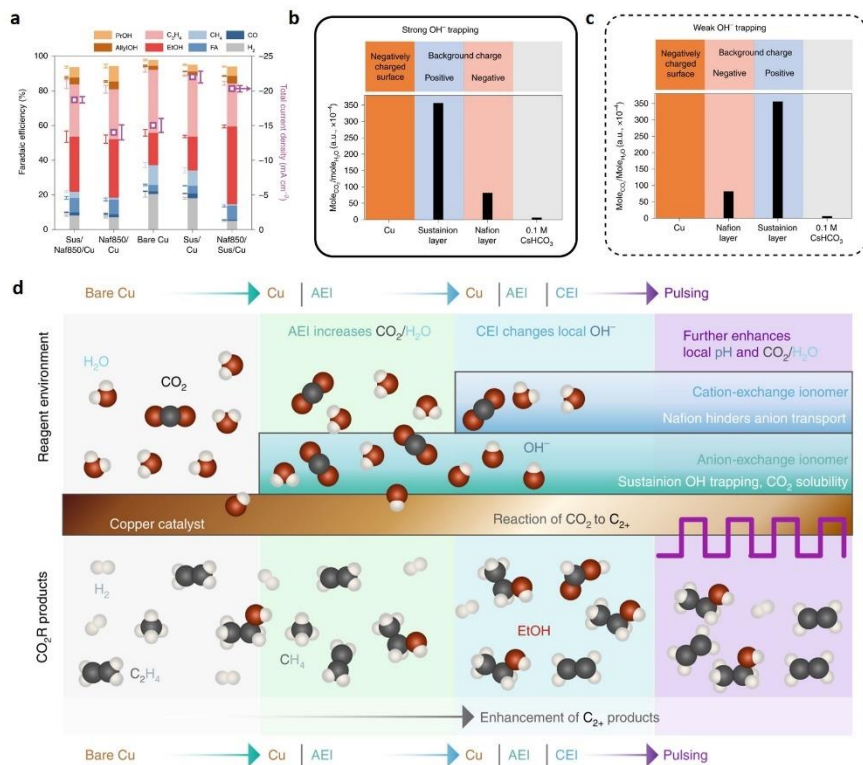
Figure 3.17 (**a**) CO$_2$R performance at −1.15 V vs. RHE using stacked ionomers on Cu in the presence of 0.1 M CsHCO$_3$ electrolyte. Schematic illustration of Naf850/Sus/Cu (top, **b**) and Sus/Naf850/Cu (bottom, **c**) in terms of local CO$_2$/H$_2$O ratio (dimensionless) and spatial charge configuration. (**d**) Schematic depiction of enhanced CO$_2$R using ionomers. Reproduced from Ref.[12]

In this case, a stacked double layer of ionomer film was introduced on Cu catalysts. As mentioned above, Nafion thin films possess a high proton-conductivity but hinder the transport of anions. Given this point of knowledge, the authors selected Nafion ionomer films as the outer layer, which was deposited on top of another inner anion-conducting layer of Sustanion (Sus) ionomer films on Cu catalysts. The net result of the bilayer was to increase local pH via trapping OH$^-$ generated in CO$_2$RR and meanwhile restrict the transport of buffering bicarbonate ions from bulk electrolyte into the microenvironment. As a consequence of the rise of local pH,

HER could be greatly suppressed and in turn CO_2RR could be enhanced (Figure 3.17). On the other hand, the inner layer of Sustanion, an anion conducting material, exhibits a much higher CO_2 solubility of ~703 mM compared to the value of ~36 mM for Nafion ionomer films. As a result, by synergistc control of both local pH and molar ratio of CO_2/H_2O using both cation and anion exchanging ionomer layers, a favorable microenvironment can be modulated for enhanced production of multicarbon products.

In summary, these two works highlighted the importance of further understanding the effects of Nafion on CO_2 electrolysis, thus inspiring the following research to improve the performance of CO_2 electrolysis by engineering of ionomer films on catalyst surfaces.

3.4.2 Discussion

Generally, the dispersion of catalyst materials – especially nanoparticles – in solvent can be promoted by Nafion ionomers because they consist of hydrophobic PTFE chains and terminal hydrophilic sulfonic acid groups. Uniform deposition of catalyst with reduced aggregation on electrodes increases electrochemically active surface areas, thus ensuring high catalytic site loading and promoting the overall activity, while strong molecule-solid interactions enable Nafion to serve as a robust binder between the catalytic nanostructures and the support, thereby enhancing long-term operational stability.[103] Furthermore, the large proton conductivity of Nafion, its hydrophobic/hydrophilic interactions, and mass transport characteristics can significantly affect the local environment in the vicinity of active sites.

It has been shown above that the catalyst ink formulation can modify the structures and properties of resultant CLs, as well as the properties of Nafion at the catalyst surface. Indeed, previous studies have recognized that interactions between Nafion ionomers and different solvents can alter inner network connectivity/tortuosity, conductivity, and water uptake of resultant Nafion thin films, which enables regulation of the environment surrounding the catalyst.[86,103,105,106] While it is expected that this can have a profound impact

on the reaction microenvironment, systematic analyses of the role of ink formulations on CO_2RR performance characteristics are lacking and clear design rules for optimization of activity, selectivity, and stability are required. Indeed, the ionomer/solvent formulations used in most studies are not rationally selected and vary considerably from one study to another. Consequently, analyses of catalytic function often neglect the critical role of Nafion in defining the reaction microenvironment and many reported catalysts risk being evaluated with non-optimal Nafion/solvent formulations that underestimate the true performance characteristics of the underlying surface. Therefore, the goal of this work is to systematically investigate the impact of Nafion/solvent formulations on Cu-catalyzed electrochemical CO_2RR, which is demonstrated in the following 3 chapters (Chapter 4 to 6).

Chapter 4. The impact of Nafion/solvent formulations on casted Nafion thin films

This fourth chapter begins with a literature review of Nafion/solvent formulations used for preparing catalysts inks for CO_2 electrolysis, which serves as both motivation for the experimental work, as well as a basis for selecting the range of compositions of catalyst inks to be studied. Thereafter, the preparation of spin-coated Nafion films is introduced, followed by a series of characterizations that explore how Nafion/solvent formulations affect the structure and properties of the prepared Nafion films.

4.1 Review of Nafion/solvent formulations in previous studies

The Nafion ionomer is the most widely used binder in numerous electrochemical applications. Here, in Table 4.1 we summarize the catalyst ink formulations from 20 recent publications concerning CO_2 electrolysis. Considering the diversity of CO_2 reduction products and variations of catalyst ink recipes across different research groups, 7 different major products, including $HCOO^-$, CO, methanol (MeOH), CH_4, C_2H_4, acetic acid (CH_3COOH), and ethanol (EtOH) are covered and these 20 publications were selected from more than 10 different research groups. In addition, both H-type cell and flow cell-based publications are involved.

As summarized in Table 4.1, a typical catalyst ink consists of three major ingredients: catalyst powder, Nafion ionomer dispersion, and solvent. The mass content of the catalyst material varies significantly among these studies, while the final mass loading of catalyst on the substrates is usually around 1 mg cm^{-2}.

Table 4.1 A summary of catalyst ink formulations, together with corresponding testing conditions and electrochemical performance, reported in recent publications

concerning electrochemical CO_2 reduction.[16,30,107–124] FE is short for Faradaic efficiency.

Catalyst	Major product	Substrate	Catalyst ink formulations $m_{catalyst}$ (mg)-V_{Nafion} (µL)-$V_{solvent}$ (µL)	Ref.
In H-type cells				
Pd₄Ag nanowires	HCOO-	glassy carbon	1-6-250 (ethanol)	[108]
Bi₂O₃ nanotubes	HCOO-	carbon paper, AvCarb P75	1-10-250 (50% water + ethanol)	[16]
Cu₂O nanocubes	C₂H₄	glassy carbon	4-100-1900 (80% water + isopropanol)	[125]
Ag nanopowder	CO	Sigracet 25 BC	10-10-1200 (50% water + isopropanol)	[126]
Sulfur-doped indium catalyst	HCOO-	Toray TGP-H-060 carbon paper	10-20-1000 (50% water + isopropanol)	[117]
CuO-CTAB	HCOO-	carbon fiber paper, Toray-03	1-0-1000 (ethanol)	[118]
CoPc–NH₂/CNTs	MeOH	carbon fibre paper, Toray 030	2-6-2000 (ethanol)	[119]
Copper(II) phthalocyanine	CH₄	glassy carbon disk	2-12-2000 (methanol)	[120]
NiPc–OMe MDE	CO	CFP (Toray, TGP-H-060)	2-17-1000 (ethanol)	[59]
Cu₅Sn₆ alloy	HCOO-	AvCarb MGL 190,	20-0-1000 (ethanol)	[30]
CumCeOx catalysts	C₂H₄	glassy carbon	4-10-400 (50% water + ethanol)	[127]
In flow type cells				
InP colloidal quantum dots	HCOO⁻	carbon cloth, CeTech W1S1010	0.24-10-600 (methanol)	[107]
Cu-based bimetallics	C₂₊	GDL, Sigracet 29 BC	3-3-1440 (isopropanol)	[110]
PDDA-functionalized Pd/C	CO	GDL, Sigracet 29 BC	10-10-1000 (isopropanol)	[111]
Cu, Ag, Sn	NA	Sigracet 29 BC GDL	25-20-3000 (isopropanol)	[112]
Cu nanosheets	CH₃COOH	Sigracet 29 BC GDL	25-20-3000 (isopropanol)	[113]
Cu powder	C₂₊	Sigracet 29 BC GDL	100-40-2500 (isopropanol)	[114]
AgSn/SnOx nanoparticles	HCOO⁻	Sigracet 25 BC	50-20-2400 (50% water + isopropanol)	[115]
Fluorine-modified Cu	EtOH, C₂H₄	GDL, YLS-30T	10-20-1000 (25% water + isopropanol)	[116]
Ni-PACN	CO	GDL, Sigracet 39BC	13-100-5000 (33% water + isopropanol)	[124]

It should be noted that although Nafion ionomer is of great importance for the durability of catalyst layers and electrodes, a few studies still choose Nafion-free catalyst inks.[30,118] The Nafion weight ratio, defined as the ratio of the mass of

catalyst materials to the total weight of solvent, is compared in Figure 4.1a. Regardless of electrochemical cell configuration, the calculated Nafion weight ratio ranges from 0 to 0.25 wt.%, implying a significant variation in Nafion usage across these studies.
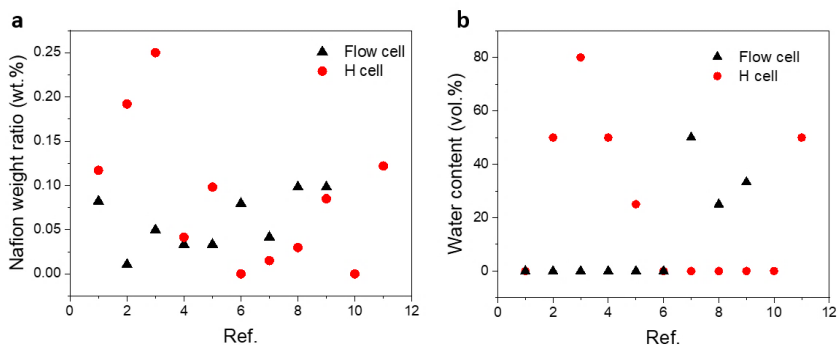

Figure 4.1 Analysis of Nafion weight ratio (**a**) and water content (**b**) in recently reported catalyst ink formulations (based on Table 4.1) for electrochemical CO_2 reduction. The x-axis is represents the different publications in randomized fashion for illustrative purposes, with the actual references are provided in Table 4.1.

The solvent composition of catalyst ink is also analyzed. Remarkably, 60% of publications use absolute alcohol as the solvent, while the rest use water/alcohol mixtures to disperse catalyst materials. The preference of water-free alcohol-based solvent is very likely due to the quick drying process when depositing catalyst inks that is enabled by the lower bolting points and higher vapor pressures of alcohols relative to water. Similarly, the water content, defined as the ratio between the volume of water and the total solvent volume, is estimated Figure 4.1b as another important parameter to evaluate Nafion/solvent formulations. For those water-containing inks, the water content varies from 20 to 80%. High water content inks are rarely used as the slow evaporation rate of water inevitably leads to long drying processes for preparing catalyst layers. Therefore, the frequently used water-containing inks are of less than ~50 vol.% H_2O.

In summary, after examining the Nafion weight ratio and water content of various catalyst ink formulations previously reported in the literature, we can draw the following conclusion: There is significant variation in the reported catalyst ink formulations across different publications and groups, and it is likely that these formulations were developed empirically, and in many cases with little consideration of the role of solvent formulation on eventual catalytic function. These results suggest that there are currently no established guidelines for designing catalyst ink formulations, particularly in terms of Nafion content and solvent composition. Furthermore, analysis of recent electrochemical CO_2RR literature reveals that the Nafion content in catalyst inks varies over a broad range, from 0 wt.% to 0.50 wt.%, while the water content in water/alcohol solvent mixtures ranges from 0 vol.% to 80 vol.% (Figure 4.1). The pervasive inconsistency in Nafion content and solvent composition within catalytic ink formulations reflects the poor understanding of their effects on electrochemical CO_2RR. To address these issues, systematic studies of Nafion/solvent ink formulations and their roles in CO_2 electrolysis are in urgent demand.

4.2 Preparation of casted Nafion thin films

As a starting point for understanding how ink formulations influence electrochemical CO_2RR, it is useful to first explore the roles of Nafion content and solvent composition on the structures and morphologies of deposited Nafion films. Previous studies of nanoscale Nafion films and microscale membranes have revealed that the dielectric constants of different solvents can alter the dispersion of Nafion ionomers in solution, which results in drastic structural changes of solution-derived Nafion films (Figure 4.2, also see Chapter 3). [86,103–105]

As shown in Figure 4.2, Nafion dispersions in low dielectric constant solvents (e.g., n-PrOH) lead to loose ionomer aggregates with linked sulfonic acid terminal groups. In contrast, high dielectric constant solvents (e.g., water) yield tightly packed aggregates with strong backbone interactions, resulting in improved inner network connectivity and reduced swelling upon Nafion film formation, as well as enhanced ionic conductivity and decreased water uptake.[86] Thus, we hypothesize that it

should be possible to tune the structure of Nafion films surrounding catalyst layers by adjusting both the water/n-PrOH ratios and total Nafion content within catalyst ink formulations, thereby allowing controlled modification of key properties that can affect the CO_2RR, such as thickness, ionic conductivity, mass transport coefficients, and local microenvironments (e.g., pH, CO concentration, and CO_2/H_2O ratio).
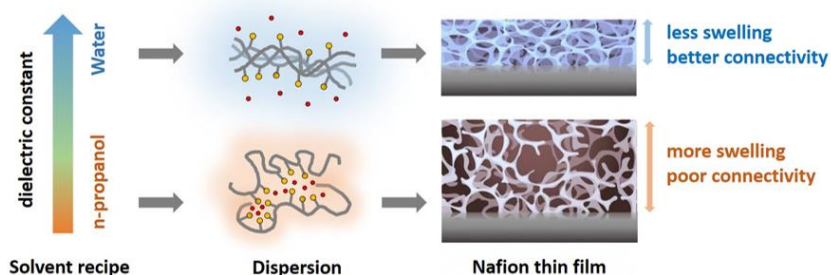

Figure 4.2 Schematic illustration of the effects of Nafion/solvent formulations on the resulting Nafion films based on previous studies.[78,86,105]

To verify the expected dependence of the properties of deposited Nafion films on ink formulations, we first examined pure Nafion films prepared by spin-coating dispersions containing different concentrations of Nafion and water on Si wafers (p-type, thickness: 525 µm). For this, formulations with seven Nafion weight fractions (0, 0.005, 0.025, 0.05, 0.125, 0.25, and 0.5 wt.%) in water/n-PrOH solvent mixtures containing four water volume fractions (0, 25, 50, and 75 vol.%) were investigated (Table 4.2). Thus, 28 ink formulations were prepared in total. These different compositions were selected to span the majority of ink compositions reported in the literature (Figure 4.1). As demonstrated in previous studies, annealing of as-prepared Nafion films is able to lock-in the internal structural differences caused by the varying Nafion/solvent formulations.[86] Thus, we annealed all freshly prepared Nafion films at 80 °C prior to all measurements presented in this thesis.

Table 4.2 All Nafion/solvent formulations investigated in this thesis for the production of Nafion dispersions. For water-containing formulations, n-propanol is used as the balance.

	Water Content (vol.%)			
	0	**25**	**50**	**75**
0	Sample 1	2	3	4
0.005	5	6	7	8
0.025	9	10	11	12
0.05	13	14	15	16
0.125	17	18	19	20
0.25	21	22	23	24
0.5	25	26	27	28

Nafion weight ratio (wt.%)

4.3 Structures and morphologies of casted Nafion thin films

We first examined the chemical structure of thus-prepared Nafion thin films on Si wafers. Fourier-transform infrared spectroscopy (FTIR) of Nafion films with different thicknesses can provide important insights into the chemical and structural properties of these films (Figure 4.3). Basically, all characteristic chemical bonds or functional groups within Nafion, including CF_2 units in the main chain, C-O-C bonds at the connections and SO_3^- groups at the terminal of side chains, were probed in the spectra. The C-F bonds are part of the fluorocarbon backbone of the polymer and are responsible for the high chemical stability of the films, as well as their hydrophobic and proton-conducting properties. When the film thickness is increased from 2.4 nm at 75 vol.% H_2O to 7.5 nm at 0 vol.% H_2O, the local environment around the C-F bonds can change, affecting the vibrational frequency and intensity of the C-F stretching band. Specifically, as the film thickness increases, the number of neighboring polymer chains and the degree of molecular ordering may increase, resulting in stronger intermolecular interactions between adjacent polymer chains. This can lead to changes in the molecular conformation and rigidity around the C-F bonds, causing a shift in the C-F stretching frequency to a higher value. As a result, the corresponding peaks for the vibrational modes of

v_{as} (CF$_2$) around 1155 cm^{-1} and 1230 cm^{-1} both constantly shift to larger wavenumbers with increasing film thickness.
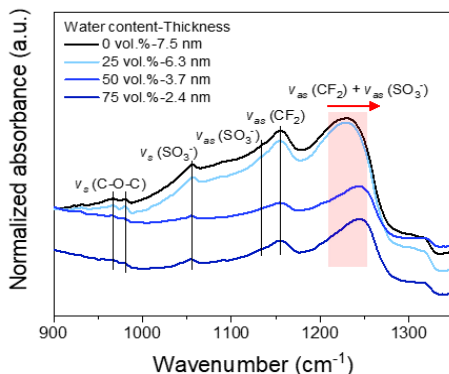

Figure 4.3 Fourier-transform infrared spectroscopy (FTIR) of Nafion films prepared with 0.25 wt.% Nafion dispersions with different water contents (0, 25, 50 and 75 vol.%). The thickness of Nafion films was measured by spectroscopic ellipsometry as introduced in Figure 4.8.

Next, AFM images in Figure 4.4 and Figure 4.5 show representative surface morphologies of four dry Nafion films prepared from 0.5 wt.% and 0.25 wt.% Nafion dispersions, respectively, containing four different water fractions on polished Si substrates. All measured films were uniform, though the surface roughness was the largest for the case of absolute n-PrOH (0.48 nm at 0.5 wt.% and 0.41 nm at 0.25 wt.%) and decreased with increasing water content from 0.35 nm (at 0.5 wt.%) and 0.36 nm (at 0.25 wt.%) at 25 vol.% to 0.13 nm (at 0.5 wt.%) and 0.12 nm (at 0.25 wt.%) at 75 vol.%, respectively (Figure 4.4 and Figure 4.5). Moreover, with increasing water content, the porous structures within the film became smaller with less swelling, as indicated by the 3D AFM images in Figure 4.4 and Figure 4.5, in agreement with the expectation for higher network connectivity and smaller pore dimensions in films derived from higher water content solvents (as illustrated in Figure 4.2).
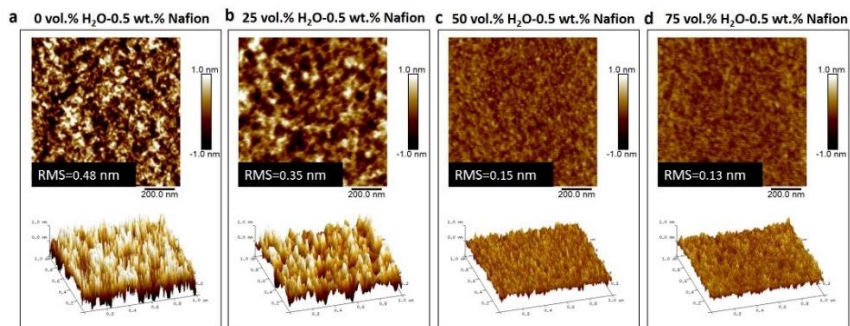
Figure 4.4 Atomic force microscopy (AFM) images of Nafion films prepared by spin-coating Nafion dispersions (made of commercial Nafion dispersions and solvent of water/isopropanol) on Si wafers. These dispersions contain 0.5 wt.% Nafion and different water contents (0 vol.%, 25 vol.%, 50 vol.%, and 75 vol.%).
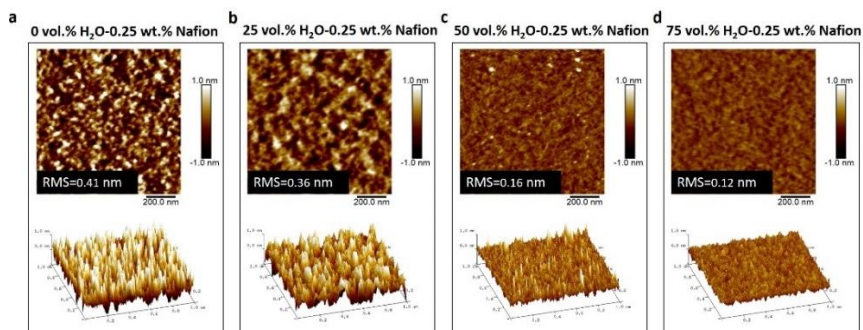

Figure 4.5 Atomic force microscopy (AFM) images of Nafion films prepared by spin-coating Nafion dispersions (made of commercial Nafion dispersions and solvent of water/isopropanol) on Si wafers. These dispersions contain 0.25 wt.% Nafion and different water contents (0 vol.%, 25 vol.%, 50 vol.%, and 75 vol.%).
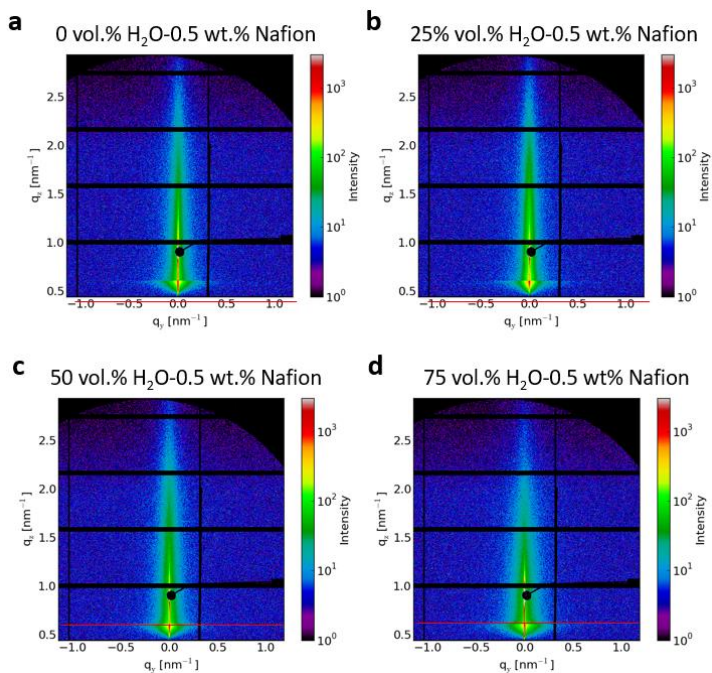
Figure 4.6 2D GISAXS data of Nafion films prepared by spin-coating dispersions (made of commercial Nafion dispersions and solvent of water/isopropanol) on Si substrates. These dispersions contain 0.5 wt.% Nafion and different water contents (0 vol.%, 25 vol.%, 50 vol.%, and 75 vol.%). The positions for performing the horizontal line cuts used to produce Figure 4.7 are denoted with the red line.

The morphological differences observed by AFM are also confirmed by GISAXS measurements (Figure 4.6) of Nafion films. In small-angle X-ray scattering, the *q* value refers to the magnitude of the scattering vector, which is defined as the difference between the wave vector of the incident X-rays and that of the scattered X-rays. The scattering vector, *q*, is related to the scattering angle, *θ*, and the X-ray wavelength, *λ*, by the equation:

$$q \ = \ \frac{4\pi}{\lambda} \ \sin\frac{\theta}{2} \qquad\qquad 4.1$$

The *q* value provides information about the size, shape, and distribution of structures or particles in a sample. Small *q* values correspond to large structures, while large *q* values correspond to small structures.

As analyzed in Figure 4.7, the horizontal line cuts of 2D GISAXS data revealed a shift of the q_y value of the domain structure from 0.025 to 0.075 nm^{-1} and, thus, a decreasing pore size as the water content was increased from 0 vol.% to 75 vol.%. The smaller pore size and more densely packed structures are consistent with better inner connectivity and suggest higher proton conductivity of Nafion films derived from higher water content solvents.[87]
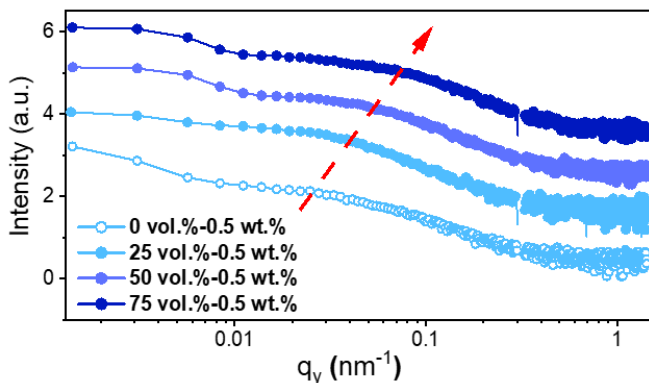
Figure 4.7 Horizontal line cuts of the 2D GISAXS data (from Figure 4.6) of Nafion films prepared with 0.5 wt.% Nafion solutions with different water contents.

In summary, the solvent composition of Nafion dispersions drastically affects the morphology and structure of the prepared Nafion films. Increasing water content in Nafion dispersions leads to less swelling and smoother Nafion films with smaller porous structures compared to those prepared from water-free or low-water-content dispersions.

4.4 Thicknesses of casted Nafion thin films

The thickness of Nafion films is another important characteristic parameter, which is linked to the transport efficiency of species such as CO_2 gas, protons, buffering ions, reaction intermediates and products between the catalyst surface and the bulk electrolyte.

Ellipsometry is a powerful and non-destructive optical technique that can be used to measure the thickness of thin films with high precision. It works by measuring the change in polarization of light as it reflects off various interfaces on and within a sample. As light reflects from the upper and lower interfaces of a thin film, its polarization state changes and interference fringes are generated. These changes are governed by the optical properties of the material and its thickness, which can be detected using a spectroscopic ellipsometer (as depicted in Figure 4.8a) and subsequently modelled.
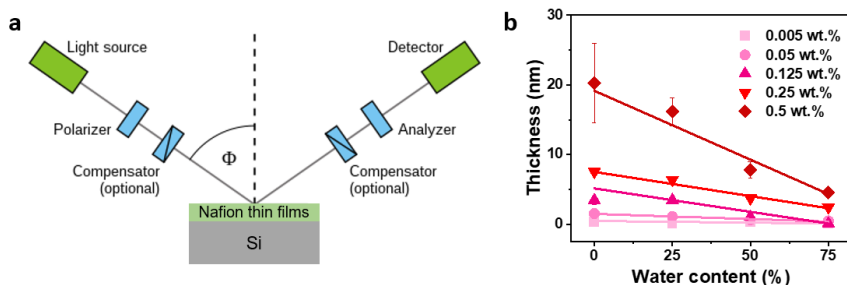
Figure 4.8 (a) Schematic depiction of a spectroscopic ellipsometer. **(b)** Estimated thicknesses of Nafion films prepared with different Nafion/solvent formulations using spectroscopic ellipsometry.

The blank Si substrates were first characterized via ellipsometry and the thickness of the native oxide (SiO_2) layer was measured to be ~2 nm. Then, dry Nafion films spin-coated on Si substrates were subject to ellipsometry investigations. These films were produced from Nafion dispersions comprising five Nafion weight ratios and four water volume fractions (Figure 4.8b). A multilayer model for Si/SiO₂/Nafion, consisting of library functions for the Si substrate and native oxide (Si: Si-JAW;

SiO$_2$: SiO$_2$_JAW), as well as a Cauchy model for Nafion, was built to fit the ellipsometry data and to estimate the thickness of as deposited Nafion films.

Film thicknesses increased with increasing Nafion content: for the case of 0 vol. % water (75 vol.% H$_2$O) the thickness increased from 0.3 to 20 nm (0.1 to 4.5 nm) as the Nafion content increased from 0.005 to 0.5 wt.%. As indicated by these values, the Nafion film thickness decreased with increasing the water fraction. For example, the measured thickness of films prepared with 0.5 wt.% Nafion decreased from 20 nm at 0 vol.% H$_2$O to 4.5 nm at 75 vol.% H$_2$O.

Such a trend of thickness was further verified by the FTIR spectra in Figure 4.3 as the change in thickness can significantly affect the position and absorbance of characteristic peaks of the infrared spectra of Nafion films. As the thickness reduced from 7.5 nm at 0 vol.% H$_2$O to 2.4 nm at 75 vol.% H$_2$O, the major peak assigned to vibrational modes of V$_{as}$ (CF$_2$) and V$_{as}$ (SO$_3^-$) constantly shifted from 1230 cm^{-1} to 1245 cm^{-1}, and its corresponding absorbance continuously decreased as well. This finding is in good agreement with previous studies[128].

These results indicate much thinner films can be obtained with formulations of low Nafion and/or high water content. Furthermore, a generally weaker dependence of thickness on the Nafion weight ratio with increasing water content is observed.

4.5 Water uptake of casted Nafion thin films

As the prepared Nafion films are all dehydrated in the annealing treatment, they will take in water molecules when exposed to water or immersed in aqueous electrolytes. Such water uptake behavior of Nafion films has been introduced in Chapter 3, and is evaluated here by measuring the water content within Nafion films. In particular, to determine the water content, the thicknesses of Nafion films were recorded in an *in situ* ellipsometry cell (fixed incidence angle: 70.23°) at different humidities. The humidity was controlled to be 0 and 100% by first purging the cell with N$_2$ (99.9999%, Linde) at a flow rate of 400 sccm for 1 h (0% humidity), after which humidified N$_2$ gas that was bubbled through a 25 °C (room temperature) water bath was fed to the cell for 1 h (100% humidity).

The change of thickness (ΔT) between 0% (T_0) and 100% (T_{100}) humidity was used to derive the swelling factor (α) and water content (μ) according to the equations below:

$$\alpha = (T_{100} - T_0)/T_0 = \Delta T/T_0 \qquad\qquad 4.2$$

$$\mu = \frac{\alpha\, EW_{Naf}\, \rho_{H_2O}}{\rho_{Naf}\, M_{H_2O}} \quad [=]\ \text{mol}\ H_2O/\text{mol}\ SO_3^- \qquad 4.3$$

where EW_{Naf} is the equivalent weight (1100 g polymer per mole SO_3^-) of Nafion ionomer dispersion, ρ_{Naf} is the density of Nafion ionomer (2.075 g/cm^3), and ρ_{H_2O} and M_{H_2O} are the density and molar mass of water, respectively.[129] The corresponding molar water concentration within the Nafion films, c_{H_2O}, is thus:

$$c_{H_2O} = \frac{\mu\, \rho_{Naf}}{EW_{Naf}} = \frac{\alpha\, \rho_{H_2O}}{M_{H_2O}} \qquad\qquad 4.4$$

Quantitative values were obtained for the Nafion films prepared from 0.5 wt. % Nafion dispersions as a function of the solvent composition, as reported in Table 4.3. We note that such measurements were not possible for the complete set of samples due to the ultra-thin nature of films produced from dispersions possessing low Nafion fractions.

Figure 4.9a shows that the swelling fraction of Nafion films decreased as the water volume fraction in Nafion dispersions increased from 0 to 75 vol.%. This suggests that Nafion films made from water-free or low-water-content Nafion dispersions have more swollen and porous structures compared to those made from high-water-content Nafion dispersions, which is consistent with the morphological variations observed in AFM images in Figure 4.4 and Figure 4.5.

Moreover, by measuring the difference in thickness between dehydrated and hydrated Nafion films, the water content was determined and found to exhibit a similarly decreasing trend with increasing water volume fraction in the solvent (Figure 4.9b). It should be noted that water serves as the proton source in CO_2 electrolysis, and therefore the local concentration of water around catalysts is

strongly related to competing HER. A detailed discussion of the local molar ratio between CO_2 and water is presented in Section 5.6 of Chapter 5.

Table 4.3 *In situ* ellipsometry measurement of thickness changes of Nafion films prepared by spin-coating of Nafion solutions containing four different water contents. Swelling fraction, water content and water concentration in Nafion films were calculated based on variations in thickness with humidity.

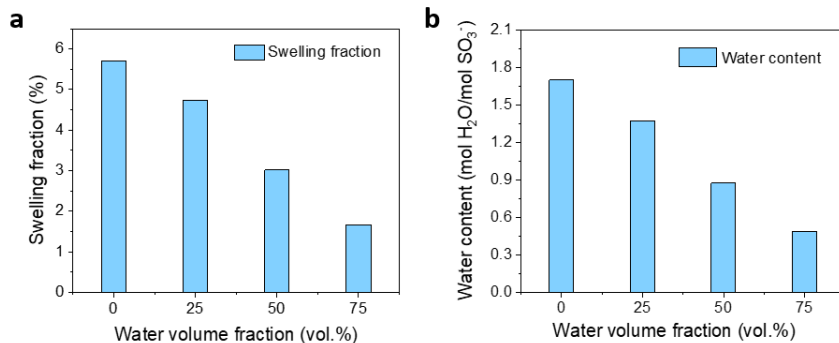| Water content (vol. %)	Thickness (nm)		Swelling fraction (%)	Water content (mol H_2O/mol SO^{3-})	Water concentration (M)
	dry N_2, 1h	humidified 25 ^{o}C, 1h			
0	24.25	25.64	5.7	1.7	3.1
25	14.54	15.23	4.7	1.4	2.6
50	7.59	7.82	3.0	0.9	1.6
75	3.06	3.11	1.7	0.5	0.9

Figure 4.9 Effect of solvent composition on water uptake of spin-coated Nafion films on Si. Plots of the calculated swelling fraction (**a**) and water content (**b**) of Nafion films according to *in situ* ellipsometry tests versus the water volume fraction in Nafion dispersions.

Chapter 5. Defining the roles of Nafion/solvent formulations in copper-assisted CO_2 electrolysis on carbon paper substrates

In the fifth chapter, systematic investigations of the impact of Nafion/solvent formulations on Cu-catalyzed CO_2 electrolysis on carbon paper substrates are demonstrated from the following perspectives: the structure of the catalyst layers, the CO_2 electrolysis performance (activity, selectivity, and stability), and the local reaction environment (local concentration of CO_2 and H_2O and surface adsorption of intermediates).

5.1 Introduction

In this chapter, we systematically study the impact of Nafion/solvent formulations on Cu-catalyzed electrochemical CO_2RR. Using commercial CuO nanoparticles as the model pre-catalyst, we demonstrate that both the selectivity and stability of the resulting CLs are significantly affected by the Nafion/solvent formulation. In particular, we find that the presence of Nafion is crucial for the morphological stabilization of the electrodes, while the Nafion content and water/alcohol composition significantly impact the activity for multicarbon product formation. The presence of Nafion on the catalytic surface has a significant influence on the local reaction environment, where control of the CO_2 and H_2O reactants, as well as the CO intermediate, is essential for suppressing both HER and C_1 production, while promoting at the same time C-C coupling to form C_{2+} products.[21,130] With this in mind, we correlate systematic electrochemical analyses of catalytic function with *ex situ* structural characterization and *in situ* Raman spectroscopic monitoring of

CO$_2$RR on CLs to investigate the influence of Nafion/solvent formulations on activity, selectivity, and stability.

5.2 Properties of catalyst layers deposited on carbon paper

Having characterized the influence of solvent and Nafion ionomer concentrations on resulting Nafion films, we then introduced catalytic particles to the ink formulations and investigated the properties of complete CLs. As highlighted in Chapter 2, Cu-based catalysts are attracting increasing attention due to their versatility in producing value-added multicarbon products from CO$_2$ electroreduction. Hence, throughout this thesis commercial CuO nanoparticles with the size of ~50 nm were chosen as model pre-catalysts that can be reduced to catalytically active metallic Cu under cathodic bias. Such nanoparticles offer high active site concentrations, resulting from their large surface-to-volume ratio. Moreover, it is well known that oxide-derived Cu catalysts are able to generate superior catalytic activity in CO$_2$ electrolysis compared with pristine metallic Cu catalysts for generating C$_{2+}$ products.[131–133]

Carbon paper substrates, normally made of carbon fibers, have porous microstructures and are extensively used in electrochemical applications. The carbon paper is therefore selected as the supporting substrate and electron conductor for preparing working electrodes. All working electrodes were prepared by drop-casting uniformly dispersed catalyst inks on a piece of carbon paper (1 cm x 2 cm) on a heating plate (80 °C), followed by annealing in air for 10 min. The mass loading of CuO powder and the effective working area were kept constant at 0.5 mg cm^{-2} and 1 cm^2, respectively. All electrodes and CLs prepared with varied Nafion/solvent formulations are denoted by "Water content-Nafion weight ratio". For instance, the one prepared with inks containing 50 vol.% H$_2$O and 0.5 wt.% Nafion is labeled as "50 vol.% H$_2$O-0.5 wt.% Nafion".

As presented in Figure 5.1 and Figure 5.2, large agglomerates of CuO nanoparticles were observed in the scanning electron microscopy (SEM) images of CLs fabricated with Nafion-free catalyst inks. In sharp contrast, for those CLs

prepared with Nafion-containing inks, large agglomerates were absent. This suggests that the use of Nafion ionomer is crucial for ensuring that CuO nanoparticles are uniformly dispersed on carbon paper substrates and for preventing the formation of aggregates. The increase of Nafion content from 0.005 to 0.5 wt.% did not lead to any obvious morphological changes of CLs.
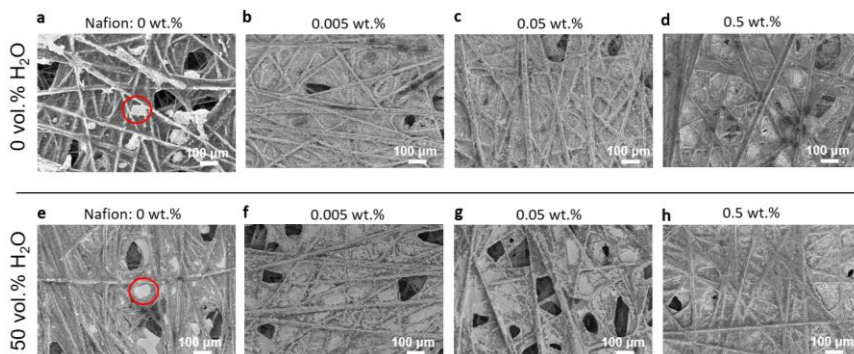

Figure 5.1 Scanning electron microscopy (SEM) images of catalyst layers deposited on carbon paper prepared with inks containing 0 vol.% (**a-d**) and 50 vol.% (**e-h**) water and different Nafion weight ratios (0, 0.005, 0.05 and 0.5 wt.%). Red circles indicate the existence of large aggregates on carbon paper, which are only observed in the absence of Nafion in the catalyst ink.
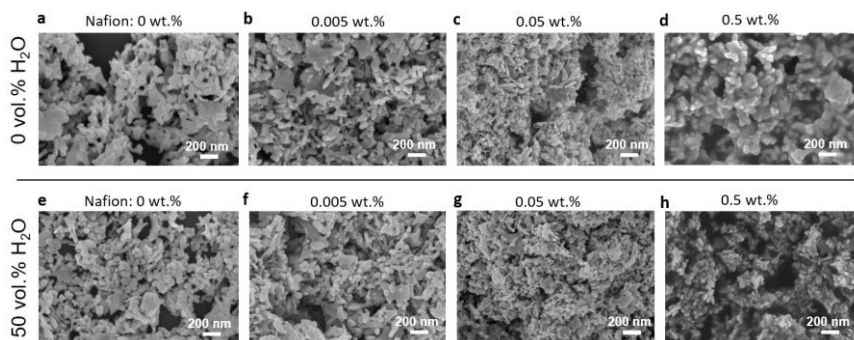

Figure 5.2 Magnified SEM images of catalyst layers deposited on carbon paper prepared with inks containing 0 vol.% (**a-d**) and 50 vol.% (**e-h**) water and different Nafion weight ratios (0, 0.005, 0.05 and 0.5 wt.%).

In magnified SEM images (Figure 5.2), CuO nanoparticles were found to have largely random shapes with an average size of ~50 nm. Remarkably, for the CLs produced from inks of the highest Nafion content of 0.5 wt.% transparent Nafion film layers were recorded around the surface of CuO nanoparticles. On the other hand, the variation of water content appears to have a negligible impact on the dispersity of CuO nanoparticles on carbon substrates.

Further structural characterizations revealed the particles to comprise the pure monoclinic phase of CuO (JCPDS No. 80-1268, Figure 5.3). After adding Nafion ionomer into catalyst inks, no significant changes to the XRD data were observed, although SEM images showed clear indications for the presence of Nafion films on CLs deposited from 0.5 wt.% Nafion solutions. The XRD data of working electrodes prepared from these catalyst inks indicated the existence of both the CuO phase and the underlying carbon paper substrate.
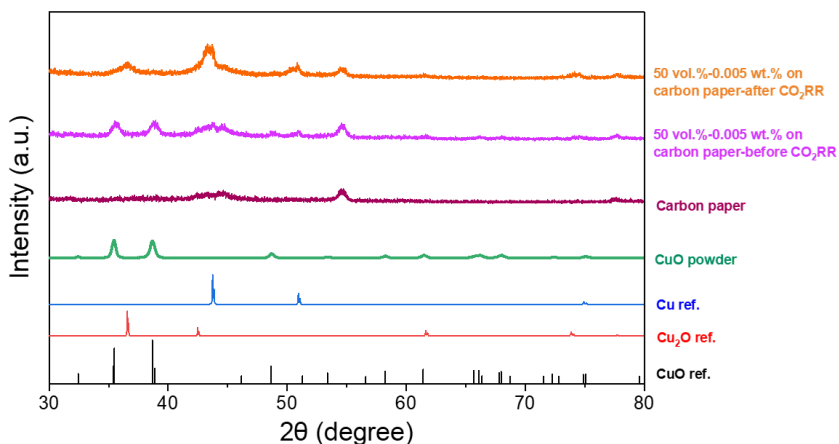
Figure 5.3 X ray diffraction (XRD) data of references (CuO, Cu_2O, and Cu) from database, the blank carbon paper substrate, and the best-performing electrode before/after CO_2 electrolysis prepared with optimal catalyst ink formulations (50 vol.% H_2O-0.005 wt.% Nafion on carbon paper).

Notably, XPS revealed increasing attenuation of the Cu 2p signals with increasing Nafion content from 0 to 0.5 wt.%. No chemical changes were observed within the

Cu 2p core level region, indicating that the CuO is preserved upon contact with Nafion. However, for the highest Nafion content of 0.5 wt.%, photoemission from the catalyst particles was nearly completely suppressed (Figure 5.4). Given that the XPS sampling depth through organic material is on the order of ~10 nm,[134] these findings imply that formulations of higher Nafion weight ratios yield increasing thicknesses of Nafion atop CuO particles at the nanometer scale. Consistent with this conclusion, C 1s and F 1s photoemission intensities associated with the C-F_2 and C-O bonding in Nafion increase with increasing Nafion content.
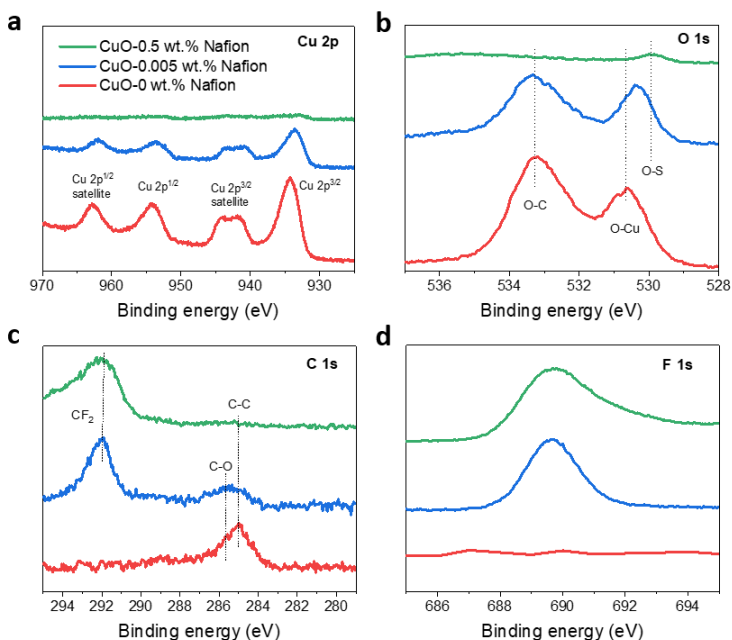
Figure 5.4 X ray photoelectron spectroscopy (XPS) data of catalyst layers prepared with inks containing 50 vol.% H_2O and different Nafion weight ratios (0, 0.005 and 0.5 wt.%). (**a**) Cu 2p spectrum. (**b**) O 1s spectrum. (**c**) C 1s spectrum. (**d**) F 1s spectrum.

TEM imaging was performed to verify the presence of Nafion on catalyst particles, as well as the qualitative dependence of film thickness on solvent composition. In particular, TEM images from CuO nanoparticles deposited from solutions

containing 0.5 wt.% Nafion and various water/n-PrOH solvent ratios were acquired. Consistent with the spectroscopic ellipsometry data described above, Nafion films were observed around CuO nanoparticles for all samples and the thickness of Nafion films was reduced with increasing water content. The consistent trend of decreasing film thickness with increasing water content indicates that the impact of formulations on deposited Nafion films persists when CuO nanoparticles are introduced to form catalyst inks.
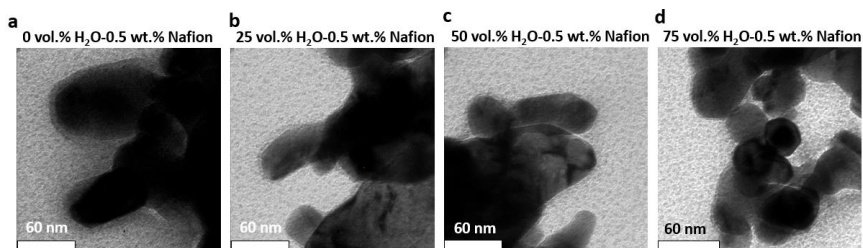

Figure 5.5 Transmission electron microscopy (TEM) images of CuO nanoparticles prepared by drop-casting catalyst inks on copper sample grids. These catalyst inks contain 0.5 wt.% Nafion and different water contents (0 vol.%, 25 vol.%, 50 vol.% and 75 vol.%).

5.3 Effect on activity of CO_2 electrolysis on carbon paper

As a basis for understanding the influence of Nafion at the surfaces of CuO particles on CO_2RR activity, we evaluated the electrochemically active surface areas (ECSAs) by measuring the double layer capacitances of drop-casted CLs on glassy carbon substrates in 0.1 M K_2SO_4 aqueous electrolyte (Figure 5.6a).[28] SEM images have revealed that CLs formed without Nafion contained many large agglomerates, while the addition of Nafion and its increasing weight ratio in the catalyst ink significantly improved the homogeneity and dispersity of CuO nanoparticles (Figure 5.1). Accordingly, compared to layers prepared in the absence of Nafion, the measured double layer capacitances increased and peaked at the lowest Nafion weight fraction of 0.005 wt.%.

These findings indicate that suitably low Nafion content can be beneficial for creating higher loadings of active sites by improving the dispersion of catalyst nanoparticles. However, the peaked dependence suggests that higher Nafion content results in the blocking of active sites due to formation of thick films over the nanoparticle surfaces. For layers prepared with 50 vol.% H_2O, large double layer capacitances were preserved over a broader range of Nafion wt.% (up to ~0.05 wt.%) and these values were also larger for all Nafion contents compared to those prepared with 0 vol.% H_2O, which is consistent with the observed reduction of Nafion thicknesses with increasing water content. Importantly, it is likely that thinner Nafion films contribute to the exposure of more active sites.
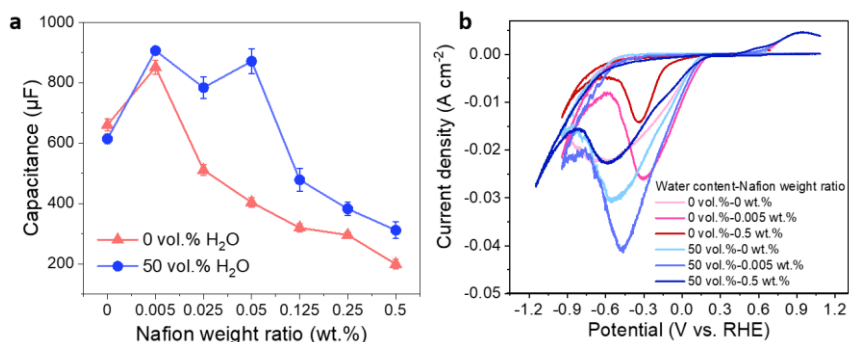

Figure 5.6 (**a**) Electric double layer capacitance of CLs deposited on glassy carbon as a function of Nafion weight ratio and solvent composition, measured in Ar-purged 0.1 M K_2SO_4 aqueous electrolyte. (**b**) The first cycle of cyclic voltammetry curves in CO_2-saturated 0.5 M $KHCO_3$ on carbon paper-based electrodes prepared using different ink formulations. Please note that the potential values in this figure are reported without iR compensation.

Before CO_2 electrolysis, all working electrodes were activated by cyclic voltammetry (CV) scanning. In this process, pre-catalytic CuO nanoparticles were reduced into catalytically active metallic Cu. Particularly, in the first CV cycle a broad peak around -0.45 V vs. RHE was recorded on all electrodes, which corresponds to the reduction reaction of CuO to Cu (Figure 5.6b). The integration of the reduction peak area represents the amount of charge driving the reduction reaction, and may be loosely associated with the amount of produced active sites.

Apparently, electrodes prepared with high-water-content and/or low-Nafion-content ink formulations displayed larger reduction peaks, indicating the greater extent of reduction and implying the existence of more active sites. This finding is in line with the result from electrochemical double layer capacitance data as mentioned above.

Briefly, increasing Nafion content leads to thicker Nafion films that can block active sites of CLs and decrease catalytic surface areas, which can be balanced by increasing the water content (i.e., decreasing alcohol content) to improve the inner structure of Nafion films. Furthermore, when subject to CO_2 electrolysis, Nafion films possessing different thicknesses and inner network connectivities are likely to significantly impact the reaction microenvironment and, thus, reaction selectivities. Therefore, it is expected that the incorporation of Nafion can promote the activity of CLs for electrochemical CO_2RR, but that an optimum catalyst ink formulation exists to balance these competing properties.

The impact of Nafion/solvent formulations on electrochemical CO_2RR was investigated using electrodes based on carbon paper substrates in a conventional H-cell under 0.5 M $KHCO_3$ with continuous CO_2 bubbling and a constant catalyst mass loading of 0.5 mg cm^{-2}. The activity in terms of current density and gas products of CO_2 electrolysis, including H_2, CO, CH_4, and C_2H_4, were analyzed at seven different potentials (Figure 5.7, Figure 5.8, and merged plots in Appendix Figure B1, Figure B2 and Figure B3)

Figure 5.7 Effect of Nafion/solvent formulations on potential-dependent CO_2 electrolysis. Catalytic performance of electrodes prepared by different Nafion/solvent formulations evaluated in terms of Faradaic efficiency of (**a**) H_2 (**b**) CO, (**c**) CH_4, and (**d**) C_2H_4.

Importantly, electrodes prepared without Nafion exhibited the lowest total current densities (Figure 5.8a), which is consistent with agglomeration and restructuring of weakly bound catalytic particles. Although the current density vs. potential (J-E) characteristics from all electrodes prepared with Nafion were similar, those prepared with 50 vol.% H_2O content displayed slightly higher total current densities across the entire potential range compared to those prepared without water. This result agrees with the reduced Nafion thickness, improved inner network connectivity, and higher ESCA for these CLs. Nevertheless, the weak dependence

of the total current density (TCD) on catalyst ink formulation implies that ionic transport limitations do not play a dominant role for the Nafion thickness regime investigated here, which is consistent with the findings of Kim *et al.*[12]
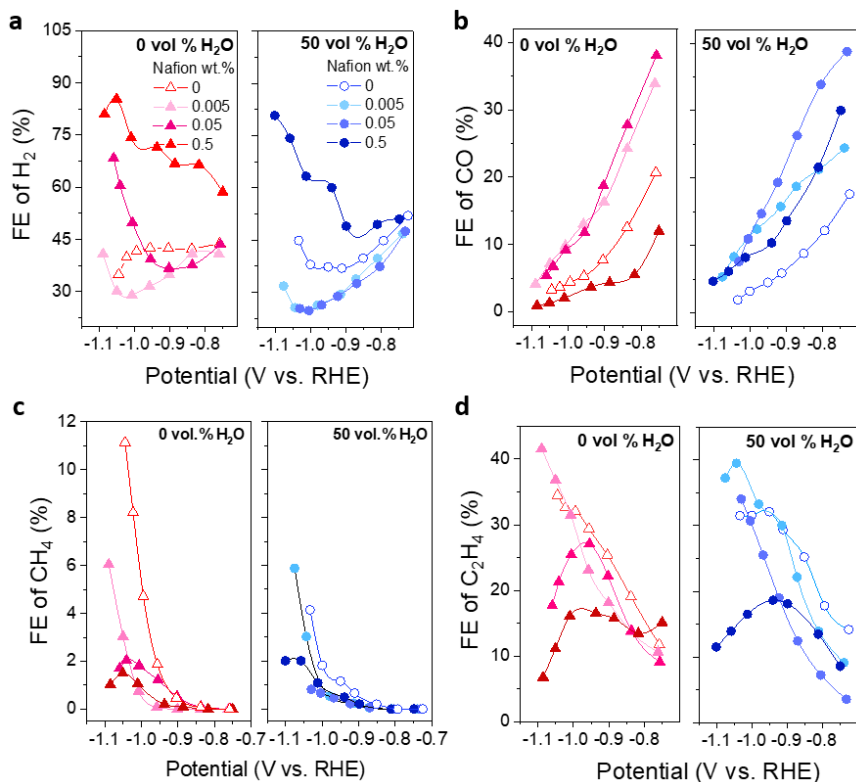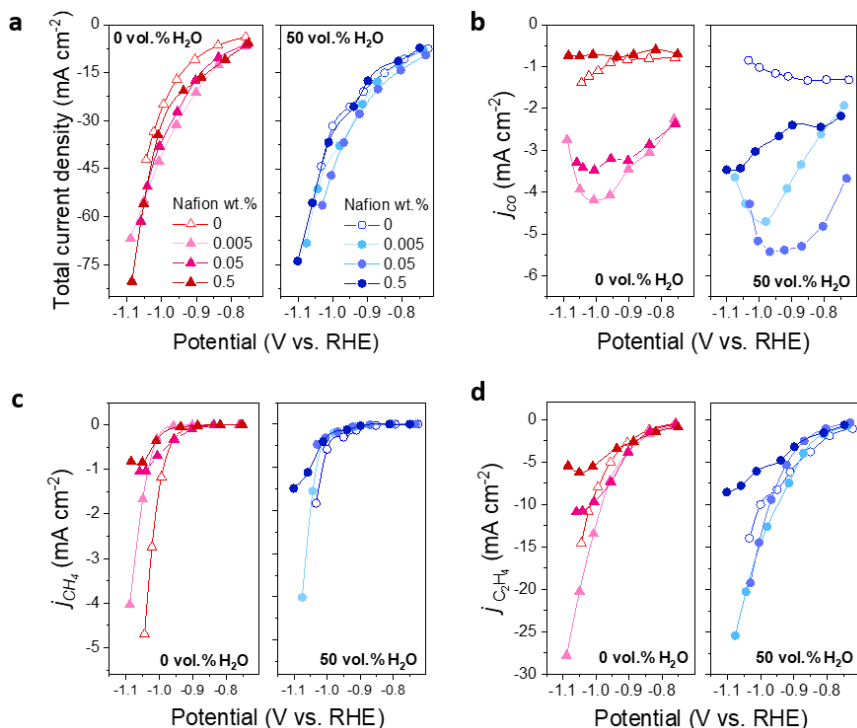

Figure 5.8 Effect of Nafion/solvent formulations on potential-dependent CO_2 electrolysis. Catalytic performance of electrodes prepared by different Nafion/solvent formulations evaluated in terms of the total current density (**a**) and partial current density of CO (**b**), CH_4 (**c**) and C_2H_4 (**d**).

Corresponding gas chromatography (GC) measurements reveal the strong influence of the catalyst ink formulation on the product yield. In particular, we observe significant suppression of HER with the inclusion of low Nafion weight fractions. For ink formulations containing 50 vol.% H_2O, similar HER suppression is obtained with both 0.005 and 0.05 wt.% Nafion, with an absolute minimum H_2 FE of 24.5% at -1.00 V vs. RHE for the electrode produced from 50 vol.% H_2O and

0.05 wt.% Nafion (Figure 5.7a). For those electrodes produced in the absence of water, the H_2 FE is consistently larger and rapidly increases with increasing Nafion content. At the highest Nafion content of 0.5 wt.%, vigorous hydrogen generation with maximum H_2 FEs in excess of 80%, were observed, though the H_2 FEs remained lower across the entire potential range for the 50 vol.% H_2O compared to the 0 vol.% H_2O samples. In addition, the production of CO was promoted and the yield of CH_4 was slightly reduced for all Nafion contents at 50 vol.% H_2O relative to those at 0 vol.% (Figure 5.7, Figure 5.8). As a result, the production of C_2H_4 was enhanced at 50 vol.% H_2O, especially in the region of low Nafion weight ratio where HER was significantly suppressed. The maximum C_2H_4 FE values of >40% were achieved at 0.005 wt.% regardless of initial water content, while the one prepared from the ink of 50 vol.% H_2O demonstrated superior C_2H_4 FEs across the whole potential range compared to the one prepared from the ink without water (Figure 5.7d).

Such performance is comparable with that measured on previously reported oxide-derived Cu catalysts.[9] The C_2H_4 FEs were generally reduced with increasing Nafion content, with those prepared with 0.5 wt.% Nafion remaining below 20% at all potentials. Accordingly, the partial current density of C_2H_4 decreased by a factor of approximately 3.6× near -1.1 V vs. RHE, from -27 mA cm^{-2} at 0.005 wt.% Nafion to less than -8 mA cm^{-2} at 0.5 wt.% Nafion for both water contents (Figure 5.8). Here, it is important to note that electrodes prepared without Nafion exhibited reasonably large C_2H_4 FEs in excess of 30%. However, these electrodes were characterized by poor stabilities compared to those containing Nafion, as discussed below.

5.4 Effect on selectivity of CO_2 electrolysis on carbon paper

As demonstrated above, the maximum activity for C_2H_4 production together with minimum activity for HER in terms of FE was achieved around the potential of -1.0 V vs. RHE and the current density of approximately -50 mA cm^{-2}. Given C_2H_4 is one of the major target multicarbon products, we further investigated the effect of Nafion/solvent formulations on the selectivity of CO_2 electrolysis, particularly the

selectivity of multicarbon products, by carrying out chronopotentiometry tests at a constant current density of -50 mA cm^{-2} on all electrodes. Such chronopotentiometric CO_2 electrolysis was evaluated over the course of 5 h with all testing conditions being the same as those used for chronoamperometric CO_2 electrolysis, as introduced above in Subsection 5.2. Gaseous products were analyzed every 20 min over 5 h and liquid products in catholytes were quantified after the whole period of electrolysis. For the clarity of data, we determined the average FE of each specific product within 5 h and plotted the product distribution of each electrode in Figure 5.9.

In total, 17 different products of CO_2RR were detected using GC and nuclear magnetic resonance spectroscopy (^{1}H NMR), in agreement with previous studies,[4] but only the 8 major products (hydrogen, carbon monoxide, methane, ethylene, formate, acetate, n-propanol, and ethanol) were quantified (see the Appendix Figure B4, Figure B5 and Table B1). The product distribution as a function of Nafion weight ratio and solvent composition in the ink formulation, plotted in Figure 5.9, confirmed the strong dependence of product distribution on both Nafion content and solvent composition. Here, it is noted that the observed FEs are not identical to those reported near 50 mA cm^{-2} in Figure 5.7 since certain formulations yielded unstable performance during the long-term evaluation. In general, the consequence of these instabilities was to increase HER at the cost of CO_2RR activity (see below).
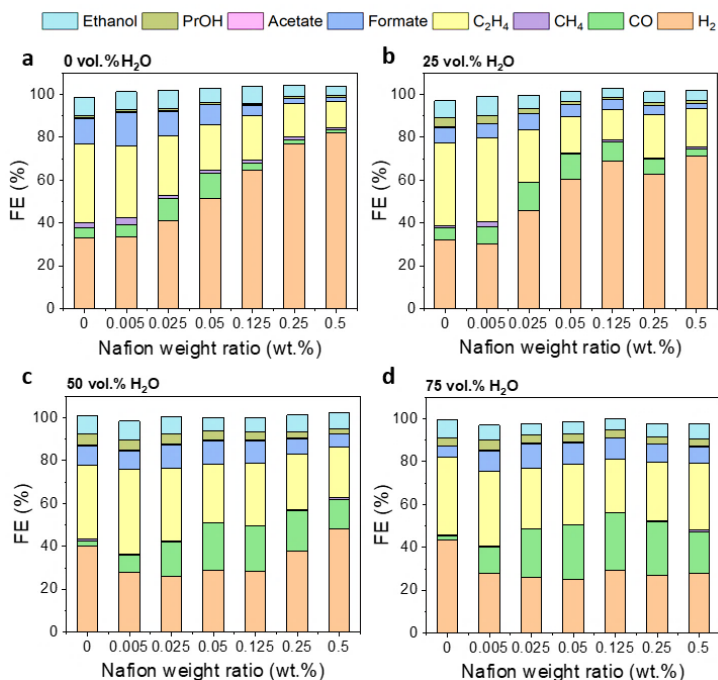
Figure 5.9 Product distributions on CLs during chronopotentiometric CO_2 electrolysis at a total current density of -50.0 mA cm^{-2} in CO_2 saturated 0.5 M $KHCO_3$. The electrodes were prepared with various Nafion/solvent formulations containing seven different Nafion weight ratios (0, 0.005, 0.025, 0.05, 0.125, 0.25, and 0.5 wt.%) and four different water contents, namely 0 (**a**), 25 (**b**), 50 (**c**) and 75 (**d**) vol.%.

For all electrodes, the major products comprised C_2H_4, CO, and H_2. To specifically analyze the selectivity changes, we mainly focus on the average FEs of 4 dominant products at different Nafion/solvent formulations, namely H_2, CO, $HCOO^-$, and C_2H_4, as compared in heatmaps (Figure 5.10, Figure 5.11 and Appendix Figure B6), along with heatmaps for the total FE for total CO_2 reduction products, single carbon products (C_1) and C_{2+} products. Corresponding heatmaps for minor products are available in Appendix Figure B6.
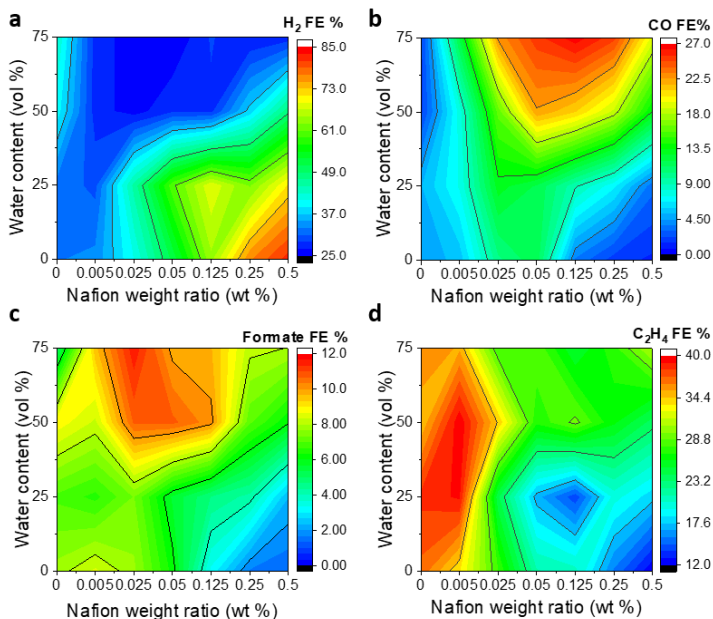
Figure 5.10 Effect of Nafion/solvent formulations on selectivity of chronopotentiometric CO_2 electrolysis at -50.0 mA cm^{-2} in CO_2 saturated 0.5 M $KHCO_3$. Heatmaps of Faradaic efficiency of four major CO_2 reduction products: (**a**) H_2 (**b**) CO (**c**) formate (HCOO$^-$) and (**d**) C_2H_4.

From these data, several distinct regions can be identified. First, HER is effectively suppressed over an extended region spanning low-Nafion and/or high-water content, where the H_2 FEs were all below 30% (top left of heatmap in Figure 5.10a). Notably, the H_2 FEs at each Nafion weight ratio, and especially at high Nafion weight ratios (>0.05 wt.%), were continuously reduced with gradual increase of water content in ink formulations. For instance, for electrodes prepared with 0.5 wt. % Nafion, the H_2 FE was drastically reduced from 80% at 0 vol.% H_2O to 28% at 75 vol.%. Consistent with results discussed above, more vigorous H_2 production was associated with CLs prepared with high Nafion and low water content (bottom right of heatmap of Figure 5.10a). Within the region of suppressed HER, C_{2+} products were dominant for all CLs prepared with low Nafion content, regardless of water fraction. While C_2H_4 was the primary product, FEs for both EtOH and n-

94

PrOH increased with increasing water content for CLs prepared with low Nafion content (Appendix Figure B6f, h). That is to say, CLs prepared at high water content and low Nafion content appear to enhance the adsorption of not only CO intermediate for C-C coupling but also key C_2 intermediates for subsequent C_1-C_2 coupling. Taken together, the dependence of these products on ink formulation resulted in a similar form of the heatmap for the total FE of C_{2+} products varying from a peak value of 54% at low Nafion content to a minimum of 17% for high Nafion and low water content (Figure 5.11c).

Figure 5.11 Effect of Nafion/solvent formulations on selectivity of chronopotentiometric CO_2 electrolysis at -50.0 mA cm^{-2} in CO_2 saturated 0.5 M KHCO$_3$. Heatmaps of Faradaic efficiency of all CO_2 reduction products (**a**), total single carbon (C_1) products (**b**), multicarbon (C_{2+}) products (**c**), and the ratio of C_{2+} to C_1 products (C_{2+}/C_1 ratio, (**d**)).

Interestingly, the production of CO was drastically affected by Nafion/solvent formulations with CO FE ranging from 0 to ~27.0%. In particular, CO production was especially favored for formulations possessing both high water and high Nafion

content (Figure 5.11b). In addition, the FE of another major C_1 product, namely formate, increased in the CO-favored region (Figure 5.11b), though its peak FE occurred at slightly lower Nafion content. At high water content, this direct competition between C_1 and C_{2+} products suggests enhanced activity for C_{2+} products at low Nafion content that is disturbed at higher Nafion content, which is also confirmed in the heatmap of the C_{2+}/C_1 ratio in Figure 5.11d. The underlying reasons for these changing product distributions will be addressed in detail in section 5.6 and 5.7 below.

5.5 Effect on stability of CO_2 electrolysis on carbon paper

The effect of Nafion/solvent formulations on the stability of Cu-catalyzed CO_2 electrolysis on carbon paper substrates was measured from two primary perspectives: the dynamic change of selectivity and the structural evolution of CLs in continuous electrolysis.

To probe the dynamic change of electrochemical performance over the course of 5 h of chronopotentiometric CO_2 electrolysis at -50 mA cm^{-2}, the FEs of all gaseous products were monitored by online GC with sampling every 20 min (Figure 5.12. Figure 5.13, Appendix Figure B2 and Figure B3), and the corresponding working potentials were recorded over time as well (Figure 5.14).

The dynamic FE of each product was measured via GC and is plotted as a function of time, classified into four groups according to four water contents (0 vol.% H_2O in Figure 5.12, 50 vol.% H_2O in Figure 5.13, 25 vol.% H_2O in Appendix Figure B2 and 75 vol.% H_2O in Appendix Figure B3). In general, for all electrodes the selectivity for gaseous CO_2 reduction products continuously decreased throughout the 5 h long experiments, indicating the degradation of electrochemical performance regardless of Nafion/solvent formulations.
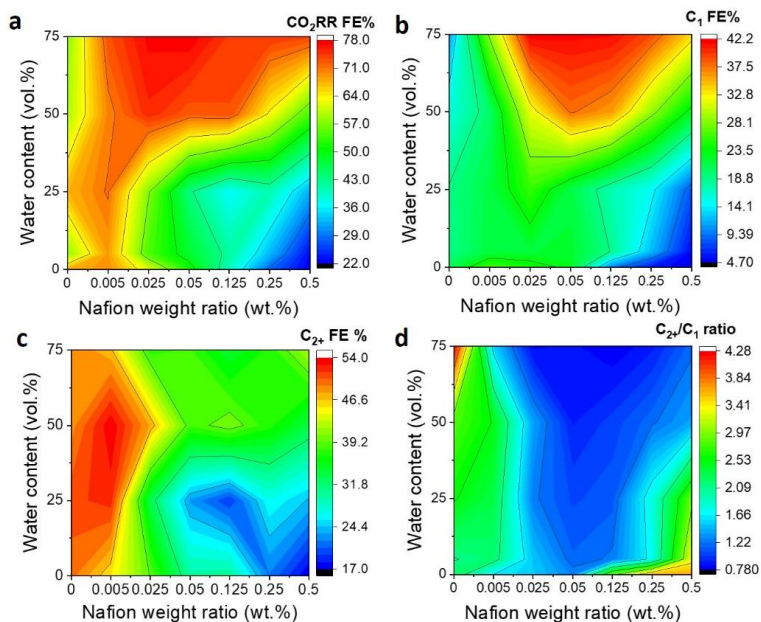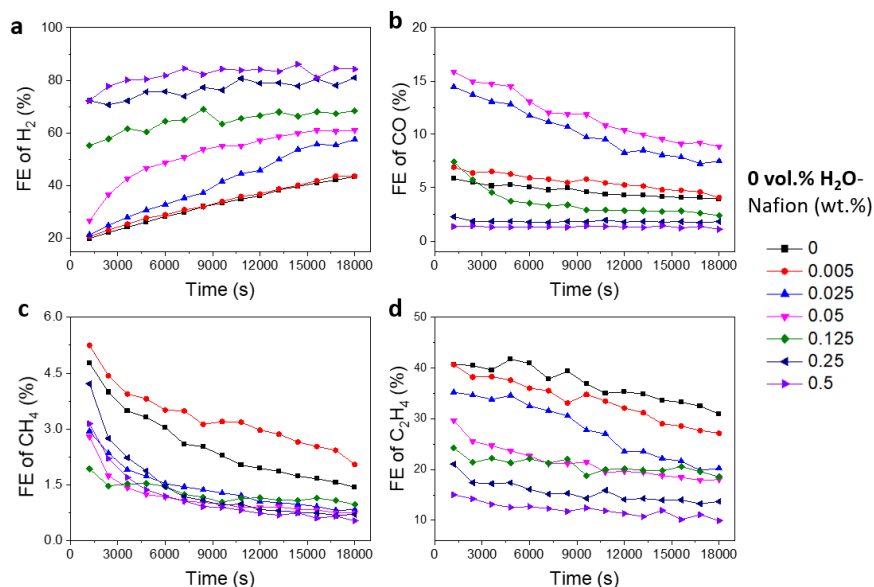
Figure 5.12 Effect of Nafion/solvent formulations on stability of chronopotentiometric CO_2 electrolysis at -50.0 mA cm^{-2} in CO_2 saturated 0.5 M KHCO$_3$. Dynamic changes of FEs of gaseous products: namely H_2 (**a**), CO (**b**), CH$_4$ (**c**), and C_2H_4 (**d**), over 5 h.

As compared between Figure 5.12 and Figure 5.13, regardless of water content, the electrodes without Nafion presented the worst stability with the largest change of FEs across 5 h. Specifically, the production of H_2 was constantly increased at the cost of a continuous decrease of production of CO_2 reduction products, particularly C_2H_4. Such rapid degradation of CO_2 reduction activity is likely caused by the detachment of CLs from carbon paper substrate in the absence of Nafion binder, which was further investigated using SEM in Figure 5.15 and Figure 5.16. After adding Nafion, the net drop (or rise) of FE of each gas CO_2 reduction product (or H_2) became smaller with increasing Nafion content, indicating enhanced stability of CO_2 electrolysis due to more stable CLs produced from inks possessing higher Nafion content.
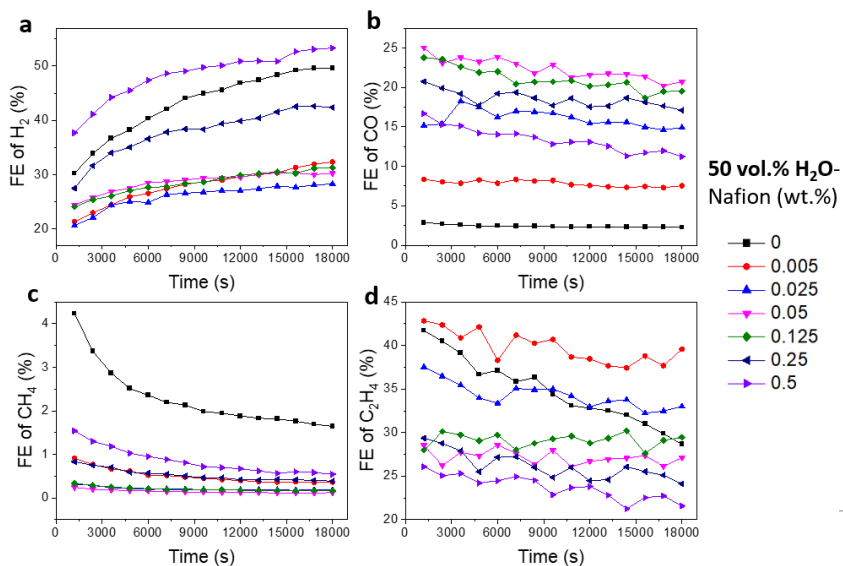
Figure 5.13 Effect of Nafion/solvent formulations on stability of chronopotentiometric CO_2 electrolysis at -50.0 mA cm^{-2} in CO_2 saturated 0.5 M $KHCO_3$. Dynamic changes of FEs of gaseous products: namely H_2 (**a**), CO (**b**), CH_4 (**c**), and C_2H_4 (**d**), over 5 h.

On the other hand, the the decrease of the FEs to CO_2 reduction products was found to be slower on electrodes prepared from inks with 50 vol.% H_2O compared to those prepared from inks with 0 vol.% H_2O. Moreover, the overall CO_2 reduction activity was enhanced for 50 vol. % H_2O compared to that of 0 vol. % H_2O, especially at high Nafion content. For instance, the severe HER at 0.5 wt.% Nafion and 0 vol.% H_2O with the maximum H_2 FE of >80% was significantly reduced for 0.5 wt.% Nafion and 50 vol.% H_2O, with the maximum H_2 FE of ~50%. Moreover, with increasing water content, the production of CO was enhanced at all Nafion contents, and a similar trend was also observed for C_2H_4 production. These findings imply that ink formulations with high water content are conducive to stable and enhanced production of multicarbon products (i.e., C_2H_4). Given previously introduced results of the effect of Nafion/solvent formulations on Nafion films and CLs in Chapter 4, we infer that the compact structure and better inner network

connectivity of Nafion films obtained with high water content formulations enable stable CLs and favorable local microenvironments, which eventually ensures superior stability of CO_2 electrolysis.

Moreover, the recorded cathodic potentials in chronopotentiometric tests were continuously positively shifted over 5 h for all electrodes (Figure 5.14). This is most likely because the H_2 FE is increasing. This corresponds to the degradation mechanisms that begins to favor HER. In this scenario, the overpotential for HER is decreasing, leading to an increased partial current density to H_2, which at last reduces the overall potential required to sustain -50 mA cm^{-2}.
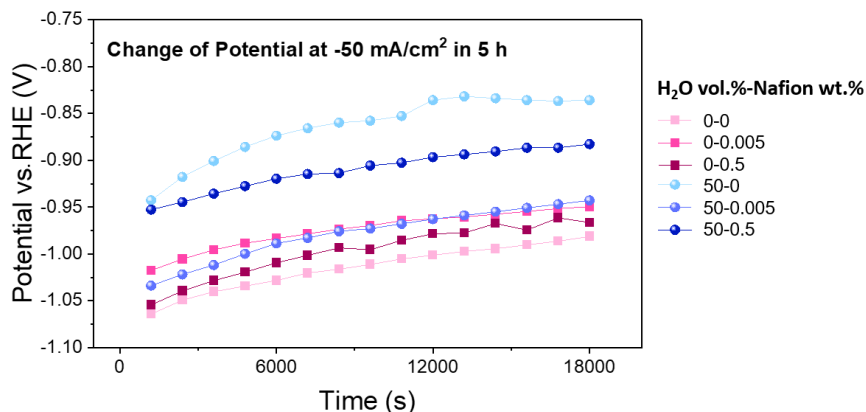
Figure 5.14 Effect of Nafion/solvent formulations on selectivity of chronopotentiometric CO_2 electrolysis at -50.0 mA cm^{-2} in CO_2 saturated 0.5 M $KHCO_3$. Changes of cathodic potentials during 5 h of electrolysis for electrodes prepared with varied Nafion/solvent formulations.

To understand the underlying mechanisms of the observed reactivity changes during sustained electrolysis, we monitored the structural evolution of Cu catalysts with the help of *ex situ* SEM measurements. First, six representative carbon paper-based electrodes, including those prepared with 0 and 50 vol.% H_2O combined with 0, 0.005, and 0.5 wt.% Nafion, were characterized before and after 5 h chronopotentiometry tests at a fixed TCD of -50 mA cm^{-2}. Direct comparison of selected CLs before and after operation is provided in Figures 5.15 and Figure 5.16.
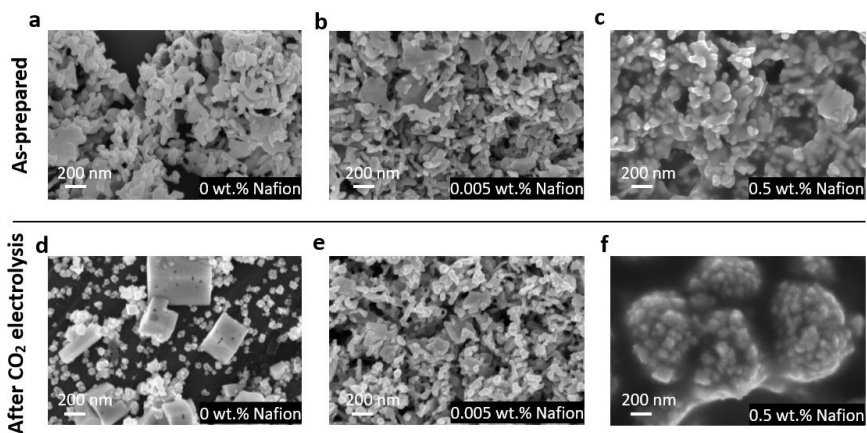
Figure 5.15 SEM images of catalyst layers prepared with formulations of 0 vol.% H_2O and different Nafion contents before (**a-c**) and after (**d-f**) CO_2 electrolysis of 5 h at -50 mA cm^{-2}.

Figure 5.16 SEM images of catalyst layers prepared with formulations of 50 vol.% H_2O and different Nafion contents before (**a-c**) and after (**d-f**) CO_2 electrolysis of 5 h at -50 mA cm^{-2}.
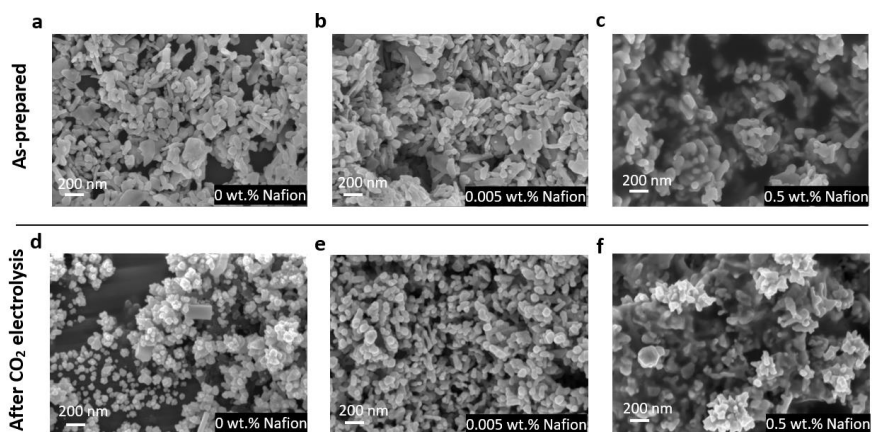
Notably, large cubic Cu crystals with size of 250-600 nm were observed on the electrode without Nafion, which suggested that significant Cu reconstruction occurred during CO_2 electrolysis. Such reconstruction would not only reduce the

electrochemically active surface area, but can also cause a change of selectivity due to variation of crystal facets between the *in situ* grown Cu cubes and pristine CuO-derived Cu nanoparticles.[23,24] Moreover, a decrease of surface coverage of Cu and exposure of the bare carbon paper substrate indicated possible detachment of Cu nanoparticles. Such morphological instabilities are consistent with prior investigations of Cu-based CO_2R electrocatalysts, which are susceptible to aggregation, delamination, dissolution-redeposition, and facet evolutions under reaction conditions.[4,135] These severe morphological changes likely account for increasing H_2 FE from 30% to 50% during the 5 h chronoamperometric experiment (Figure 5.13a).

In contrast, the morphologies and coverages of CLs containing Nafion were effectively preserved, suggesting that the ionomer serves as an effective binder and encapsulant to enhance adhesion and confine particles, thereby reducing the surface mobility, detachment, and dissolution/redeposition processes that characterize bare Cu electrocatalysts. Therefore, Nafion ionomer was necessarily required to ensure the structural stability of Cu in CO_2 electrolysis. However, thicker Nafion films obtained from inks containing higher Nafion weight ratios (0.5 wt.%) lead to reduced electrochemically active surface areas, blocking of active sites, and enhanced HER.

5.6 Effect on local molar ratio of CO_2/H_2O

The complete set of observations presented above suggests a basis for understanding CL performance characteristics in terms of the evaluated properties of Nafion as a function of ink composition. As a starting point, we first studied the role of Nafion in impeding CO_2 transport to the Cu surface by estimating the local concentration ratio of CO_2 to H_2O, denoted as $[CO_2]/[H_2O]$.

Analysis of the local molar ratio of CO_2 to H_2O at the catalyst surface, $[CO_2]/[H_2O]$, follows the previously reported approach by Kim *et al*.,[12] and is described in detail here for clarity and completeness. The analysis begins with a determination of whether the system is in a kinetic or mass transport limited regime on the basis of

the experimentally measured electrocatalytic current density for CO_2 reduction products. For the case that the system is under kinetic control, the local carbon dioxide concentration can be assumed to be approximately equal to its solubility in the Nafion ionomer. To test whether this assumption holds, we first evaluate the mass transport regime, as described below.

For a given total applied current density in CO_2 electrolysis, j_{tot} (-50 mA cm^{-2} on carbon paper-based electrodes), the mass flux of CO_2 consumed on the bare Cu surface due to kinetics, $J_{co_2,kin}$, can be calculated according to the following expression:

$$J = \frac{j_{tot}}{F} \sum_i^m \frac{FE_{co_2R,i} \, N_i}{n_i} \qquad 5.1$$

where $FE_{co_2R,i}$ is the faradaic efficiency of each major CO_2 reduction product, N_i is the number of carbon atoms associated with each of these products, n_i is number of electrons required to generate each of these CO_2RR product molecules, and F is the Faraday constant of 96,485 C mol^{-1}. The summation is performed over all m detected products of CO_2 reduction. As shown in Table 5.1, the calculated values for the kinetic mass flux associated with consumption of CO_2 at the catalyst surface lie in the range of 2×10^{-5} to 1×10^{-4} mol m^{-2} s^{-1}. To determine whether the steady state system is governed by mass transport or reaction kinetic control, these fluxes are compared to the limiting mass flux given by diffusive transport of CO_2 from the bulk to the catalyst surface, as described below, first for the case of bare Cu and then for Nafion-coated Cu.

According to Fick's Law, the diffusive mass transfer flux of CO_2 ($J_{co_2,MT}$) across the boundary layer is given by

$$J_{co_2,MT} = -D_{CO_2,w} \frac{dc_{CO_2}(x)}{dx} \qquad 5.2$$

where $D_{CO_2,w}$ is the diffusivity of CO_2 in aqueous solution (2.02×10^{-9} m^2 s^{-1} at 298 K),[136] and $c_{CO_2}(x)$ is the one dimensional concentration profile of CO_2. The minimum diffusive mass flux under mass transport limited conditions ($J_{co_2,MT,min}$)

will correspond to the case in which there is a linear concentration profile between the Cu surface ($x = 0$) and the outer edge of the boundary layer ($x = \delta$), yielding:

$$J_{co_2,MT,min} = -D_{CO_2,w}\frac{c_{CO_2}(\delta)-c_{CO_2}(0)}{\delta} \qquad 5.3$$

where $c_{CO_2}(\delta)$ is the concentration of CO_2 in the bulk electrolyte of 34 mM and δ is the hydrodynamic boundary layer thickness (~100 μm).[137] Under mass transport limited conditions, the concentration at the electrode surface would approach 0 mM ($c_{CO_2}(0) = 0$), thus yielding a minimum diffusive CO_2 flux of 6.87×10^{-4} mol m^{-2} s^{-1} under mass transport limited conditions. Although this value was calculated for the case of bare Cu surface, the fact that the value is much larger than the kinetic mass flux associated with CO_2 consumption suggests that the system is under kinetic rather than mass transport limited control. However, introduction of Nafion to the surface could introduce an additional impediment to mass transport, so we next evaluate this case.

Introduction of Nafion ionomer onto the Cu surface, does not alter the expression for the kinetic CO_2 mass flux given by Eq. 5.1. However, the presence of Nafion modifies the diffusivity of CO_2 in the local vicinity of the Cu surface, and can thus change the minimum flux of CO_2 under transport limited conditions. Application of a mass balance at the ionomer/electrolyte boundary and assuming linear concentration profiles as above yields:

$$J_{co_2,MT,min} = -D_{CO_2,w}\frac{c_{CO_2}(\delta)-c_{CO_2}(d)}{\delta} = -D_{CO_2,Naf}\frac{c_{CO_2}(d)-c_{CO_2}(0)}{d} \qquad 5.4$$

where $D_{CO_2,w}$ is the diffusivity of CO_2 in aqueous solution (2.02×10^{-9} m^2 s^{-1}),[136] $D_{CO_2,Naf}$ is the diffusivity of CO_2 in Nafion (2.4×10^{-10} m^2 s^{-1}),[138] δ is the hydrodynamic boundary layer thickness in the liquid phase (~100 μm),[137] and d is the thickness of hydrated Nafion measured by spectroscopic ellipsometry under 100% relative humidity. As before, under mass transport limited conditions, $c_{CO_2}(0) \to 0$, while $c_{CO_2}(\delta)$ is the bulk concentration of CO_2 of 34 mM and $c_{CO_2}(d)$ is the concentration at the Nafion/electrolyte interface. Thus, the transport limited CO_2 flux to the surface of Nafion-coated Cu is given by:

$$J_{CO_2,MT,min} = \frac{D_{CO_2,w}\, c_{CO_2}(\delta)}{\delta + d\left(\frac{D_{CO_2,w}}{D_{CO_2,Naf}}\right)}. \qquad\qquad 5.5$$

As shown in Figure 4.6b, for the range of thicknesses determined by spectroscopic ellipsometry in this work, the minimum transport limited CO_2 flux is not significantly decreased by the presence of Nafion, with all values being larger than 6.86×10^{-4} mol m^{-2} s^{-1} (compared to 6.87×10^{-4} mol m^{-2} s^{-1} for the case of bare Cu, as determined by Eq. 5.3). Importantly, the mass transport limited flux is significantly larger than the kinetic flux associated with CO_2 consumption during CO_2 electrolysis. Thus, it is highly unlikely that the system experiences CO_2 mass transport limitations, in agreement with the findings of Kim *et al.*[12]

For the case of kinetically controlled reaction conditions, which holds for the present work, the concentration of CO_2 within the Nafion can be assumed to be approximately equal to its solubility, which is 36.1 mM.[12] Although this assumes that the CO_2 solubility is independent of the internal structure of the Nafion layers derived from different solvents, it is important to note that the CO_2 solubility in Nafion is very similar to that in the bulk electrolyte. Thus, changing degrees of water uptake should not have a significant influence on the CO_2 solubility.

Finally, the local molar ratio of CO_2 to H_2O, [CO_2]/[H_2O] under kinetic reaction is calculated by dividing the saturation concentration of CO_2 in Nafion, $c_{CO_2,sat,Naf} = 36.1$ mM, by the concentration of water determined via *in situ* spectroscopic ellipsometry, c_{H_2O} (Table 4.3):

$$\frac{[CO_2]}{[H_2O]} = \frac{c_{CO_2,sat,Naf}}{c_{H_2O}}. \qquad\qquad 5.6$$

The resulting values are provided in Table 5.1, as well as Figure 5.17.

Table. 5.1 Calculated molar concentration of CO_2 in CO_2 electrolysis in terms of kinetically consumed CO_2 molecules ($J_{CO_2,\,kin}$) to form CO_2 reduction products, minimum diffusive CO_2 flux under mass transport control ($J_{CO_2,\,MT,min}$), and the resulting molar concentration ratio of CO_2 to H_2O at the catalyst surface, [CO_2]/[H_2O].

Water content in the formulation (vol.%)	Kinetically consumed CO_2 molecules ($J_{co_2, kin}$) (mol m^{-2} s^{-1})	Mass transport flux of CO_2 ($J_{co_2, MT, min}$) (mol m^{-2} s^{-1})	Molar ratio of CO_2/H_2O
0	2.44×10^{-5}	6.86×10^{-4}	115
25	3.61×10^{-5}	6.86×10^{-4}	139
50	7.99×10^{-5}	6.86×10^{-4}	219
75	1.07×10^{-5}	6.87×10^{-4}	396

Thus, for the range of Nafion thicknesses investigated here, the system is governed by surface reaction rate kinetics rather than mass transport of CO_2. While this conclusion may be surprising in light of the strong dependence of CO_2R selectivity and product distribution on the catalyst ink formulation, it is important to recognize that the internal structure and network connectivity of Nafion films are significantly impacted by the solvent composition, as described above. In particular, improved internal network connectivity, which is promoted by high water/alcohol fractions within the solvent, is expected to reduce water uptake within the formed Nafion layers, which could significantly modify the relative availability and accumulation of reactants and intermediates at Cu catalyst surfaces.

To test this hypothesis and understand the impact of different ink formulations on the reaction microenvironment, we have estimated the local molar concentration ratio of CO_2 and H_2O ([CO_2]/[H_2O]) on the basis of measured water concentration in Nafion films using *in situ* ellipsometry and corresponding CO_2R partial current densities in chronopotentiometry tests (Figure 5.17b).

For a fixed Nafion weight fraction of 0.5 wt.%, increasing water content in the solvent solution resulted in smaller swelling fractions of Nafion films during subsequent exposure to humidified environments (Table 4.3). This finding is consistent with the scheme in Figure 4.2 and indicates decreasing water uptake (i.e., decreasing concentration of water molecules compared to the concentration of Nafion SO_3^-) when treated with water-saturated N_2 (Figure 5.17a).
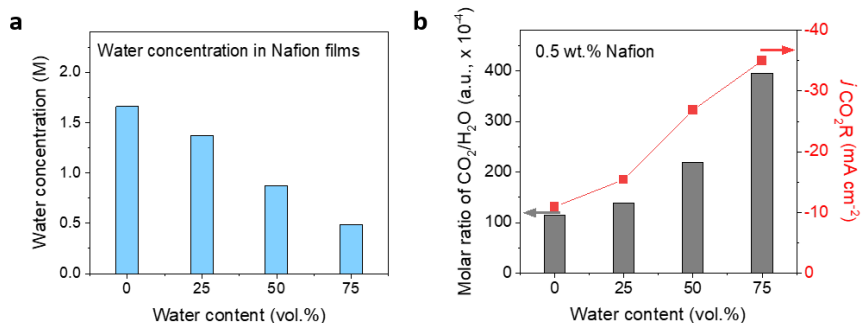
Figure 5.17 Effect of solvent composition on water uptake and reaction microenvironment during CO_2 electrolysis. (**a**) Plots of calculated water concentration in Nafion films from *in situ* ellipsometry tests versus water content in Nafion solutions. (**b)** Estimation of molar ratio of CO_2/H_2O (grey bars) on the basis of measured water concentration within Nafion films in (**a)** and corresponding partial current densities for CO_2R (red squares) in chronopotentiometry test of -50 mA cm^{-2}.

Combined with the partial current densities for all CO_2R products during 5 h of chronopotentiometry electrolysis, this water concentration reveals a substantial increase of the calculated molar ratio [CO_2]/[H_2O] with increasing water content in the original solvent. In particular, when operated at a TCD of -50 mA cm^{-2} the molar ratio [CO_2]/[H_2O] increased by 3.4× for the films prepared with 75 vol.% H_2O compared to those prepared with 0 vol.% H_2O. This important change to the reaction microenvironment corresponds to an enhanced CO_2R activity, with partial current density j_{CO2R} increasing from -10.9 mA cm^{-2} at 0 vol.% to -35.0 mA cm^{-2} at 75 vol.% (Figure 5.17b). Together with our insights from structural analysis of Nafion films in Chapter 4, we can thus conclude that this dramatically higher molar ratio [CO_2]/[H_2O] arises from the formation of thinner and denser Nafion films with better inner network connectivity, resulting in enhanced CO_2 availability near the copper surface for ink formulations comprising higher water content. This finding is also consistent with the observed product distribution, which favors CO_2RR over HER. In addition, the decreased water concentration in the reaction environment could have a significant impact on the local pH. While this quantity is extremely

difficult to quantify, it is important to recognize that one OH^- ion is generated for each e^- consumed by CO_2R.[38] Thus, suppressed water uptake in Nafion films could promote more alkaline environments that favor C-C coupling reactions.

5.7 *In situ* Raman spectroscopy

To gain insight into the local microenvironments near the Cu catalyst surfaces, we monitored the oxidation state of Cu (Cu_2O and/or CuO) and the presence of various adsorbed intermediates and ions on six different electrodes during electrochemical CO_2RR measurements using *in situ* Raman spectroscopy (Figure 5.18 and Figure 5.19).

As a basis for these experiments, we first analyzed the catalyst activation process by cyclic voltammetry (CV) in the pre-catalytic region between the open circuit potential (OCP) and -0.9 V vs. RHE, during which the first CV sweep always showed a distinct reduction wave for conversion of CuO to metallic Cu (Figure 5.6b). Accordingly, on all six samples we observed the characteristic peak for CuO at ~295 cm^{-1} at OCP, which disappeared when the applied potential was more cathodic than -0.15 V vs. RHE, suggesting that CuO can be readily reduced to catalytically active Cu.
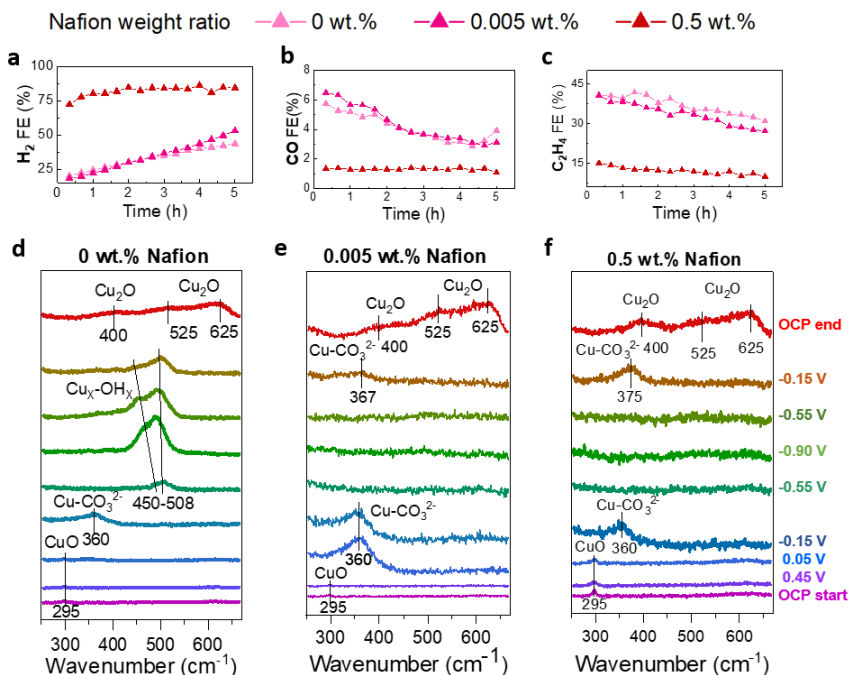
Figure 5.18 Effect of Nafion weight ratio on local reaction environments during CO_2 electrolysis in CO_2 saturated 0.5 M $KHCO_3$ on three carbon paper-based electrodes: 0 vol.% H_2O-0 wt.% Nafion, 0 vol.% H_2O-0.005 wt.% Nafion and 0 vol.% H_2O-0.5 wt.% Nafion. Changes of Faradaic efficiencies of H_2 (**a**), CO (**b**), C_2H_4 (**c**) within 5 h of CO_2 electrolysis on 3 electrodes. *In situ* Raman spectra recorded in cyclic voltammetry tests (**d-f**) on 3 electrodes.

In addition, a broad band at ~360 cm^{-1} emerges starting at 0.05 V vs. RHE and persists until -0.15 V vs. RHE. Recent reports have assigned this band to surface adsorbed bidentate carbonate species ($Cu-CO_3^{2-}$) associated with the CuO reduction process in the presence of $KHCO_3$ electrolyte and hydroxyl species.[139–142] It is important to note that this mode is similar in energy to the linear Cu-C stretch (from adsorbed *CO on Cu) that could be indicative of adsorbed *CO, a key intermediate in C_{2+} product formation. However, this can be excluded due to the absence of the spectral signature of Cu-CO rotational modes at 280 cm^{-1}, the corresponding broad linewidth of the 360 cm^{-1} vibrational feature, and its presence

in the pre-catalytic potential range associated with CuO to Cu activation. Thus, the 360 cm^{-1} mode observed between 0.05 and -0.15 V vs. RHE is assigned to bidentate Cu-CO$_3^{2-}$, and disappears upon complete activation of the catalyst to Cu, in line with recent *in situ* Raman spectroscopy investigations on the dynamics of CO$_2$ to CO activation in this potential regime.[142]
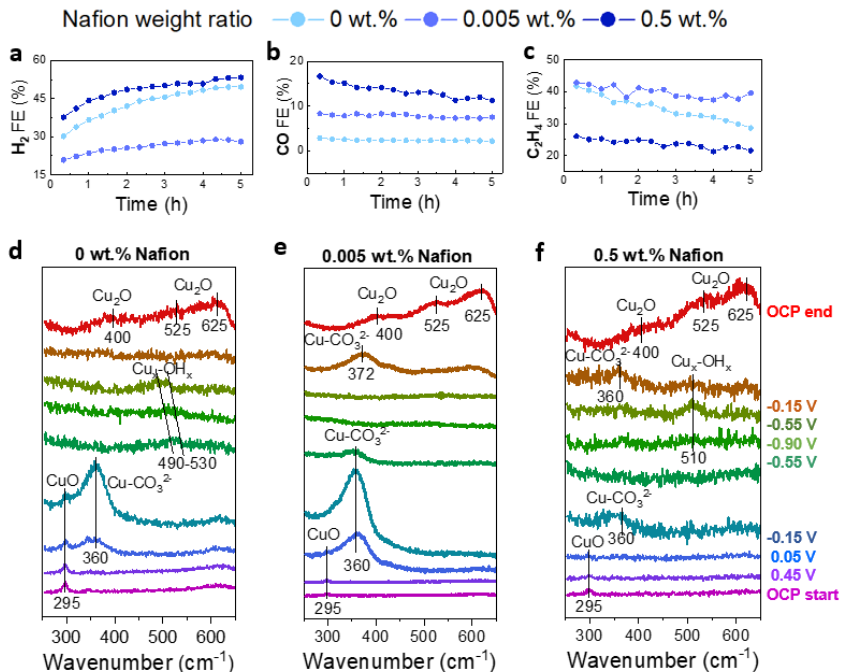
Figure 5.19 Effect of Nafion weight ratio on local reaction environments during CO$_2$ electrolysis in CO$_2$ saturated 0.5 M KHCO$_3$ on 3 carbon paper-based electrodes: 50 vol.% H$_2$O-0 wt.% Nafion, 50 vol.% H$_2$O -0.005 wt.% Nafion and 50 vol.% H$_2$O-0.5 wt.% Nafion. Changes of Faradaic efficiencies of H$_2$ (**a**), CO (**b**), C$_2$H$_4$ (**c**) within 5 h of CO$_2$ electrolysis on 3 electrodes. *In situ* Raman spectra recorded in cyclic voltammetry tests (**d-f**) on 3 electrodes.

When scanning to more cathodic potentials from -0.55 and -0.90 V vs. RHE and then scanning back to -0.15 V vs. RHE, multiple broad peaks in the range of ~490 to ~530 cm^{-1} arise, particularly on the electrodes fabricated without Nafion and with

0.5 wt.% Nafion (Figure 5.18d-f and Figure 5.19d-f).[140,143,144] These spectral features around 500 cm^{-1} have been heavily debated in literature: some works show evidence for the presence of hydroxide ions due to severe HER,[145] whereas others have used isotope labeling to show that bands in this regime correspond to carbon-containing reaction intermediates.[141,142] A definite assignment of the bands in this region remains challenging due to the low signal-to-noise ratio, but the presence of Cu_x-OH_y is inferred due to the likely consumption of protons during HER. As shown in Figure. 5.18a and Figure 5.19a, HER dominates for 0 wt% and 0.5 wt% Nafion, in line with the presence of vibrational features around 500 cm^{-1} (Figure 5.18d and Figure 5.19d).

For the case of electrodes prepared with 0.005 wt.% Nafion, peaks at approximately 500 cm^{-1} were extremely weak, in agreement with suppressed HER (Figure 5.18e and Figure 5.19e). In general, electrodes prepared with high Nafion content (0.5 wt.%) exhibited much weaker Cu-CO_3^{2-} and/or potential Cu_x-OH_y Raman scattering intensities than those prepared without Nafion or with low Nafion content (0.005 wt.%). This could be a consequence of the reduced ECSA and limited carbonate content near the surface during the Cu_2O-to-Cu reduction process in the case of thicker Nafion films at 0.5 wt.%. Finally, on all six electrodes, Cu at the surface was partially re-oxidized into Cu_2O when the CV concluded at OCP due to inevitable exposure of the electrode to the aqueous electrolyte, as indicated by three corresponding peaks at around 400, 525, and 625 cm^{-1} assigned to Cu_2O (Figure 5.18d-f and Figure 5.19d-f).[139,140]

Immediately after the activation process, we continued with chronoamperometry tests at a fixed potential of -1.0 V on all electrodes and simultaneously analyzed the local microenvironment by *in situ* Raman spectroscopy (Figure 5.21). Prior to the application of potential, all electrodes exhibited two peaks near 525 and 625 cm^{-1} at OCP, which are attributed to the re-oxidized Cu_2O described above (Figure 5.20). Upon application of -1.0 V vs. RHE and the associated onset of CO_2 electrolysis, Cu_2O was reduced to metallic Cu and the corresponding peaks for Cu_2O completely vanished.
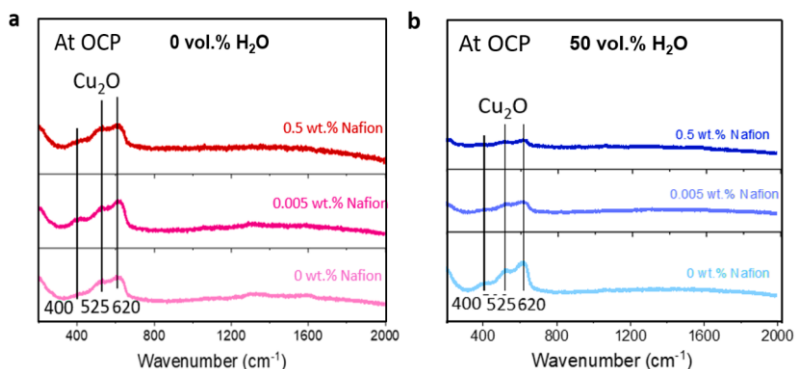
Figure 5.20 *In situ* Raman spectra recorded at open circuit potential (OCP) at the beginning of chronopotentiometry tests on 6 carbon paper-based electrodes formed with three different Nafion weight ratios (0 wt.%, 0.005 wt.%, and 0.5 wt.%) and two different water content (**a**, 0 vol.%; **b**, 50 vol.%) in CO_2 saturated 0.5 M $KHCO_3$.
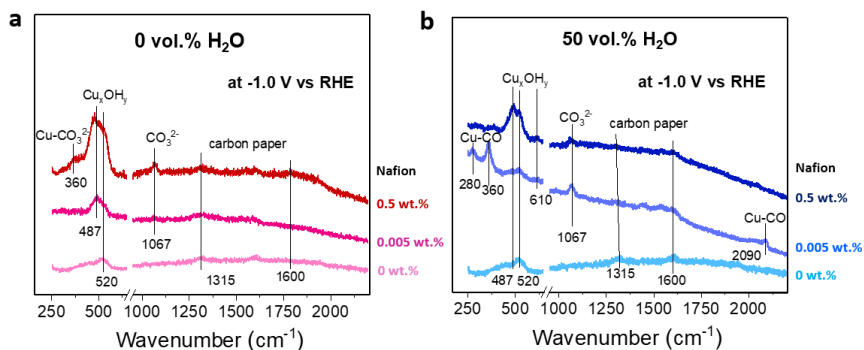
Figure 5.21 *In situ* Raman spectra recorded during chronoamperometry tests at -1.0 V vs. RHE on 6 carbon paper-based electrodes formed with 3 different Nafion weight ratios (0 wt.%, 0.005 wt.%, and 0.5 wt.%) and two different water content (**a**, 0 vol.%; **b**, 50 vol.%).

The specific Raman bands from the carbon paper substrates were observed on all electrodes, with peaks at around 1315 and 1600 cm^{-1} as shown in Figure 5.21. Remarkably, on the electrode with 50 vol.% H_2O and 0.005 wt.% Nafion, the sharp peak at 360 cm^{-1} (Cu-C linear stretching mode from adsorbed *CO on Cu)

111

accompanied by two additional peaks at 280 (Cu-CO rotation) and 2090 cm^{-1} (linear CO stretching mode) provide a direct indication for the presence of surface adsorbed CO (Cu-CO). More importantly, the peak intensity at 360 cm^{-1} was much higher than that at 280 cm^{-1}, which is consistent with a high CO surface coverage that is beneficial for C-C coupling to produce C$_{2+}$ products.[139,146] As a result, only the electrode with 50 vol.% H$_2$O and 0.005 wt.% Nafion demonstrated moderate CO FE of ~7.5% and the highest C$_2$H$_4$ FE of ~40% throughout 5 h of electrolysis and also the highest C$_{2+}$ FE of ~54% among all six carbon paper-based electrodes (Figure 5.18e, f and Figure 5.19e, f), in agreement with the *in situ* Raman spectroscopy data. In contrast, those characteristic peaks for Cu-CO were not detected on electrodes without Nafion or with high Nafion weight ratio (0.5 wt.%). Instead, carbonate bands at 360 (Cu-CO$_3^{2-}$) and 1067 cm^{-1} (CO$_3^{2-}$ symmetric stretching mode) and peaks between 480 and 610 cm^{-1} were observed,[140] particularly on the electrodes with 0.5 wt.% Nafion (Figure 5.21).

On Cu surfaces, high coverage of carbonates and hydroxides rather than high coverage of CO, is inevitably associated with strong HER and reduced C$_{2+}$ production. Correspondingly, electrodes without Nafion suffered from increasing H$_2$ FE from ~20% to >45% and decreasing C$_2$H$_4$ FE from ~40% to ~30% over 5 h. Electrodes with 0.5 wt% Nafion performed even worse, constantly possessing the highest H$_2$ FE and the lowest C$_2$H$_4$ FE within 5 h (Figure 5.18a, c and Figure 5.19a, c). Interestingly, the electrode with 0 vol.% H$_2$O and 0.005 wt.% Nafion also presented high C$_2$H$_4$ FE of ~40% and low H$_2$ FE of ~20% at the beginning of the experiment, but the production of CO and C$_2$H$_4$ continuously decreased and HER increased over 5 h.

Taken together, these findings reveal that only the combination of high water/alcohol fraction and low Nafion weight ratio in the solvent ink is able to provide a stable and favorable microenvironment with high CO surface coverage to facilitate C$_{2+}$ production in long-term CO$_2$ electrolysis.

5.8 Summary

In this work, we systematically studied the impact of Nafion/solvent formulations on CO_2 electrolysis using CuO as a model catalyst. Using high surface area carbon paper supports, the performance of electrochemical CO_2RR in terms of activity, selectivity, and stability was significantly influenced by varying Nafion/solvent formulation. Combining structural and morphological characterization of Nafion films and CLs with *in situ* spectroscopic analysis of the local microenvironment enabled specific insights into the role of Nafion on reaction outcomes. In particular, the impact of Nafion/solvent formulations on CO_2 electrolysis originates from three major aspects: the evolution of catalyst structure, modulation of local microenvironment, and accumulation of surface adsorbates. Specifically, morphological restructuring and delamination of weakly bound catalysts were effectively suppressed by addition of Nafion into the catalyst ink, resulting in partially stabilized product distributions. Furthermore, tuning both the thickness of Nafion films and their inner network connectivity by changing both the Nafion and water content in the catalyst ink formulations impacted the local concentrations of CO_2 and H_2O in the reaction microenvironment and the CO surface coverage, as evidenced by *in situ* Raman spectroscopy. Use of high water content solvents of 50-75 vol.% in catalyst inks is recommended to optimize the quality of Nafion films for improved CO_2RR performance.

Although this study addresses aqueous H-cell type reactor configurations, it is reasonable to expect that the strong dependence of ink formulations on catalyst performance characteristics will also be observed for other cell types, such as those comprising GDEs. While morphological stabilization by Nafion is likely to also play an important role in such systems, the higher operating current densities afforded by improved mass transport at the three-phase interface, as well as their operation under highly alkaline conditions, suggest that optimal Nafion thicknesses and internal structures will differ from those reported here, thus motivating analogous studies for GDEs electrodes in the future. Overall, these findings provide a scientific basis for understanding and designing Nafion/solvent formulations for manufacturing electrodes in CO_2 electrolysis, and motivate further innovation in

catalyst ink formulation development, including the use of novel ionomers and solvents specifically tailored for the desired electrochemical application.

Chapter 6. Tailoring Nafion/solvent formulations for enhanced Cu-assisted CO_2 electroreduction to multicarbon products on glassy carbon substrates

In the sixth chapter, the carbon paper substrate is replaced with a glassy carbon substrate, which is another widely used support material for electrode preparation in CO_2 electrolysis. Systematic investigations of the impact of Nafion/solvent formulations on Cu-catalyzed CO_2 electrolysis on glassy carbon substrates are explored from the following perspectives: the structure of the CLs, the CO_2 electrolysis performance (activity, selectivity and stability), and the structural evolution of catalysts. Particularly, the optimal Nafion/solvent formulation is examined for long-term CO_2 electrolysis dring 200 h of operation.

6.1 Introduction

As introduced in Chapter 5, by tuning the Nafion ionomer content and solvent composition of catalyst inks, Nafion thin films with varied structure and properties can be obtained, which can affect a variety of critical processes in Cu-catalyzed CO_2 electrolysis and lead to significant impacts on the activity, selectivity and stability. In particular, Nafion films can beneficially stabilize CLs and create favorable microenvironments, but can also cause the blocking of active sites or introduce undesired mass transport limitations. This complexity provides considerable opportunity for engineering hybrid Cu/ionomer catalyst interfaces with dramatically enhanced performance. On the other hand, as mentioned in Chapter

3.2, the properties of the substrate, such as its surface roughness, charge, and hydrophobicity, also play an important role in determining the final structure and properties of Nafion films. These understandings therefore motivate us to further explore the effect of Nafion/solvent on Cu-catalyzed CO_2 electrolysis on another widely used substrate, glassy carbon.

In this chapter, we systematically study the effect of Nafion ionomer films on electrochemical CO_2R catalyzed by oxide-derived Cu nanoparticles on glassy carbon substrates. By tuning the Nafion content and solvent composition of Nafion dispersions, the structure and properties of Nafion films and CLs can be readily modified as well, which is found to significantly influence the selectivity of C_{2+} products in CO_2R. With the optimal Nafion/solvent formulations, highly stable and selective production of C_{2+} products with maximum C_2H_4 FE of 65% and C_{2+} FE of 85% is realized in long-term CO_2 electrolysis of up to 200 h. Remarkably, the selectivity of C_{2+} products can be continuously improved over 200 h, which is attributed to electrochemical fragmentation of catalyst particles and efficient mass transport, enabled by Nafion films prepared with optimal Nafion/solvent formulations.

6.2 Effect on catalyst layers on glassy carbon

It is beneficial to first explore the effect of Nafion/solvent formulations on CLs. In this chapter, commercial CuO nanoparticles (NPs) are again used as the model catalyst and CLs are prepared by drop-casting ultrasonicated catalyst inks on glassy carbon substrates, followed with annealing at 80 °C on a hot plate (see details in Experimental Methods in Section A.12). As-prepared CLs and electrodes are first characterized by a variety of physical techniques, as described below.

6.2.1 Structural characterization of catalysts layers

The XRD data in Figure 6.1 and SEM images in Figure 6.2 and Figure 6.3 demonstrate the CuO nanoparticles are in pure monoclinic phase with average size of ~50 nm. As expected, the X-ray diffraction peaks of as-prepared CLs match

those of CuO, accompanied with a broad peak around 43° assigned to the glassy carbon substrate.
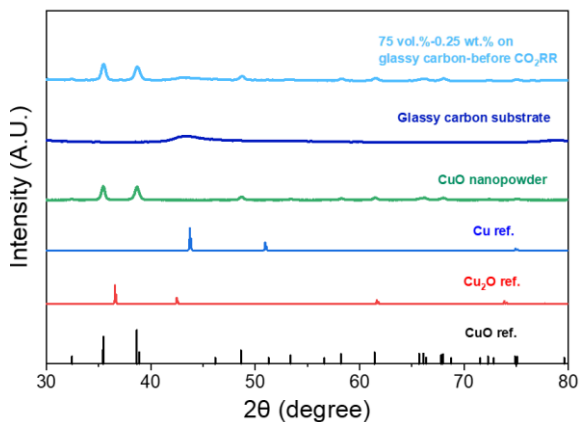
Figure 6.1 X -ay diffraction (XRD) data of references (CuO, Cu_2O and Cu), blank glassy carbon substrate and the best-performing electrode before and after CO_2 electrolysis prepared with optimal catalyst ink formulations (75 vol.% H_2O-0.25 wt.% Nafion on glassy carbon).

Figure 6.2 Scanning electronic microscopy (SEM) images of as-prepared catalyst layers deposited on glassy carbon prepared with catalyst slurries containing different Nafion weight ratios and different water contents.

In the absence of Nafion, large aggregates of CuO NPs were observed on glassy carbon regardless of water content, which resulted in th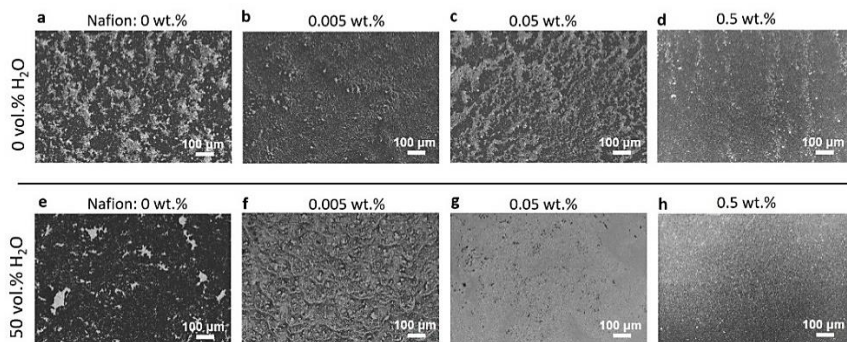e exposure of large areas of the bare glassy carbon substrate. In contrast, after adding Nafion into catalyst slurries, aggregations were drastically reduced and the surface coverage was improved. Moreover, the dispersity of Cu NPs generally increased with increasing of Nafion content. Finally, the CLs with the most uniform dispersions of CuO NPs on glassy carbon were obtained using formulations containing both high Nafion and water content (i.e., 50 vol.% H_2O and 0.5 wt.% Nafion, Figure 6.2h).

Figure 6.3 Magnified scanning electronic microscopy (SEM) images of catalyst layers deposited on glassy carbon prepared with catalyst slurries containing 0.25 wt.% Nafion and different water contents, namely 0 vol.% (**a**), 25 vol.% (**b**), 50 vol.% (**c**), and 75 vol.% (**d**).

Magnified SEM images in Figure 6.3 revealed that at the same Nafion content of 0.25 wt.%, the CL prepared with the formulation of 0 vol.% H_2O apparently displayed thicker Nafion films around CuO NPs than those prepared with the formulation of 75 vol.% H_2O, consistent with our findings on CLs on carbon paper substrates in Figure 5.2. These findings are also in good agreement with our previous studies regarding Nafion film thicknesses on Si substrates in Chapter 4.

6.2.2 Hydrophobic properties of catalysts layers

The structure of CLs, including surface roughness, chemistry, and modifications, plays a critical role in determining their hydrophobic behavior. Thus, to evaluate the effect Nafion modifications, we analyzed the hydrophobicity of CLs by measuring the contact angles of deionized water on the surface of CLs produced with various Nafion/solvent formulations (Figure 6.4). The water contact angle test is a type of surface characterization technique used to estimate the wettability of a solid surface. The test involves placing a droplet of water onto a flat surface and measuring the angle between the droplet and the surface (see Experimental Methods in Section A.6). Regardless of solvent composition, the bare CuO catalyst layer is hydrophilic with contact angles below 50°, implying it has a high affinity for water and the droplet will spread out over the surface (Figure 6.4a, e).
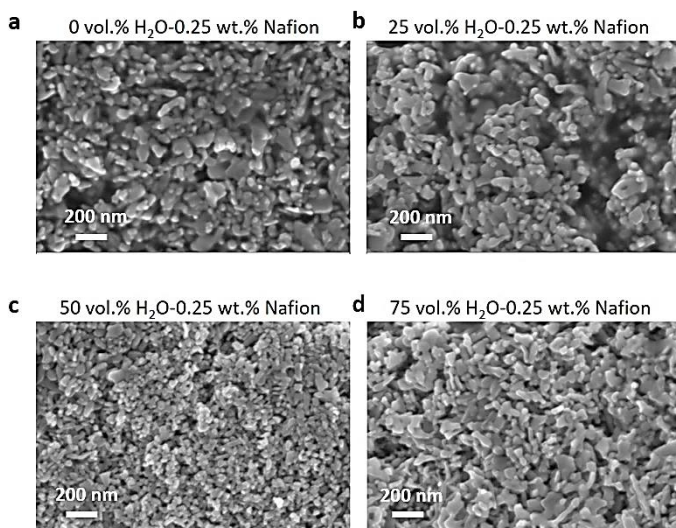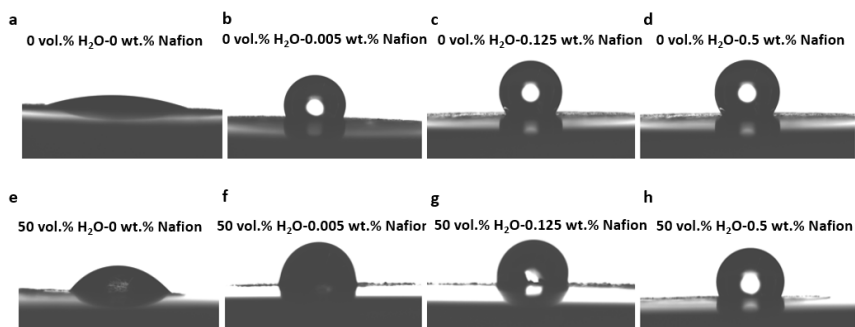

Figure 6.4 Magnified scanning electronic microscopy (SEM) images of catalyst layers deposited on glassy carbon prepared with catalyst slurries containing 0.25 wt.% Nafion and different water contents, namely 0 vol.% (**a**), 25 vol.% (**b**), 50 vol.% (**c**), and 75 vol.% (**d**).

In contrast, all Nafion-containing CLs are hydrophobic, with measured contact angles of >90°, indicating that such layers repel water molecules. Moreover, the contact angles tended to increase with increasing Nafion content, which suggests enhanced hydrophobicity after adding Nafion into catalyst slurries (Figure 6.4 and Figure 6.5).

Figure 6.5 Contact angles of deionized water on catalyst layers prepared with slurries with four Nafion weight ratios (0, 0.005, 0.125 and 0.5 wt.%) and two water contents (0 and 50 vol.%). Contact angle data are obtained from the images presented in Figure 6.4.

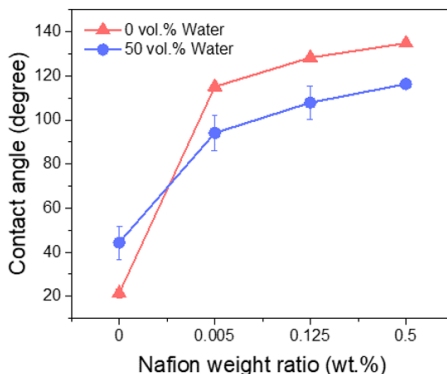Notably, Nafion-coated CLs prepared without water exhibit superior hydrophobicity relative to those prepared with formulations of 50 vol.% H_2O. It is known that surface roughness enabled by micro- or nano- structures is able to enhance hydrophobicity[147]. Given the rough surface with hierarchical nanostructures observed previously in the 3D AFM images (see Figure 4.4 and Figure 4.5) of Nafion films prepared with water-free formulations, we infer that Nafion films with high surface roughness prepared with low-water-content formulations accounts for the enhanced hydrophobicity.

Thus, combining the insights from both Nafion films and CLs, we conclude that the impact of Nafion/solvent formulation on Nafion films can be preserved on CLs on glassy carbon substrates.

6.3 Dependence of CO_2 electrolysis performance on Nafion/solvent formulations

We first applied electrochemical characterization methods to investigate the dependence of CO_2 electrolysis performance on Nafion/solvent formulations on

glassy carbon-based electrodes. For this, the electrodes prepared with various Nafion/solvent formulations were examined during CO_2 electrolysis at different applied potentials and their functional characteristics were compared.

Following the established procedures for carbon paper-based electrodes in Chapter 5, we utilized Nafion/solvent formulations with four Nafion weight contents (0, 0.005, 0.05 and 0.5 wt.%) and two water fractions (0 and 50 vol.%, balance of isopropanol) to produce catalyst slurries, followed by deposition on glassy carbon substrates to fabricate working electrodes with a constant mass loading of 0.255 mg cm^{-2}. The resulting eight working electrodes were then examined in a conventional H-cell filled with CO_2 saturated 0.1 M $KHCO_3$ aqueous electrolyte. The current densities and gaseous products were analyzed during the course of 1 h CO_2 electrolysis at seven different potentials.

Notably, regardless of water content, no CO_2 electrolysis was observed from either of the electrodes prepared without Nafion. Indeed, as shown in Figure 6.6a, product quantification on these Nafion-free electrodes under CO_2 electrolysis conditions at a fixed potential of -1.0 V vs. RHE yielded H_2 as the sole gas product with FEs of ~100%. SEM images of these electrodes after electrolysis revealed complete loss of CLs from the surface, indicating negligable activity for CO_2RR due to exfoliation of CLs from the glassy carbon substrates, even during the CV scanning (Figure 6.6b, c). Thus, in contrast to the Nafion-free electrodes on carbon paper substrates, the interaction between CLs and glassy carbon substrates is too weak to permit CO_2 electrolysis. We believe that this is a consequence of the smooth and comparatively inert surface of glassy carbon substrates, which prohibits physisorbed catalyst nanoparticles from being stabilized without Nafion binder. In contrast, the porous structure of carbon paper substrates helps to physically constrain catalyst nanoparticles from immediate detachment, though CO_2RR performance degradation is also observed on those substrates when Nafion is not present in the CLs.
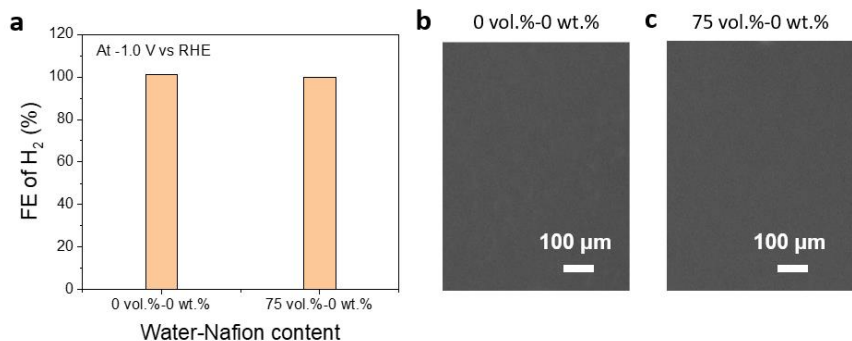
Figure 6.6 (**a**) The measured Faradaic efficiency of H_2 in CO_2 electrolysis at a fixed potential of -1.0 V vs RHE in CO_2 saturated 0.1 M $KHCO_3$ electrolyte on two electrodes prepared with Nafion-free formulations (0 vol.% H_2O-0 wt.% Nafion and 75 vol.% H_2O-0 wt.% Nafion). (**b**, **c**) SEM images of these two electrodes after CO_2 electrolysis.

Based these results, we concluded that for glassy carbon-based electrodes, Nafion ionomer is essential to ensure not only good dispersion of catalyst particles but also, more importantly, the stability of CLs. Thus, only Nafion-containing electrodes were further evaluated in CO_2 electrolysis.

For the case of CLs containing Nafion binder, the total current densities (TCDs) tended to increase with decreasing Nafion content, as shown in Figure 6.7a. Indeed, the maximum TCDs of approx. -20 mA cm^{-2} near -1.05 V vs. RHE were achieved at the lowest Nafion content of 0.005 wt.%. In particular, for the highest Nafion content of 0.5 wt.%, the electrode prepared with 50 vol.% H_2O yielded larger TCDs than that prepared without water across the whole potential range. We ascribe such enhanced TCDs at higher water content to the larger electrochemically active surface areas of CLs produced from high-water-content formulations, as estimated in Figure 5.6a, which is also accordance with the findings on carbon paper substrates.

Figure 6.7 Effect of Nafion/solvent formulations on potential-dependent CO_2 electrolysis in CO_2 saturated 0.1 M $KHCO_3$. Catalytic performance of glassy carbon-based electrodes prepared by different Nafion/solvent formulations evaluated in terms of total current density (**a**), and partial current density of CO (**b**), CH_4 (**c**), and C_2H_4 (**d**).

The potential-dependent partial current densities and FEs of gaseous products are plotted in Figure 6.7 and Figure 6.8, respectively. In addition, these two groups of data are also plotted in a merged format in Appendix Figure B7 and Figure B8, respectively. On all electrodes, C_2H_4 and H_2 were detected as two major products, together accounting for a cumulative FE of ~75%. HER was significantly suppressed near -1.0 V vs. RHE and the minimum H_2 FE of ~16% was obtained on the electrode prepared by the formulation containing 50 vol.% H_2O and 0.005 wt.% Nafion. As for the production of C_2H_4, the optimal potential was shifted to -1.05 V vs. RHE and the maximum C_2H_4 FE was as high as ~56% on the electrode

prepared with 50 vol.% H_2O and 0.5 wt.% Nafion. Moreover, the production of C_2H_4 was generally favorable, in terms of higher C_2H_4 FEs, on electrodes prepared from high-water-content formulations relative to those prepared with water-free formulations (Figure 6.8d).
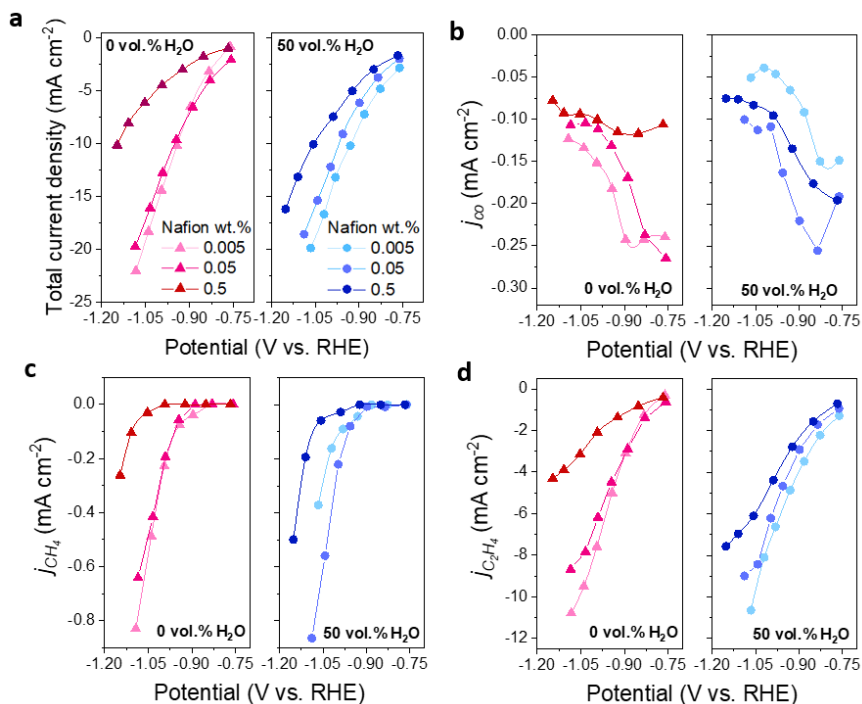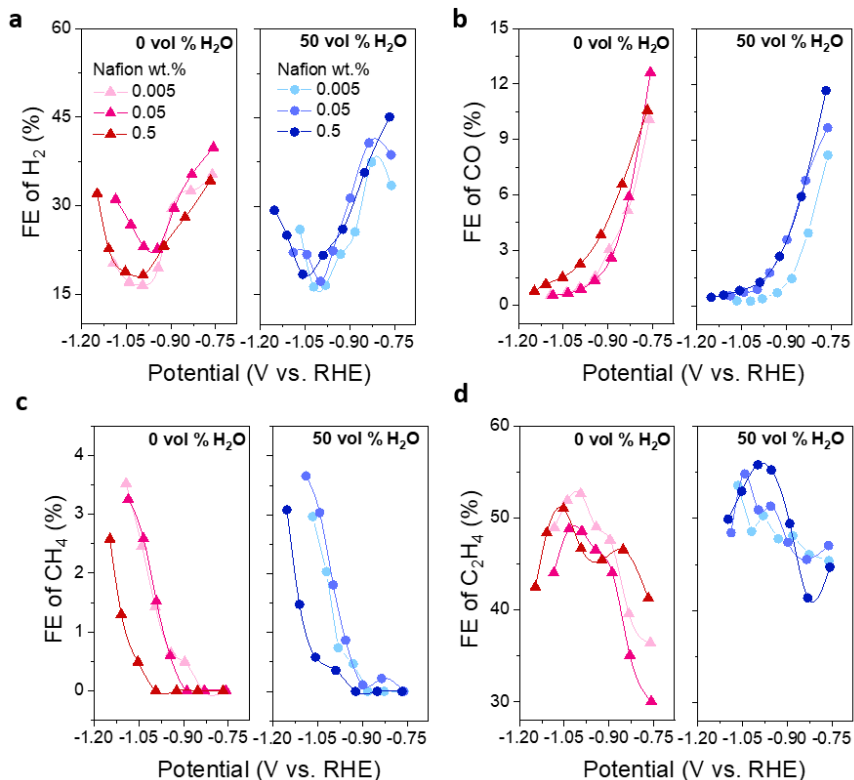

Figure 6.8 Effect of Nafion/solvent formulations on potential-dependent CO_2 electrolysis in CO_2 saturated 0.1 M $KHCO_3$. Catalytic performance of glassy carbon-based electrodes prepared by different Nafion/solvent formulations evaluated in terms of Faradaic efficiency of H_2 (**a**), CO (**b**), CH_4 (**c**), and C_2H_4 (**d**).

CO and CH_4 were also detected as minor products. Briefly, electrodes prepared with the highest Nafion content of 0.5 wt.% afforded relatively higher CO FEs and lower CH_4 FEs. At -1.05 V vs. RHE, CO FEs were reduced to less than 1% on all electrodes, while CH_4 FEs were only suppressed to <1% on electrodes prepared

with formulations of the highest Nafion content (Appendix Figure B9). The CH_4 FE has been reported to be an indicator for local pH in CO_2 electrolysis, as the production of one single CH_4 molecule from CO_2 requires the consumption of 8 protons.[148] The extremely low CH_4 FE measured on electrodes prepared with formulations of the highest Nafion content implies that thicker Nafion films probably result in higher local pH, thus suppressing HER and promoting the selectivity of C_{2+} products.[12,148,149]

Overall, we confirmed a strong dependence of CO_2 electrolysis performance on Nafion/solvent formulations on glassy carbon substrates, though the absolute FEs and their specific trends with ink composition differed from those observed on carbon paper. Nevertheless, it should be noted that the optimal potential for CO_2R to multicarbon products (i.e., the potential with lowest HER and highest selectivity for C_2H_4) on glassy carbon-based electrodes is always measured at approximately -1.0 V vs. RHE, which is consistent with the optimal potential determined on carbon paper-based electrodes in Chapter 5. This finding suggests that the overall intrinsic catalytic activity of CuO-derived catalysts is not affected by Nafion/solvent formulations or substrate type. Thus, we conclude that the impact of Nafion/solvent formulations on CO_2 electrolysis performance can be attributed to modified mass transport efficiencies and local microenvironments controlled by Nafion films.

6.4 Determining the optimal Nafion/solvent formulation

As a next step, we continue to systematically assess the effect of Nafion/solvent formulations on the selectivity of CO_2R in longer CO_2 electrolysis experiments (Figure 6.9) and identify the optimal Nafion/solvent formulation for production of multicarbon products on glassy carbon-based electrodes. Notably, it is very hard to define the optimal Nafion/solvent formulation as the production of multicarbon products is determined by both selectivity (FE) and yield (corresponding partial current density). To quickly screen the effect of Nafion/solvent formulations, we chose the chronopotentiometry tests at a fixed current density of -12.8 mA cm^{-2}, which was selected to correspond to the conditions that generate relatively higher

FE and larger partial current density for multicarbon products for the majority of electrodes (as shown in Figure 6.7 and Figure 6.8).
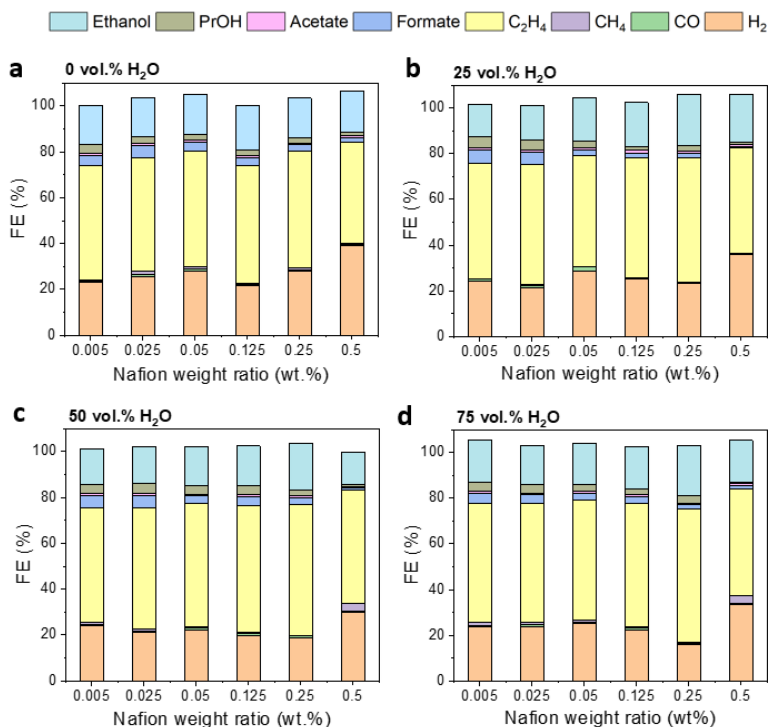
Figure 6.9 Product distributions from Nafion-containing CLs during chronopotentiometric CO_2 electrolysis at a total current density of -12.8 mA cm^{-2} in CO_2 saturated 0.1 M $KHCO_3$. The electrodes were prepared with various Nafion/solvent formulations containing six different Nafion weight ratios (0.005, 0.025, 0.05, 0.125, 0.25, and 0.5 wt.%) and four different water contents, namely 0 (**a**), 25 (**b**), 50 (**c**), and 75 (**d**) vol.%.

For this, a series of Nafion/solvent formulations with six Nafion contents (0.005, 0.025, 0.05, 0.125, 0.25 and 0.5 wt.%) and four water contents (0, 25, 50 and 75 vol.%) were employed to produce working electrodes. All electrodes were examined in 5 h chronopotentiometry tests at a constant current density of -12.8

mA cm^{-2} and both gas and liquid products, including H_2, CO, CH_4, C_2H_4, formate, ethanol, acetate, and n-propanol, were quantified.

The product distribution obtained from each electrode is presented in Figure 6.9. To analyze the influence of Nafion/solvent formulations on the selectivity of each product, the average FE within 5 h was individually compared in heatmaps (Figure 6.10 and Appendix Figure B9). For most formulations, the H_2 FE was maintained at a value of approximately 25%. However, the HER is highly dependent on water content at the highest Nafion content of 0.5 wt.%. Severe HER, with H_2 FE of ~40%, was measured at 0 vol.%-0.5 wt.%, which was improved at even higher Nafion content. The lowest H_2 FEs around 16% were recorded for the combination of relatively high Nafion content of 0.25 wt.% and high water content (i.e., 50-75 vol.%). Accordingly, in this HER-suppressed region the selectivity towards CO_2R was significantly enhanced (Figure 6.10a and Figure 6.11a).

In particular, the FEs of C_2H_4 were increased to a remarkable value of ~58% in this region. Similarly, the production of another major C_{2+} product, namely ethanol, was promoted as well, with FEs above 20% in the region of high Nafion content (i.e., 0.25-0.5 wt.%) and relatively high water content (i.e., 25-75 vol.%). The FEs of other C_{2+} products, such as acetate and n-propanol, were moderate in this high-Nafion-content region. Instead, the FEs for these products reached maximum values for low Nafion content CLs (i.e., <0.025 wt.%). The total FE of acetate and n-propanol was nonetheless always below 5%. Thus, the production of C_{2+} products was maximized, with a significant FE of ~84%, on electrodes prepared with formulations containing 0.25 wt.% Nafion and >25 vol.% H_2O (Figure 6.11c and Appendix Figure B9f, h).
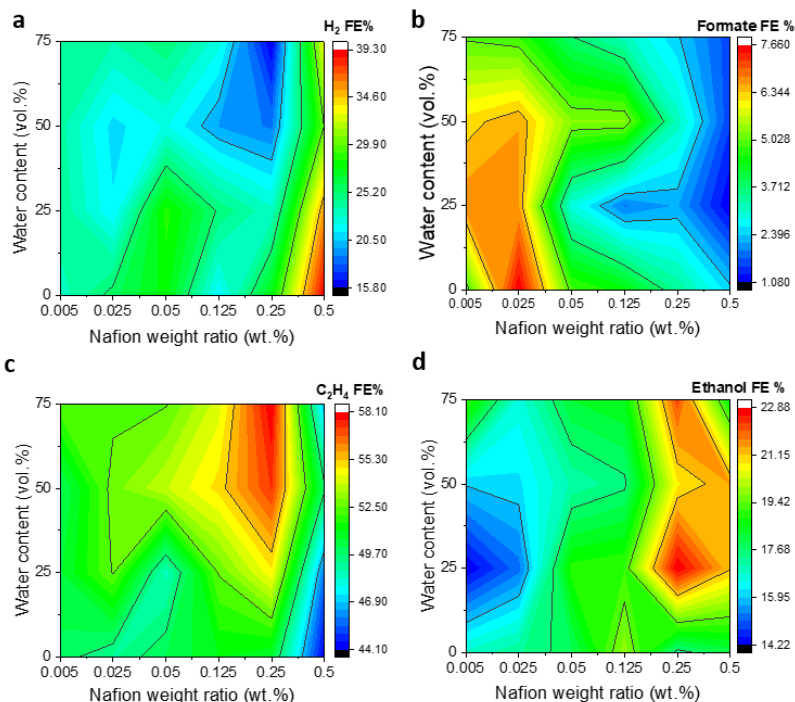
Figure 6.10 Effect of Nafion/solvent formulations on selectivity during chronopotentiometric CO_2 electrolysis at -12.8 mA cm^{-2} in CO_2 saturated 0.1 M $KHCO_3$. Heatmaps of Faradaic efficiency of four major products: H_2 (**a**), formate (**b**), C_2H_4 (**c**), and ethanol (**d**).

In contrast to C_{2+} products, the selectivities of single carbon (C_1) products such as CO and CH_4 were much lower on all electrodes, with <1.8% CO and <3.7% CH_4 (Appendix Figure B9b, c). Formate is the only major C_1 product and its FE demonstrates a strong dependence on Nafion content. Specifically, increasing Nafion content causes a steady decrease of formate production regardless of water content, with the corresponding FE falling from a peak value of 7.6% at 0.005 wt.% Nafion to 1% at 0.5 wt.% Nafion (Figure 6.10b). Considering the minimal FEs of both CO and CH_4, the overall production of C_1 products is predominantly given by formate production, which is primarily influenced by Nafion content rather than water content (Appendix Figure B9b, c). Moreover, the ratio of C_{2+} FE to C_1 FE

(C_{2+}/C_1) also displayed a strong dependence on Nafion content, as illustrated in Figure 6.11d
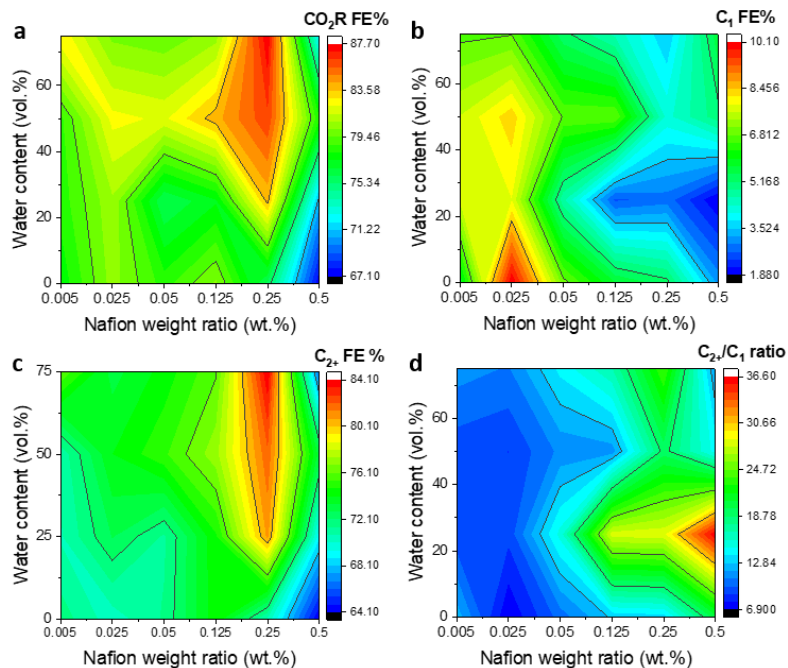
Figure 6.11 Effect of Nafion/solvent formulations on selectivity of chronopotentiometric CO_2 electrolysis at -12.8 mA cm^{-2} in CO_2 saturated 0.1 M KHCO$_3$. Heatmaps of Faradaic efficiency of all CO_2R products (**a**), single carbon products (**b**), multicarbon products (**c**), and the C_{2+}/C_1 FE ratio (**d**).

As presented before in Chapter 4, formulations with higher Nafion content are primely responsible for creating thicker Nafion films. These results suggest that by tuning the thickness of Nafion films the competition between C_{2+} and C_1 reaction pathways can be modulated. Indeed, it has been shown in previous studies that thick Nafion films can raise local pH values by trapping hydroxide ions (OH$^-$) generated in CO_2 electrolysis and preventing buffering carbonate species from entering the local microenvironment, thereby reducing HER and enhancing C_{2+}

selectivity.[12] Our results are consistent with such a model, though additional experiments would be necessary to probe the local pH during reaction.

Remarkably, the optimal ink formulation is considerably different for electrodes based on two different substrates: carbon paper and glassy carbon. Overall, although formulations with high water content always promote CO_2RR, the optimal formulation for C_{2+} products on carbon paper substrate lies only in the region of low Nafion content, whereas it requires a much higher Nafion content for glassy carbon-based electrodes. There are a couple of reasons for this discrepancy. Firstly, the structure of Nafion and, consequently, the mass transport and local environment, can be affected by Nafion's interactions with different supporting substrates. Secondly, it likely has to do with how the catalysts are situated either on a planar surface (for glassy carbon-based electrodes) or within a porous structure (for carbon paper-based electrodes), which provides additional confinement for reactants and/or intermediates. Thirdly, it may also be related to the different operating current densities and, thus, different reaction rates. These possibilities can ideally be verified through future experiments that could help elucidate the differences at a mechanistic level.

6.5 Long term CO_2 electrolysis on glassy carbon

Having obtained a maximum C_{2+} FE of 84% during 5 h CO_2 electrolysis on the electrode prepared with the optimal formulation of 75 vol.% H_2O and 0.25 wt.% Nafion, we subsequently assessed its durability for 100-200 h (each cycle of ~40 h) of chronopotentiometric CO_2 electrolysis. After each cycle, both catholyte and anolyte were competed removed and refreshed with CO_2 saturated 0.1 M $KHCO_3$ to continue the next cylcle. Gas products were analyzed by online GC every 20 min and Liquid products in electrolytes were detected by ^{1}H NMR.

Figure 6.12 demonstrates the first long-term durability test on an electrode prepared with the ink formulation of 75 vol.% H_2O and 0.25 wt.% Nafion. In the first 10 h , the C_2H_4 FE rose from a beginning value of ~57% to ~60%. Despite relatively large fluctuations of FE during the subsequent 40 h of operation, most likely due to

bubble accumulation and release, the average C_2H_4 FE sustained a value of ~60%. At the same time, the HER activity was continuously reduced, with the H_2 FE dropping from 22.5% to <20%. Consistent with the results presented above during shorter-term experiments, the production of CO and CH_4 was minimal, with corresponding FEs both around 1%.
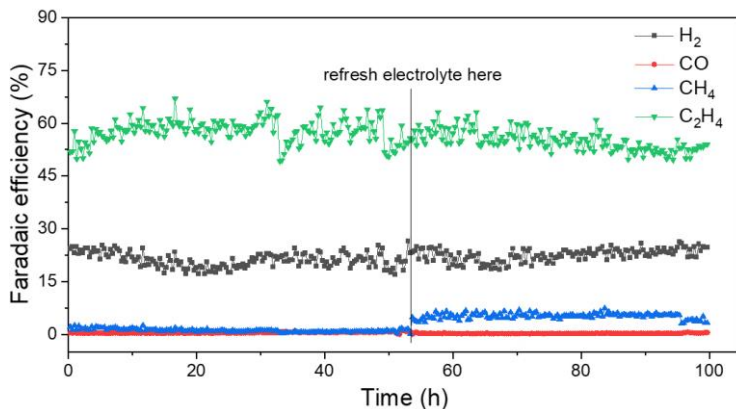

Figure 6.12 Evaluation of durability in 100 h chronopotentiometric CO_2 electrolysis at -12.8 mA cm^{-2} in CO_2-saturated 0.1 M $KHCO_3$ on glassy carbon. The electrode was prepared with the ink formulation of 75 vol.% H_2O and 0.25 wt.% and the dynamic change of FEs of gas products was monitored every 20 min by online GC over 100 h.

During the exchange of electrolyte, the working electrode was placed in air and was then remounted to restart CO_2 electrolysis. Surprisingly, the production of C_2H_4 deteriorated gradually following the electrolyte exchange. This decrease in C_2H_2 FE was accompanied by constant rise of the H_2 FE. Moreover, the FE of CH_4 was suddenly increased to ~5% following electrolyte exchange, and was very stable at this value thereafter. Such a significant change in selectivity between the first and second cycle was likely caused by oxidation of metallic Cu catalysts when exposed to air during the electrolyte exchange process. To minimize the effect of re-oxidation of the catalyst in air, the working electrode was protected in CO_2-saturated 0.1 $KHCO_3$ solution when exchanging electrolyte in subsequent durability tests.
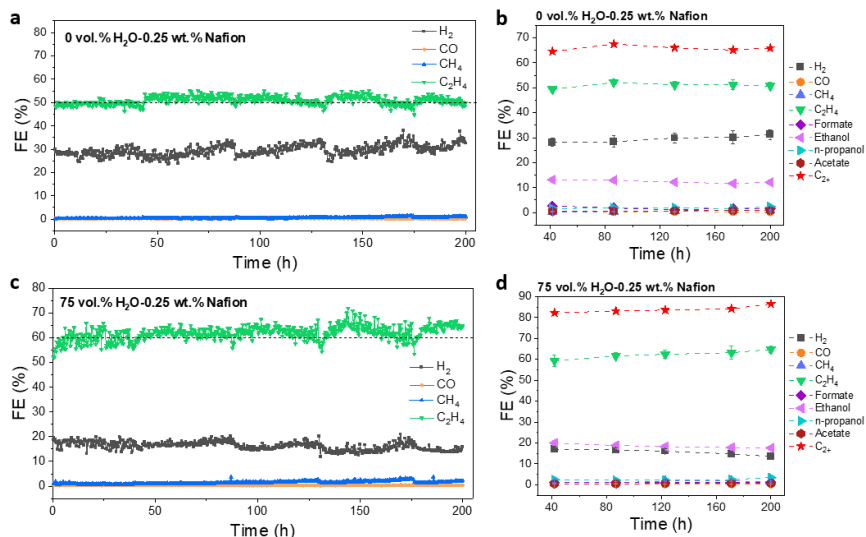
Figure 6.13 Evaluation of durability of two different electrodes, one with 0 vol.% H_2O 0.25 wt.% Nafion **(a,b)** and one with 75 vol.% H_2O-0.25 wt.% Nafion (**c,d**), during 200 h chronopotentiometric CO_2 electrolysis at -12.8 mA cm^{-2} on glassy carbon. The dynamic change of FEs of gas products were monitored every 20 min over the course of 200 h by GC (**a**, **c**). Also plotted are the average FEs of all products in each stage of ~ 40 h (**b**, **d**), between which the electrolyte was exchanged.

Armed with knowledge of how to handle electrodes during electrolyte exchange, we proceeded to perform long-term stability tests on two electrodes, one with 0 vol.% H_2O-0.25 wt.% Nafion (Figure 13a,b) and one with 75 vol.% H_2O-0.25 wt.% Nafion (Figure 13c,d). Overall, the 75 vol.% H_2O-0.25 wt.% Nafion electrode exhibited a sustained high CO_2R performance throughout the complete 200 h durability test. Importantly, the C_2H_4 FE increased from ~55% at the beginning to ~60% after about 40 h and constantly rose over time, eventually reaching a peak averaged FE of 65% for the last ~30 h, an overall increase of ~19%. As a trade-off, HER and the production of ethanol were both progressively reduced during the 200 h experiment, with the averaged FEs of H_2 and ethanol dropping from 17% and 20% to 13% and 17%, respectively (Figure 6.13a). At the same time, the production of all other minor products, including CO, CH_4, formate, acetate and n-propanol, was maintained at

132

minimal levels, accounting for FEs that varied from 0.5% to 3%. Hence, the FE of C_{2+} products presented a steady increase over the course of 200 h and peaked at a stunning value of 87% (Figure 6.13b).

As a comparison, we also measured the electrode prepared by the formulation of 0 vol.% H_2O and 0.25 wt.% Nafion during a 200 h CO_2 electrolysis experiment (Figure 6.13c, d). Although this electrode also demonstrated robust stability, the FEs of both C_2H_4 and ethanol were significantly lower than those measured on the previous electrode, stabilizing around 50% and 12% during 200 h, respectively. In addition, the H_2 FE nearly doubled and gradually increased from 28% to 31% (Figure 6.13c). The FE of C_{2+} products consequently was estimated to be ~65%, a net drop of >20% compared to the 75 vol.% H_2O-0.25 wt.% Nafion electrode (Figure 6.13d). In addition, we also compared the potential-dependent CO_2 electrolysis (1 h for each potential) performance on these two electrodes. Generally, the electrode prepared with the formulation of 75 vol.% H_2O exhibited larger TCDs, higher C_2H_4 FEs, and lower FEs for H_2, CO and CH_4 across nearly the entire potential range compared to the electrode prepared with the water-free formulation (Figure 6.14). The superior activity for C_{2+} production on the 75 vol.% H_2O-0.25 wt.% Nafion electrode relative to the 0 vol.% H_2O-0.25 wt.% Nafion electrode is primarily a consequence of the maximum C_2H_4 FEs from each electrode, which were measured to be approx. 60% and 50%, respectively, as shown in Figure 6.13.

The sole difference between these two electrodes lies in the water content of the solvent used to prepare the CLs. The most convincing explanation for the dramatic performance differences can therefore be derived by considering the varying properties of Nafion films caused by solvent effects. As presented previously in the AFM images of Figure 4.5, the electrode prepared with the high water content is characterized by thin Nafion films with high inner network connectivity, while the one prepared with the water-free formulation exhibits more swelling and thick Nafion films with poor inner network connectivity. Thus, mass transport, namely the transfer of reactants, reaction intermediates, and products, may be improved on the electrode with thin Nafion films, hence enhancing the overall CO_2R performance. It should be noted that the C_{2+} selectivity would be particularly

promoted as such reactions require more sophisticated pathways involving a larger number of intermediates and reactants (e.g., protons).[4] Additionally, the enhanced production of C_{2+} products could also be assigned to favorable reaction microenvironment enabled by high-water-content formulations as demonstrated in Chapter 5 on carbon paper substrate, which can be verified by *in situ* Raman spectroscopy in future experiments.
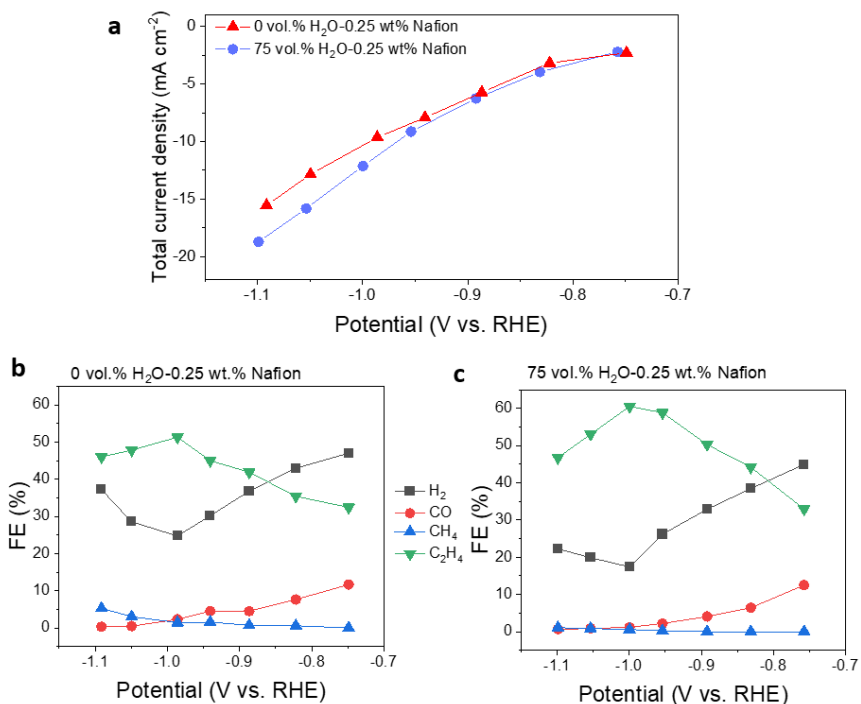
Figure 6.14 Potential-dependent performance in CO_2 electrolysis in CO_2-saturated 0.1 M $KHCO_3$ on electrodes prepared with formulations of 0 vol.% H_2O 0.25 wt.% Nafion and 75 vol.% H_2O 0.25 wt.% Nafion. The measured total current density (**a**) and Gas production distribution (**b**, **c**) on two electrodes.

Even though more efficient mass transport and favorable local reaction environment could account for the relatively higher C_{2+} selectivity on the electrode prepared with formulations on 75 vol.% H_2O, the reason for the continual

enhancement of the FE of C_{2+} products, especially C_2H_4, during the course of the 200 h experiment remains unclear. As shown in Table 6.1, the majority of previous studies have run durability tests of Cu-assisted CO_2 electrolysis for less than 10 h due to the inevitable degradation of catalytic activity. One exception reported electrochemically fragmented Cu_2O NPs, which decreased in size from 20 nm to 2-4 nm during the course of 10 h CO_2 electrolysis, which was found to double the FE of C_2H_4 from 27% to 57%.[150] This previous observation provides an important hint at the observed time-depenent selectivity of our CLs, as described below.

Table 5.1. Comparison of optimized production of C_{2+} products on various Cu-based catalysts in neutral-pH aqueous electrolyte previously reported in literature.

Catalyst	Nafion/H_2O content (%)	Electrolyte	Substrate	E vs. RHE	FE% C_2H_4/ C_{2+}	j (mA cm^{-2})	Time (h)	Ref
Cu foil	0 / N/A	0.1 M KHCO$_3$/CsHCO$_3$	Cu foil	-0.98	30 / 42	-5	0.5	[151]
		0.1 M KCl		-1.03	48 /73	-5	0.5	
Oxidized Cu foil	0 / N/A	0.1 M KHCO$_3$	Cu foil	-1.0	10 / 19	-5	1.2	[152]
Plasma treated Cu foil	0 / N/A	0.1 M KHCO$_3$	Cu foil	-0.92	57 / N/A	-12	5	[153]
CuO NPs	0 / N/A	0.5 M KHCO$_3$	glassy carbon	-0.95	20 / 57	-30	5	[154]
Branched CuO NPs	5 / 0	0.1 M KHCO$_3$	glassy carbon	-1.05	65 / 65.5	~25	12	[155]
Cu$_2$O NPs, 18 nm 41nm	0 / N/A	0.1 M KHCO$_3$	Cu disc	-1.03 -1.03	43 / N/A 10 / N/A	-31 -31	1.2 1.2	[156]
Cu$_2$O NPs, 2-4 nm	0.15 / 0	0.1 M KHCO$_3$	glassy carbon	-1.10	57 / 74	-17	10	[150]
Cu NPs, 10-40 nm	0 / 0	0.1 M CsHCO$_3$	carbon paper	-0.75	30 / 50	-20	10	[157]
Plasma treated Cu NCs	0 / N/A	0.1 M KHCO$_3$	Cu foil	-1.0	44 / 64	-34	1	[158]

CumCeOx	0.12 / 50	0.1 M KHCO3	glassy carbon	-1.10	>40 / N/A	-3.2	6	[127]
Boron-doped Cu	0.10 / 0	0.1 M KHCO3, 0.1 M KCl	glassy carbon	-1.10	52 / 79	-75	40	[159]
Cu NWs	0.05 / 0	0.1 M KHCO3	glassy carbon	-1.01	61-72 / N/A	-22	205	[53]
Defective Cu NSs	0.24 / 0	0.1 M K2SO4	glassy carbon	-1.18	80 / N/A	-60	14	[160]
CuO	0.25 / 75	0.1 M KHCO3	glassy carbon	-1.10	57-67 / 87	-13	200	This work

Note: the listed Nafion and water content are in the unit of wt.% and vol.%, respectively.

To assess whether electrochemical fragmentation could be contributing to the improved performance, we performed SEM imaging before and after 200 h of operation. As shown in Figure 6.15, the starting catalyst particle size on as-prepared electrodes was ~50 nm, regardless of the catalyst ink formulation. Remarkably, a large coverage of Cu NPs smaller than 20 nm were observed on the best-performing electrode (75 vol.% H_2O -0.25 wt.% Nafion) after 200 h of electrolysis, indicating pronounced electrochemical fragmentation (Figure 6.15c, d). In sharp contrast, the size of Cu NPs on the electrode prepared with the water-free formulation was well preserved (Figure 6.15a, b). Considering that only the electrode prepared without water does not undergoe this fragmentation process and does not exhibit improved C_{2+} FE with time (and *vice versa* for the electrode prepared with water), we thus conclude that this morphological evolution of the catalyst is critical for achieving such high selectivity to higher order products.
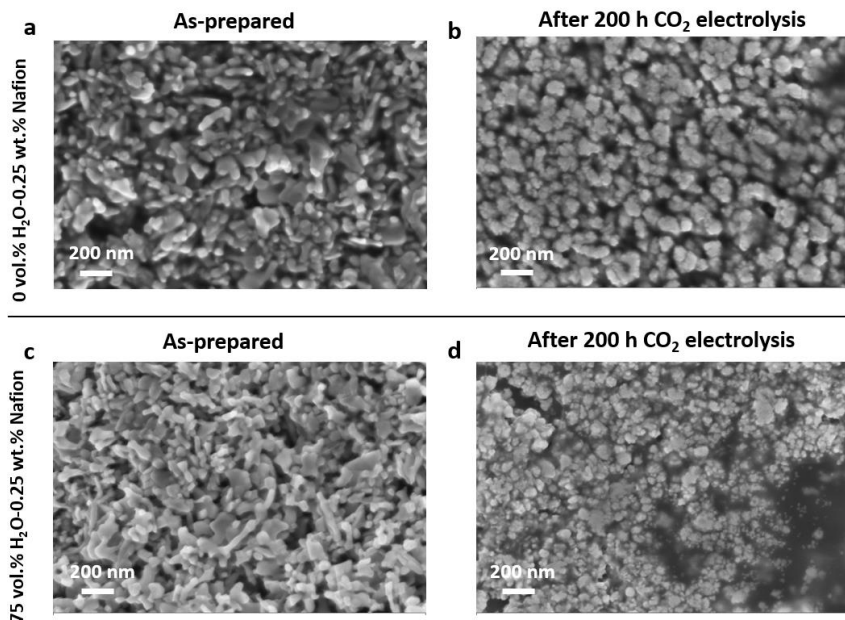
Figure 6.15 SEM images of catalyst layers before and after 200 h of CO_2 electrolysis. The catalyst layers were prepared with the formulation of 0 vol.% H_2O-0.25 wt.% Nafion (**a & b**) and 75 vol.% H_2O-0.25 wt.% Nafion (**c & d**).

Considering the dynamic changes to the catalytic structure during operation, we further analyzed the concentration of Cu^{2+} ions in the electrolytesafter each period of electrolysis (i.e. after each 40 h when electrolyte was replaced) by inductively coupled plasma mass spectrometry (ICP-MS). After the first period of ~40 h, we detected a high Cu content for the best-performing electrode, with a Cu^{2+} concentration of 19.1 µg L^{-1}, which is nearly twice the value (9.8 µg L^{-1}) for the electrode prepared with the water-free formulation. Afterwards, the Cu contents for both electrodes dropped to a lower level (with ~5 µg L^{-1} Cu^{2+}) but the Cu content for the best-performing electrode was constantly higher than the other one (Figure 6.16). The relatively higher Cu ion concentration in electrolyte is very likely associated with higher level of dissolution and electrochemical fragmentation of Cu catalysts on the electrode based on 75 vol.% H_2O-0.25 wt.% Nafion.
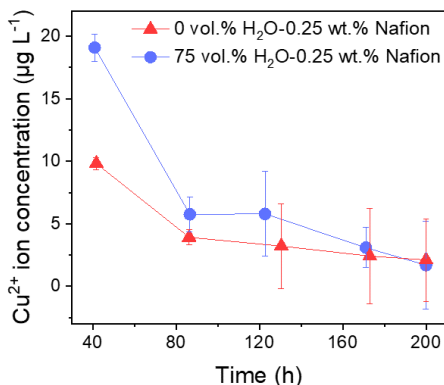
Figure 6.16 Characterization of electrolytes after each period of CO_2 electrolysis during the 200 h stability experiments. Concentrations of Cu ions in electrolytes collected after each electrolyte replacement during of CO_2 electrolysis were measured by inductively coupled plasma mass spectrometry (ICP-MS).

The dissolution of copper into the electrolyte during the electrochemical fragmentation process can also be affected by local pH changes near the copper catalyst surface. The pH near the catalyst surface can be different from the bulk pH of the electrolyte due to the consumption of protons during electrochemical reduction reactions (i.e., HER and CO_2RR). At the cathode, where the reduction of CO_2 occurs, protons are quickly consumed to form reduced products. This can lead to an increase in local pH near the catalyst surface, which can promote the oxidation of copper and the subsequent dissolution of copper ions into the electrolyte. On the other hand, Nafion can also affect the local pH near the catalyst surface, since Nafion has a high proton conductivity but a poor conductivity for anions such carbonate and hydroxide ions. Thus, Nafion ionomer films around Cu catalysts are able to confine locally formed hydroxide ions during the consumption of protons and block the transport of buffering carbonate ions from bulk electrolyte to catalyst surface, thus increasing the local pH and promoting the dissolution and fragmentation of the copper catalyst.

Based on these results, we propose that catalyst particles with Nafion films fabricated from high-water-content formulations undergo a higher level of

138

electrochemical fragmentation, particularly at the beginning of electrolysis, generating higher coverages of smaller nanoparticles. It has been demonstrated that such fragmentation or reconstruction process of catalyst usually produces abundant undercoordinated sites near the surface, functioning as active sites for promoting C-C coupling to enhance the selectivity C_{2+} products. The reason for the enhanced activity on undercoordinated copper sites in CO_2 reduction is that they can provide a high degree of selectivity towards C-C coupling by facilitating the formation of a reactive intermediate, such as a *COOH species, which can then undergo further reactions to form C-C bonds.[150,161,162] In addition to promoting C-C coupling, undercoordinated copper sites can also facilitate the adsorption and activation of CO_2, which is typically a challenging step in the electrochemical reduction of CO_2. The undercoordinated copper sites can thus provide a high density of active sites for CO_2 adsorption, and can also stabilize reaction intermediates by lowering their energy barriers.[53,125,150,163]

6.6 Summary

In conclusion, we report that the Nafion/solvent formulations used for preparing CLs have a significant impact on the performance of electrochemical CO_2R on glassy carbon substrates in terms of activity, selectivity, and stability. By optimizing the Nafion/formulations, CuO NP catalysts with Nafion films achieve high selectivities of C_2H_4 (FE of 65%) and C_{2+} products (FE of 87%), with a robust durability of 200 h on glassy carbon substrates in CO_2-saturated 0.1 M $KHCO_3$ in H-cells. Remarkably, the CO_2R performance, particularly the production of C_{2+} products, progressively improves over 200 h due to the constant increase of active sites capable of C-C coupling, generated by the fragmentation of catalyst particles. In this scenario, the maximum selectivties of C_{2+} products and corresponding durability are hence expected to be further enhanced in longer durability tests.

These findings suggest a simple and effective approach to engineer CLs for highly selective and stable CO_2 electrolysis, which can be extended to other electrochemical applications as well. For instance, future research could be devoted to engineering the Nafion films of GDEs by modifying Nafion/solvent

formulations in flow type cells or MEAs. One of the major challenges impeding cost-effective large-scale CO_2 electrolysis is the degradation and deactivation of the electrocatalysts over time. This work therefore provides a promising solution to improve the durability of catalyst. If this strategy of modulating Nafion films is applied to GDEs, this could have a profound impact on advancing industrial CO_2 electrolysis.

Chapter 7. Conclusion and outlook

Conclusion

Electrochemical CO_2RR, powered by renewable electricity, is a potential solution for generating chemical feedstocks and fuels that can facilitate the shift towards a carbon-neutral future. The selective production of multicarbon products through reduction of CO_2 is of great interest because of the superior energy density and broader applications of these products. However, highly selective and stable production of multicarbon products in CO_2 electrolysis remains challenging. Nafion ionomer, composed of hydrophobic perfluorocarbon backbones and hydrophilic sulfonic acid side chains, is the most widely used additive for preparing CLs for electrochemical CO_2 reduction, but its impact on performance of CO_2 electrolysis remains poorly understood.

To address these issues, this work systematically examined the impact of catalyst ink formulations on Cu-catalyzed CO_2 electrolysis performance, catalyst structure, and local reaction environment, through the manipulation of Nafion content and solvent composition in catalyst inks. The research is organized into four main areas of focus: investigating the properties and structure of Nafion thin films fabricated using various Nafion/solvent formulations; examining the influence of Nafion/solvent formulations on Cu-catalyzed CO_2 electrolysis using carbon paper-based electrodes; designing Nafion/solvent formulations for the optimized production of multicarbon products in Cu-catalyzed CO_2 electrolysis on glassy carbon-based electrodes; and studying the underlying mechanisms behind the impact of Nafion/solvent formulations on Cu-catalyzed CO_2 electrolysis.

Specifically, we first demonstrated a comprehensive investigation of the impact of Nafion/solvent formulations on the structure and properties of casted Nafion thin films on Si substrates. The analysis of Nafion/solvent formulations used in recent literature revealed a lack of established guidelines and a tendency towards

empirical selection. To address this knowledge gap, we conducted a systematic examination of the influence of Nafion/solvent formulations, specifically Nafion weight content and water volume fraction, on the resulting Nafion films. Using a complementary set of characterization methods, we gained insight into how Nafion/solvent formulations impact the properties and structures of the films. Based on the derived understanding, we recommend that it is beneficial to use high-water-content formulations to prepare Nafion films that possess advantageous proton conductivity and better inner network connectivity.

On carbon paper substrates, we systematically investigated the role of the catalyst ink formulation on CO_2 electrolysis using commercial CuO nanoparticles as the model pre-catalyst. We determined that the presence of Nafion is essential for achieving stable product distributions due to its ability to stabilize the catalyst morphology under reaction conditions. Moreover, the Nafion content and solvent composition (water/alcohol fraction) regulate the internal structure of Nafion films, as well as the catalyst morphology, thereby significantly impacting CO_2 electrolysis performance, resulting in variations of C_{2+} product FE by >3×, with C_{2+} FE ranging from 17% to 54% on carbon paper substrates. Using a combination of ellipsometry and *in situ* Raman spectroscopy during CO_2 reduction, we demonstrated that such selectivity differences stem from changes to the local reaction microenvironment. In particular, the combination high water/alcohol ratios and low Nafion fractions in the catalyst ink results in stable and favorable microenvironments, increasing the local CO_2/H_2O concentration ratio and promoting high CO surface coverage to facilitate C_{2+} production in long-term CO_2 electrolysis. Therefore, this work provides insights into the critical role of Nafion binders and underlines the importance of optimizing Nafion/solvent formulations as a means of enhancing performance of electrochemical CO_2 reduction systems.

We further exploited our gained insights from studies on carbon paper substrates to prepare highly efficient working electrodes on glassy carbon substrates, thereby enhancing the production of multicarbon products on Cu catalysts. As for the case of carbon paper supports, we demonstrated that one can also modify the properties

of Nafion films on CuO-derived catalysts in order to tune the CO_2 reduction performance. With the optimal formulation, efficient mass transport and beneficial electrochemical fragmentation of catalyst particles can be realized, which leads to siginificantly enhanced production of C_{2+} products with a remarkably high Faradaic efficiencies for C_{2+} products of >87% for over 200 h. These findings again highlight the importance of engineering Nafion films to improve both electrochemical performance and stability, which can be widely extended to other electrochemical devices.

Outlook

Given the results presented in this work and the ubiquitous use of Nafion in the preparation of catalyst inks, we conclude that it is of great importance to also perform systematic studies of the effect of Nafion/solvent formulations on various types of catalysts, including inorganic, molecular, and single atom catalysts, for different electrochemical applications, including CO_2 electrolysis, water splitting, and fuel cells. In addition to the catalyst ink formulation, other factors in preparing CLs, such as the technique for deposition from catalyst inks, the mass loading of catalyst on substrate, the choice of substrate, and post-treatment of CLs, should be carefully investigated as well. These tasks inevitably require huge amounts of repetitive lab work, since so many interconnected variables are involved and each of them must be studied and optimized. This represents a considerable challenge in terms of experimental resources and time. In this respect, recent advances in high throughput experimentation for robotic synthesis, characterization, and testing provides a potential solution. Indeed, robots are increasingly crucial in various laboratory procedures, spanning from ordinary chemical analysis to DNA fingerprinting and drug development and testing. The reasons behind their utilization are manifold: in some cases, they perform monotonous tasks that decrease the need for human labor and ensure consistency. Moreover, they can lower risks to human operators by managing dangerous substances, prevent contamination of samples, and perform specific tasks much faster and more accurately than humans.[164]

Ideally, with thus-gained extensive experimental inputs and understandings of each influencing factor in the preparation of CLs, a database can be therefore built up. Machine learning (ML), as a frontier technology, is a form of modeling that relies on data rather than an understanding of the underlying physics to make predictions. This has resulted in groundbreaking advances in numerous fields over the past ten years, particularly in areas with access to vast amounts of data. In electrochemistry, ML models can be used to optimize experimental conditions, predict the properties of materials, and design new electrochemical devices. It can not only analyze literature to propose solutions for a novel problem but also perform multiple

simulations and autonomously identify relevant factors. For example, ML algorithms can be used to predict the behavior of electrolytes, electrode materials, and reaction products, allowing for more efficient and effective electrochemical reactions. Additionally, ML can help identify correlations between various parameters such as temperature, pH, and current density, providing insights into the underlying mechanisms of electrochemical processes.[165] Indeed, the data-driven approach of ML complements mechanistic approaches aimed at understanding atomic-scale processes. For example, rapid performance optimization can be achieved using high throughput experimentation and ML, with little understanding of underlying mechanisms, while the subsequent detailed studies can be directed at optimized systems and their dependencies. With this in mind, it is promising to combine high throughput experimentation together with ML to explore the large parameter space needed for optimizing electrocatalytic function. Through statistical design of experiments coupled with active learning approaches, the number of experiments required to reach an optimum can be significantly reduced (Figure 7.1).

Overall, taking advantage of these benefits, it would be possible to make data-driven predictions and develop rational approaches to electrode fabrication. Furthermore, a series of standard operating procedures can be established to guide researchers in the preparation of electrodes, which will contribute to the standardization of electrochemical measurements. The standardization of electrochemical measurements is essential to ensure accurate and reliable results, which can improve the quality and reproducibility of research work and lead to more effective applications of electrochemical technologies.

In parallel, detailed mechanistic studies using various *in situ* and/or *operando* techniques can be further performed on high performance systems to not only identify key dependencies but also inspire rational design of new catalytic systems.
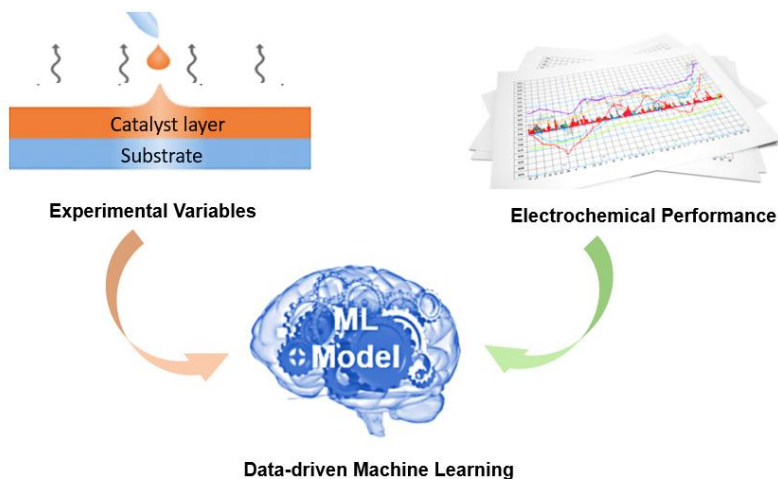
Figure 7.1 Schematic illustration of the application of machine learning (ML) in analyzing the effect of different experimental variables in electrode preparation on the electrochemical performance.

As a concluding remark, the development of CO_2 electrolysis is learning from other electrochemical technologies such as water electrolyzers, fuel cells and batteries. Extensive advances in this technology, which initiated from labs, are now on the way to being scaled up to commercial industries. One exceptional example is demonstrated by the company Twelve, which has realized the production of CO at the scale of kg per day using a proton exchange membrane (PEM) CO_2 electrolyzer. In the future scenario, as CO_2 technology potentially evolves into a primary approach to close the carbon cycle, we expect an eco-friendly energy system where more and more products are made from CO_2 collected from industrial emissions and, perhaps at a later stage, the atmosphere.

Appendix

A. Methods

A.1 Atomic force microscopy

Atomic Force Microscopy (AFM) is a powerful tool widely used to image and characterize surfaces at the nanoscale. It operates by using a sharp probe with a tip radius of ~10 nm to scan the surface of a sample in a controlled manner, providing topographical and other information about the sample.

The basic principle of AFM is the measurement of the forces between the probe and the surface of the sample. The probe is mounted on a cantilever, which is typically made of silicon, and is brought close to the sample surface. The forces between the probe and the sample surface cause a deflection of the cantilever, which is monitored with a laser beam reflected off the back of the cantilever onto a position-sensitive photodetector. By measuring the deflection of the cantilever as it scans over the surface of the sample, a map of the surface topography can be obtained (Figure A1a).

One of the most common modes of AFM operation is Tapping Mode, also known as intermittent contact mode. In this mode, the cantilever oscillates near its resonance frequency, and the tip intermittently taps the surface of the sample as it scans. The tapping motion minimizes the lateral forces between the tip and the sample, reducing the risk of damage to the sample and the tip.

The frequency of the tapping motion is typically a few hundred kHz, and the amplitude is small, typically in the range of a few nm. The amplitude and frequency of the tapping motion are monitored and controlled by a feedback loop that adjusts the height of the cantilever to maintain a constant amplitude of oscillation. The detected deflection signal provides information about the topography and other

properties of the surface, such as adhesion and stiffness. The phase of the cantilever oscillation relative to the excitation signal is also monitored, providing information about the viscoelastic properties of the sample (Figure A1b).
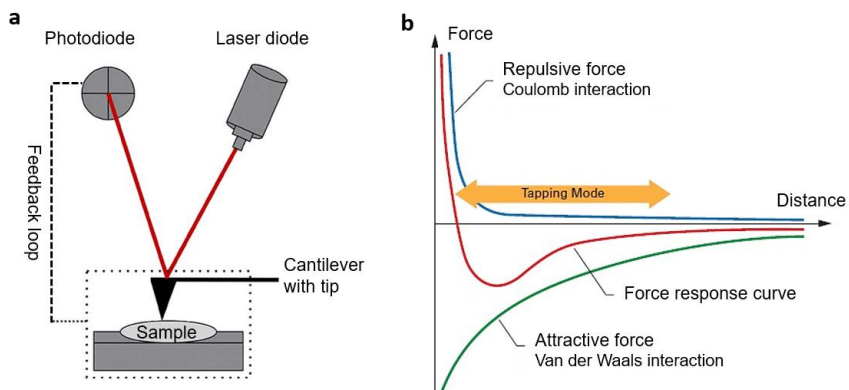

Figure A1 (a) Scheme of an AFM setup. (b) The force-distance curve, highlighting of the motion of an oscillating cantilever in tapping mode.

Tapping mode AFM is widely used for imaging, including soft materials such as organic and biological samples, because of its gentle interaction with the sample surface. Therefore, in this thesis we utilized the tapping mode of AFM (Bruker MultiMode 8 System, scan size of 1.0×1.0 µm) to characterize Nafion films without disturbing their structures.

A.2 X-ray scattering measurements

X-ray scattering is an important analytical technique used to study the structure and properties of materials at the atomic and nanoscale level. It involves shining a beam of X-rays on a sample and measuring the scattered X-rays as a function of angle or momentum transfer. X-ray scattering can provide information about the size, shape, orientation, and arrangement of atoms, molecules, and nanoscale structures in a material.

For common X-ray scattering measurements, a beam of X-rays is directed at a sample surface at a shallow angle of less than 1°, and the scattered radiation is probed with a two-dimensional detector as a function of the exit angle (α_f) and in-plane angle (α_ψ). The coordinate system is chosen to have the X-ray beam oriented parallel to the projection of the incident beam on the sample surface, with the z-axis oriented along the surface normal and the y-axis in the plane of the sample surface.

The wave vector transfer q, which is a measure of the scattering vector, is given by:

$$q = \frac{4\pi}{\lambda} \sin\left(\frac{\theta}{2}\right) \qquad\qquad \text{A.1}$$

where λ is the wavelength of the X-rays or neutrons, and θ is the scattering angle, which is related to the incident angle (α_i), the exit angle and the in-plane angle as:

$$\tan\theta = \sin(\alpha_f) \, / \, \left[\cos(\alpha_i) - \cos(\alpha_f) \, \cos(\psi)\right] \qquad \text{A.2}$$

The wave vector transfer q provides information about the size and shape of the nanoscale structures in the sample, as well as their orientation and distribution. By analyzing the scattering pattern as a function of q, valuable insights can be gained into the structure and properties of the sample.

One of the most common modes of X-ray scattering is Grazing Incidence Small-Angle X-ray Scattering (GISAXS), which is used to investigate thin films and surfaces (Fig. A2). In GISAXS, the X-ray beam is incident on the sample at a grazing angle, typically less than 0.5°. The grazing incidence geometry enhances the scattering from the surface layer of the sample, while minimizing the background scattering from the bulk. The scattered X-rays are detected at small angles, typically less than 5°, using a two-dimensional detector. The GISAXS pattern provides information about the surface morphology, roughness, and orientation of the scattering objects, such as nanoparticles or nanocrystalline domains. The shape of the scattering pattern can be analyzed using model-based simulations, such as the distorted wave Born approximation (DWBA) or the Parratt

algorithm, to extract quantitative information about the size and shape distribution of the scattering objects.
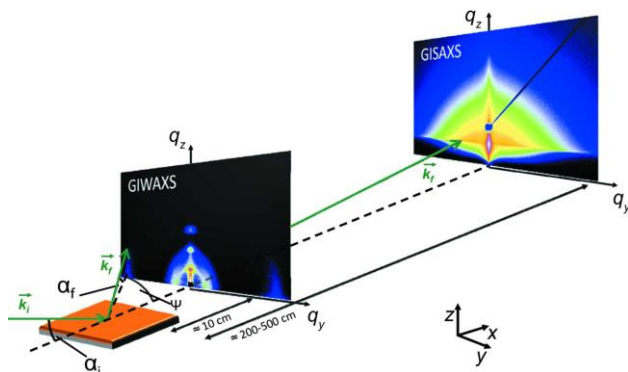

Figure A2 Illustration of the X-ray scattering principle in GISAXS and GIWAXS.[166]

The GISAXS measurements in this thesis were performed at the MiNaXS/P03 beamline of the PETRA III storage ring at DESY, Hamburg.[167] The photoenergy of the incident X-ray was 12.87 keV, corresponding to the wavelength of 0.96 Å. 2D GISAXS data were collected by PILATUS 300k detector (Dectris Ltd., Switzerland) with a pixel size of 172 × 172 µm^2. The incident angle, α_i, was set to 0.4° and the sample-to-detector distance (SDD) was 4090 ± 2 mm. Two beam-stops were used at the specular and the direct beam positions to shield the detector from the beam. 1D intensity distributions were extracted from the 2D GISAXS data using the Directly Programmable Data Analysis Kit software (DPDAK) v1.4.[168]

A.3 Spectroscopic ellipsometry

Spectroscopic ellipsometry is a powerful measurement technique that is non-destructive and non-contact, as it relies on optical methods. It can accurately determine the thickness and optical functions of each individual layer in a multilayer structure. The technique involves measuring the phase shift of light as it passes through a layer structure, and is highly sensitive, with the phase angle

measurement being independent of absolute light intensity. Spectral information on the sample can be acquired using either white light sources or monochromators.

Ellipsometry can also be used to measure ratios of complex Fresnel reflection coefficients, which are divided into amplitude and phase shift terms corresponding to ellipsometric angles Ψ and Δ, which are the two ellipsometric parameters that are determined experimentally. Ψ is the amplitude ratio of the p-polarized and s-polarized light waves reflected from the sample surface, while Δ is the phase difference between them. These two parameters provide information about the optical properties and thicknesses of thin films or multilayer structures. The values of Ψ and Δ are related to the refractive index and thickness of the layers through the Fresnel equation. Specifically, Ψ and Δ are related to the complex reflection coefficients of the sample, which can be modeled using the optical properties of the layers in the sample. By analyzing the changes in Ψ and Δ as a function of wavelength, it is possible to extract information about the optical properties of the layers, including their refractive indices, extinction coefficients, roughnesses, and thicknesses (Figure A3). Additionally, these parameters can be used to study the anisotropy and birefringence of materials. Ellipsometry is particularly useful for analyzing thin films and surfaces that have thicknesses in the range of a few nanometers to several micrometers.

The thicknesses of Nafion films on Si substrates were measured using a variable angle spectroscopic ellipsometer with a FLS-860 75 W Xe light source (J.A. Woollam, M-2000) in a high accuracy mode (angles: 45-85°, 10° step). The blank Si substrates were first characterized and the thickness of native oxide layer was measured to be ~2 nm. A multilayer general oscillator model (substrate Si-JAW; layer 1: SiO$_2$_JAW and layer 2: Cauchy Film), consisting of library functions for the Si substrate and native oxide, as well as a Cauchy model for Nafion, was built to fit the ellipsometry data and determine the as deposited Nafion film thickness. To determine the water content, the thickness of Nafion films was recorded in an *in situ* ellipsometry cell (fixed incidence angle: 70.23°) at different humidities. The humidity was controlled to be 0 and 100% by first purging the cell with N$_2$ (99.9999%, Linde) at a flow rate of 400 sccm for 1 h (0%), after which humidified

N₂ gas that was bubbled through a 25 °C water bath was fed to the cell for 1 h (100%). The change of thickness (ΔT) between 0% (T_0) and 100% (T_{100}) humidity was used to derive the swelling factor (α) and water content (μ) as descried in Section 4.5. Quantitative values were therefore obtained for the Nafion films prepared from 0.5 wt. % Nafion as a function of the solvent composition, as reported in Table 4.3.
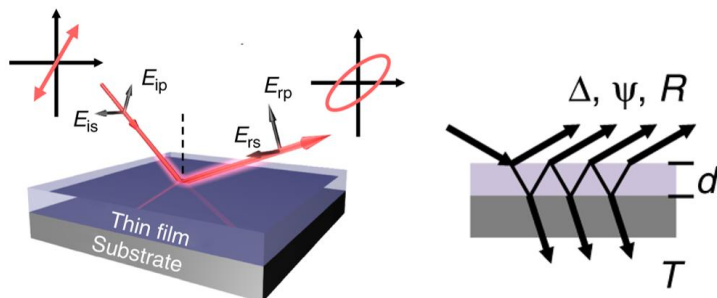

Figure A3 Schematic illustration of the principle of spectroscopy ellipsometry. The light beam, denoted as E_i, is directed at an angle onto a thin film whose refractive index, extinction coefficient, and thickness are unknown (n, κ, d). The thin film rests on a substrate whose optical properties are known. When the light beam enters the film, multiple beam interference occurs, as depicted in the inset. The reflection coefficients for the orthogonal polarization components, E_p and E_s, are unequal, resulting in an elliptically polarized reflected beam, denoted as E_r. The letters p and s are used to represent the polarizations with electric fields parallel and perpendicular to the plane of incidence, respectively. Reproduced from Ref.[169]

A.4 X-ray diffraction

X-ray diffraction (XRD) is a non-destructive analytical technique that is commonly used to determine the atomic and molecular structure of a material. In an XRD measurement, a beam of X-rays is directed onto a sample, and the scattered X-rays are collected on a detector. The sample is usually in the form of a powdered material, a thin film, or a single crystal. The incident X-rays interact with the electrons in the material, causing them to scatter in different directions. If the atomic planes of the crystal lattice are oriented in such a way that the angle of incidence

and the angle of reflection satisfy Bragg's Law, then constructive interference occurs, and the scattered X-rays reinforce each other. This leads to the formation of diffraction peaks on the detector.

This pattern of diffraction is based on Bragg's law, which states that the diffraction angle, θ, is related to the distance between crystal planes, d, and the wavelength of the X-rays, λ, by the equation:

$$n\lambda = 2d \sin \theta \qquad\qquad A.3$$

where *n* is the order of diffraction, as illustrated in Figure A4. This equation indicates that the spacing of the crystal planes determines the angle of diffraction, and the intensity of the diffracted X-rays depends on the orientation and number of atoms in the crystal structure.

The position and intensity of these peaks are characteristic of the crystal structure of the material, as well as its lattice parameters, such as the spacing between atomic planes. The XRD pattern can be analyzed to identify the crystal structure and to quantify the amount of each phase present in a mixture. Grazing Incidence X-ray Diffraction (GIXRD) is a surface sensitive diffraction technique that utilizes a small incident angle X-ray beam to limit penetration into the bulk material to avoid overlapping peaks from different depths of the sample. Thus, this technique is ideal for measuring thin films and multilayers on solid.

In this thesis, GI-XRD was performed using an X-ray diffractometer (SmartLab, Rigaku) equipped with a Cu anode with a scanning rate of 0.5° per min from 30° to 80°.
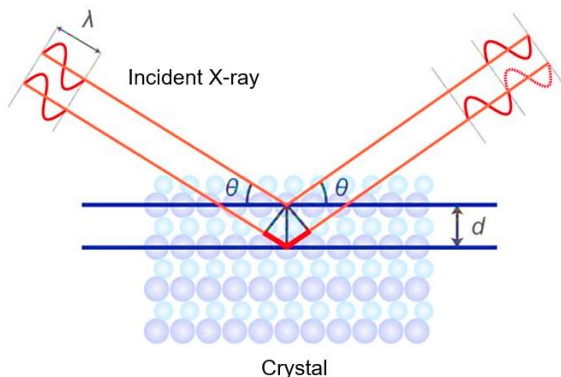
Figure A4 Schematic illustration of the principle of X-ray diffraction in a crystal.

A.5 Contact angle measurements

Contact angle measurements are used to quantify the wetting behavior of a liquid on a solid surface. The contact angle is defined as the angle formed between the solid surface and the tangent to the liquid surface at the point of contact (Figure A5). The contact angle can be expressed using the Young-Laplace equation as follows:

$$\cos\theta = (y_s - y_l)/y_i \hspace{3cm} \text{A.4}$$

where θ is the contact angle, y_s is the surface energy of the solid, y_l is the surface tension of the liquid, and y_i is the interfacial tension between the solid and liquid.

This equation shows that the contact angle is dependent on the properties of both the solid and the liquid, as well as the interfacial tension between them. A contact angle of 0° indicates complete wetting (hydrophilic), while a contact angle of 180° indicates complete non-wetting (hydrophobic).

Contact angle measurements can be performed using various techniques, for instance the sessile drop method. This method is widely used to measure the hydrophobicity of solid surface and typically involves capturing an image of the

liquid on the solid surface and analyzing the shape of the contact line to determine the contact angle.

The measurement of water contact angles in this thesis was performed using the "sessile drop" method with the Contact Angle system OCA (DataPhysics Instruments). This method involves placing a small droplet of water (1 µL) onto the surface of catalyst layers and measuring the angle formed between the liquid-solid interface and the tangent line drawn at the droplet's edge.
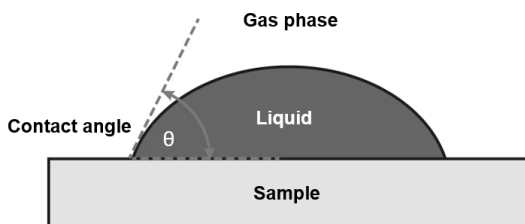

Figure A5 Schematic definition of the contact angle θ of a type of liquid on the solid sample surface.

A.6 Electrochemical techniques

Electrochemical techniques are widely used to study the behavior of electroactive species, which are species that undergo a change in oxidation state during a redox reaction. These techniques provide information on the kinetics, thermodynamics, and mechanism of electrochemical reactions.

Cyclic voltammetry (CV) is a technique that involves applying a ramped potential as an input. During the forward scan, a positive ramp potential with a positive slope is provided, followed by a voltage switch after the first half-cycle. This is then followed by a negative ramp, which reverses the nature of the cyclic voltammogram for the subsequent half cycle. The purpose of this technique is to observe the system's behavior as it strives to achieve equilibrium through redox reactions. The cyclic voltammogram follows a cyclic pattern where the system attempts to return to the same position where it started. By analyzing the CV curve, valuable

information can be obtained about the material and its properties, such as its capacitive nature. Additionally, the behavior of the system can be determined, whether it is reversible, irreversible, or quasi-reversible. This analysis allows for important conclusions to be drawn regarding the system's changes and behavior throughout the experiment. The CV experiment can be carried out with one cycle or multiple potential cycles. The resulting voltammogram is a plot of current versus applied electrochemical potential that provides information on the redox potential, electron transfer kinetics, and concentration of the electroactive species.

Chronopotentiometry (CP) is a technique that involves applying a constant current to an electrochemical cell while monitoring the resulting potential. Initially, an electrode is subjected to an applied current, leading to a change in its potential. This change is recorded over time and plotted, resulting in the chronopotentiometric response. The application of current can be done in four different ways: using a stepwise constant current, a linearly increasing current, current switching (reversal), or in a cyclic manner. Each of these methods generates distinct responses based on the varying input.

Chronopotentiometry is utilized for characterizing electrode reactions. Prior to the application of the input current, the analyte's concentration is uniform between the electrode surface and the bulk solution, and the potential recorded during this period is known as the open circuit potential. Once the input current is applied, the analyte gets reduced at the electrode surface to sustain the current, leading to a decrease in its concentration at the electrode surface. This establishes a concentration gradient for the analyte between the electrode surface and the bulk solution, causing the analyte molecules to diffuse towards the electrode surface along this gradient. The potential observed in this scenario is known as the redox potential and can be determined using the Nernst equation. Due to the changing concentration, the potential also varies with time, resulting in a change in the slope of the potential versus time response. If the concentration of the analyte at the electrode surface reaches zero, the electron transfer reaction fails to support the applied input current, causing the redox potential to shift to other electron transfer reactions involving a different analyte present in the solution. If no other analyte is

available, the second electron transfer reaction involves the reduction of the electrolyte, leading to a significant change in the potential value. Thus, the output waveform of the potential versus time exhibits a sudden potential change at the beginning and end, along with a gradual shift in the central part of the curve. The resulting potentiogram is normally a plot of potential versus time that provides information on the kinetics of the electrochemical reaction, including the rate of electrodeposition/dissolution and the diffusion coefficient of the species involved.

Chronoamperometry (CA) is a technique that involves applying a constant potential to an electrochemical cell while monitoring the resulting current. In chronoamperometry, the input potential is varied, and the corresponding current variation is recorded as a function of time. CA follows Cottrell's equation, which is derived from Fick's second law of diffusion. The equation is expressed as:

$$i(t) = nFAC\sqrt{\frac{D}{\pi t}} = \frac{k}{\sqrt{t}} \qquad\qquad A.5$$

Here, *n*, *F*, *A*, *C*, *D*, *t*, and i represent the number of electrons, Faraday constant, surface area of the electrode, concentration of the analyte (electrochemically active species), diffusion coefficient, time, and current, respectively. Cottrell's equation helps determine the diffusion coefficient (*D*) of the electroactive species available on the electrode's surface. It predicts the current variation over time, known as the chronoamperometric response, when a potential step is applied under conditions of a large overpotential. It should be noted that the Cottrell equation is applicable only when the current is diffusion-controlled, and the solution must be unstirred. Since CA follows the Cottrell equation, it exhibits a characteristic current-time response. The behavior of the curve is known as Cottrellian behavior, where the current is inversely proportional to the square root of time. At the beginning of CA, a step input potential is applied to the working electrode, increasing its potential from a point where no faradaic reaction occurs to a point where the surface concentration of the electroactive species reaches zero. This results in a decaying current profile. The chronoamperometric response (*i-t* curve) reflects the variation in the concentration gradient in the vicinity of the electrode surface. The resulting amperogram is a plot of current versus time that provides information on the

kinetics of the electrochemical reaction, including the rate of electrodeposition/dissolution and the diffusion coefficient of the species involved.

In order to perform these electrochemical techniques, specialized instrumentation is required, including a potentiostat or galvanostat, which is used to control the potential/current applied to the electrochemical cell, and a data acquisition system, which is used to monitor the resulting current/potential. The data obtained from these electrochemical techniques can be analyzed using mathematical models to obtain quantitative information on the electrochemical system under study.

For electrochemical measurements in this thesis, an airtight H-type cell (C023-2, Gauss Union) with two compartments separated by a Nafion 115 membrane was used for CO_2 electrolysis. Electrochemical measurements were performed using a potentiostat (Biologic VSP-300) connected in a three-electrode configuration, with Ag/AgCl (3 M KCl) electrode (Gauss Union) and Pt foil (99.99%, Gauss Union), as reference electrode and counter electrode, respectively. The working electrode was installed at a fixed distance of 15 mm from the reference electrode. $KHCO_3$ (99.95%, Sigma-Aldrich) aqueous solutions (0.5 M for carbon paper-based electrodes and 0.1 M for glassy carbon-based electrodes) was used as electrolyte and was continuously purged with CO_2 gas (99.999%, Linde) for 1 h to ensure CO_2 saturation prior to CO_2 electrolysis measurements. During measurements, both cathodic and anodic compartments were continuously purged with CO_2 gas and the flow rate of CO_2 gas in the cathodic compartment was maintained at 40 sccm using a mass flow controller (MKS). The gas outlet of the cathodic compartment was connected to a gas chromatograph (SRI 8610C, see details below) for online analysis of gas product every 20 min. Chronopotentiometry tests were carried out at a constant current density (-50 mA/cm^2 for carbon paper-based electrodes and -12.8 mA/cm^2 for glassy carbon-based electrodes) for 5 h, and chronoamperometry tests were performed at different fixed potentials for 1 h each.

For measurements of the electric double layer capacitance, corresponding CLs were prepared on planar glassy carbon electrodes (catalyst loading of 0.255 mg cm^{-2}) and ESCAs were obtained by recording cyclic voltammograms in Ar pre-purged 0.1 M K_2SO_4 aqueous solution at different scanning rates (10, 25, 50, 100,

200 mV s^{-1}) within a potential range where no redox reactions take place. The series resistance (R), measured by electrochemical impedance spectroscopy and the current interrupt method, was compensated by 85%. All potentials were converted to the RHE scale using the equation below, in which i was the current recorded during the course of CO_2 electrolysis:

$$E\,(vs.\,RHE)\;=\;E_{Ag/AgCl}\;+\;0.85\,R\,i\;+\;0.207\,V\;+\;0.059\,pH \qquad A.6$$

For long term chronopotentiometric CO_2 electrolysis of 200 h (5 cycles) on glassy carbon-based electrodes, the electrolytes in both cathodic and anodic compartments were refreshed after each cycle of ~40 h. Notably, to minimize the influence of oxygen in air on the CLs, the working electrode was quickly transferred into degassed electrolytes when refreshing electrolytes. Afterwards, both compartments were purged with CO_2 gas for 1 h before starting the next cycle of durability test.

A.7 Gas chromatography

Gas chromatography (GC) is a widely used analytical technique for separating and analyzing complex mixtures of volatile compounds. It is based on the principle of partitioning a mixture of compounds between a stationary phase and a mobile phase. The stationary phase is a material that is coated onto the inner surface of a long, narrow tube called a column, while the mobile phase is a gas that is used to carry the sample through the column.

As the sample moves through the column, it interacts with the stationary phase based on the differences in their physical and chemical properties, such as boiling points, polarity, and molecular weight. This results in the separation of the sample components, which can then be detected and quantified using a detector at the end of the column (Figure A6).
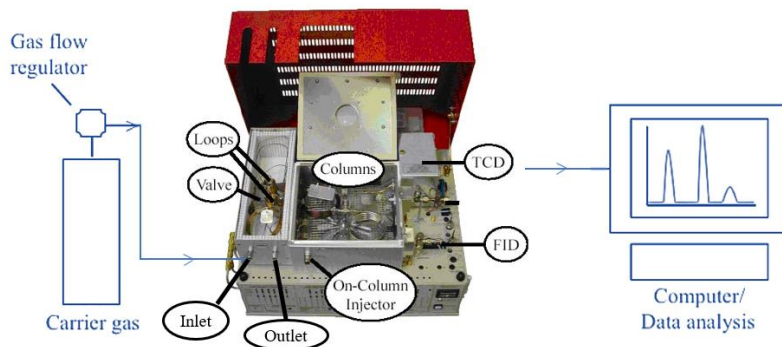
Figure A6 Scheme of the GC testing system.

There are several types of detectors that can be used in GC, including flame ionization detectors (FID), thermal conductivity detectors (TCD), electron capture detectors (ECD), and mass spectrometry (MS) detectors. Each detector type has its own advantages and limitations, and the choice of detector depends on the specific application and the properties of the sample being analyzed.

GC is widely used in analyzing the products, particularly gaseous products, in electrochemical CO_2 reduction. Typically, with an established calibration curve, the quantity of gaseous products can be readily determined. When connected to an electrochemical cell with continuous gas flow, real-time gaseous products formed in CO_2 electrolysis can be monitored by automatic sampling.

In this thesis, gaseous products, including H_2, CO, CH_4, C_2H_4 and C_2H_6, were analyzed using an online GC (SRI 8610C) equipped with both a thermal conductivity detector and a flame ionization detector using Ar (99.9999%, Linde) as carrier gas. The GC calibration was performed by sampling the diluted calibration gas with known concentrations for each component (i.e., H_2, CO, CH_4, C_2H_4 and C_2H_6.) An automagical GC sampling program was used to run measurements every 20 min at a gas flow rate of 40 sccm. The GC sample loop is of a fixed volume of 1 mL. The gas flow rate at the outlet was also measured to be 40 sccm. Faradaic efficiencies (FE) were calculated as follows:

$$FE = \frac{nFC}{Q} \qquad\qquad \text{A.7}$$

where n is the number of electrons required for production of one single specific product, F is the Faraday constant of 96,485 C mol^{-1}, C is the measured amount of product molecules in mols, and Q is the total number of electrons consumed by electrolysis.

A.8 Hydrogen nuclear magnetic resonance spectroscopy

Hydrogen nuclear magnetic resonance (^{1}H NMR) spectroscopy is a widely used analytical technique that provides information on the number, type, and environment of hydrogen atoms in a molecule. ^{1}H NMR spectroscopy is based on the principle that hydrogen atoms have a nuclear spin, which gives them a magnetic moment. In ^{1}H NMR measurements, a sample is subjected to a strong magnetic field and then irradiated with radiofrequency (rf) radiation. The protons present in the sample align themselves either parallel or anti-parallel with the magnetic field, resulting in a difference in their spin states, which corresponds to a resonance energy. Upon exposure to a specific frequency of rf radiation, the lower-energy protons can switch their alignment, and it is this exact energy released by the protons that is detected in this technique as they return to their lower energy state. (Figure A7). Each hydrogen atom in the molecule produces a signal with a unique chemical shift, allowing one to determine the number and positions of different types of hydrogen atoms in the molecule. Additionally, the intensity of the signals can be used to determine the relative quantity of each molecule in the sample with corresponding established calibration curves.
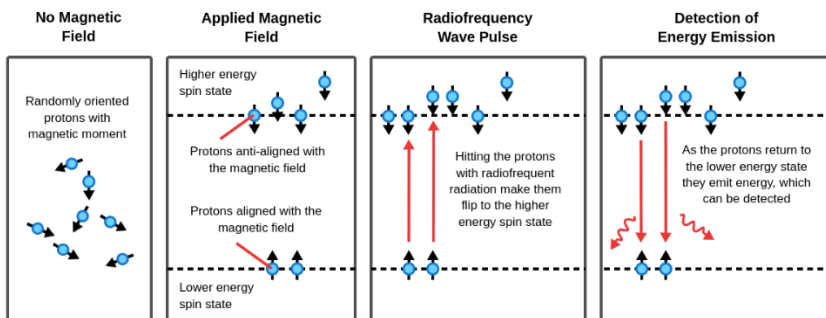
Figure A7 Scheme of the working principle of ^{1}H NMR spectroscopy. Adapted from an open source from django-wiki.

The frequency of the signal is recorded as a spectrum, with the chemical shift of the signal representing the environment of the hydrogen atoms in the molecule. The chemical shift (δ) is measured in parts per million (ppm) and is influenced by the electron density surrounding the hydrogen nucleus, as well as by the neighboring atoms in the molecule. The chemical shift of a hydrogen atom is expressed as a deviation of the measured NMR frequency (v) relative to the frequency (v_{ref}) of a reference compound (such as tetramethylsilane, TMS), which is assigned a chemical shift of 0 ppm, as defined below.

$$\delta \ (\text{ppm}) = \ 10^6 \times \frac{v - v_{ref}}{v_{ref}} \qquad\qquad \text{A.8}$$

Liquid products in this thesis, including methanol, formate, acetate, ethanol and n-propanol were determined by analysis of the cathodic electrolyte after CO_2 electrolysis using ^{1}H NMR spectroscopy (AV 500 HD). For this, 400 µL of electrolyte was mixed with 100 µL of D_2O containing 200 ppm dimethyl sulfoxide (DMSO) as the internal standard. The concentration of each liquid product was then quantified according to established calibration curves. The calibration curves were plotted based on the normalized intensities of NMR signals (referenced to DMSO) of spiked molecules with different concentrations (8, 40, 80, 160, 320 ppm) as shown in Appendix Table B1 and Figure B5.

A.9 Raman spectroscopy

Raman spectroscopy is an analytical technique that uses scattered light to measure the vibrational modes of a sample. When light interacts with a molecule (or material), it induces a polarization of the molecular electron cloud, leaving the molecule in a higher energy state. This interaction between the photon and molecule is known as the virtual state of the molecule and is short-lived. The vast majority of scattering events are elastic (Rayleigh scattering), where the energy of the molecule is unchanged, and the scattered photon has the same energy and wavelength as the incident photon.

In a much rarer event (approximately 1 in 10 million photons), Raman scattering occurs, where there is an inelastic scattering process with a transfer of energy between the molecule and scattered photon. The scattered photon loses energy if the molecule gains energy during scattering (Stokes Raman scattering) and gains energy if the molecule loses energy during relaxation (anti-Stokes Raman scattering). While quantum mechanically, Stokes and anti-Stokes are equally likely processes, the Boltzmann distribution of molecules in the ground vibrational level makes Stokes Raman scattering statistically more probable at room temperature. Thus, the Stokes Raman scattering is more intense than the anti-Stokes Raman scattering (Figure A8).

As the Raman scattered wavelength is dependent on the excitation light wavelength, the Raman scattered light spectrum is converted to a Raman shift away from the excitation wavelength, expressed as the wavenumber of the Raman shift in cm^{-1} as follows:

$$\Delta v \text{ (cm}^{-1}) = \left(\frac{1}{\lambda_0 \text{(nm)}} - \frac{1}{\lambda_1 \text{(nm)}} \right) \text{x} \frac{10^7 \text{ nm}}{\text{cm}} \qquad\qquad \text{A.9}$$

where λ_0 is the excitation laser wavelength in nm, and λ_1 is the Raman scattered light wavelength in nm.
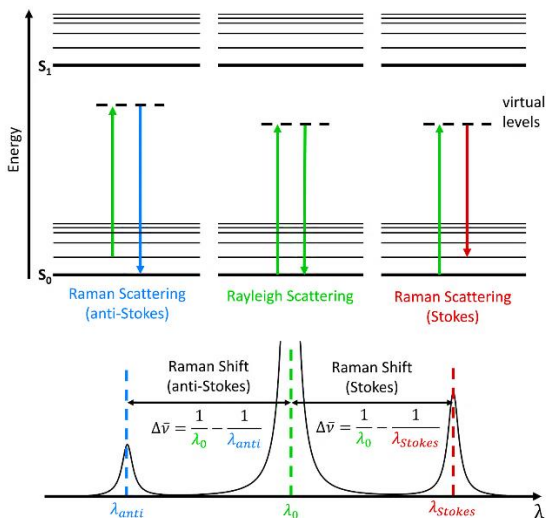
Figure A8 Jablonski Diagram showing the origin of Rayleigh, Stokes and Anti-Stokes Raman Scattering.[170]

In situ Raman spectroscopy has emerged as a powerful tool in the investigation of CO_2 electrolysis, where it allows for the real-time monitoring of intermediates and products of the reaction. For example, the formation of CO is a key step in CO_2 reduction and can be detected by the characteristic Raman peak around 2060 cm^{-1}.[140,143] The formation of other products such as formate, oxalate, and methane can also be detected by their unique Raman signatures. Additionally, in situ Raman spectroscopy can be used to track the evolution of reaction products over time and to study the effects of different operating conditions on the reaction kinetics.

In situ Raman spectroscopy has also been used in combination with other techniques such as electrochemistry and mass spectrometry to provide a more comprehensive understanding of CO_2 electrolysis. For example, *in situ* Raman spectroscopy can be used to identify the formation of reaction intermediates, while electrochemistry can be used to measure the current density and potential of the electrode. Thus, *in situ* Raman spectroscopy is used as a valuable tool in this thesis for the investigation of CO_2 electrolysis, providing real-time monitoring of reaction

intermediates and products and allowing for a better understanding of the reaction mechanism and kinetics.

In situ Raman spectra during CO_2 electrolysis were acquired using a Renishaw InVia Raman microscope equipped with a 785 nm excitation laser and a Nikon N40X-NIR water-dipping objective lens. The laser power was kept below 1.5 mW to protect the sample from laser damage. A previously described custom electrochemical Raman cell was used for collecting Raman spectra under operational conditions.[143] A grating with 1200 lines/mm was used for maximum efficiency. This limits the wavenumber coverage of each single TR-SERS collection to approximately 300 cm^{-1}. The collection time was 0.8 s per spectrum for the quick scan in the low-wavenumber window (for the CV data), which results in a final collection interval of 1 s between subsequent spectra due to the additional time required for opening/closing of the mechanical shutter and signal readout. During chronoamperometry measurements, full spectra covering the range between 100 to 2200 cm^{-1} were collected, which required acquisition of six individual spectra within different wavenumber windows, resulting in a total time of ~18 s. The potential was applied through an Autolab PGSTAT 101 potentiostat in a three-electrode configuration, with a leak-free Ag/AgCl reference electrode (eDaQ), a glassy carbon counter electrode, and carbon paper-based electrodes prepared with different Nafion/solvent formulations (CuO powder loading of 0.5 mg cm^{-1}) as working electrodes.

A.10 Inductively coupled plasma mass spectrometry

Inductively coupled plasma mass spectrometry (ICP-MS) is a powerful analytical technique used for the detection and quantification of trace elements and isotopes in a wide range of samples. The ICP is generated by introducing a sample into a stream of argon gas and then subjecting the gas to a high-frequency electromagnetic field. This ionizes the argon atoms and creates a plasma of positively charged ions and free electrons. The high temperature and energy of the plasma cause the sample to dissociate and ionize, resulting in the formation of a range of positively charged ions. These ions are then introduced into the mass

spectrometer where they are separated based on their mass-to-charge ratios. The ions are accelerated through a series of electric and magnetic fields, which cause them to travel on a curved path. The radius of curvature of the ion path is dependent on the mass-to-charge ratio of the ion, allowing for the separation of ions with different masses. The separated ions are then detected by a detector, typically a Faraday cup or a secondary electron multiplier. The number of ions detected is proportional to the abundance of the ion in the sample, allowing for the quantification of trace elements and isotopes if appropriate calibration measurements are also performed (Figure A9).

In this thesis, ICP-MS is used to detect the concentration of copper ions in electrolyte of carbonate buffer solutions. It should be noted that our sample cannot be directly subjected to the ICP-MS tests due to the relatively high pH value and the high salt concentration in the electrolyte. Therefore, collected samples were prepared by diluting the electrolyte 5 times with super-pure nitric acid.
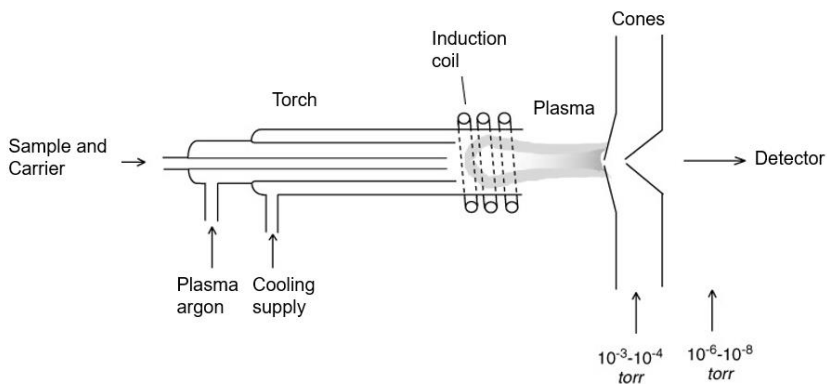

Figure A9 Scheme of the working principle of ICP-MS.

A.11 Preparation of Nafion films and working electrodes

Nafion solutions were prepared by adding specific volumes of commercial Nafion ionomer dispersions (5 wt.% in alcohol-water mixture, 45% water + 55% propanol and methanol, Sigma-Aldrich) into absolute isopropanol or isopropanol-water

solutions with defined mixing ratios. For example, to prepare the film from 50 vol.% H_2O and 0.005 wt.% Nafion, 2 μL of the as-received Nafion solution was dispersed into a mixture of 999 μL deionized water and 999 μL isopropanol, followed by 30 min of ultrasonic treatment. The prepared solutions were then spin coated on Si wafers (p-type, resistivity: <0.005 Ohm-cm, thickness: 525 μm) and dried for at least 2 h at room temperature before measurements. Similarly, catalyst inks were prepared by dispersing 10 mg of CuO powder (~50 nm, Sigma-Aldrich) into the previously prepared Nafion solutions, after which they were sonicated for 60 min in a water bath. During sonication, the water temperature was kept below 30 °C.

To prepare working electrodes on carbon paper substrates, catalyst inks were deposited on carbon paper (AvCarb P75T, Fuel Cell Store, USA). The mass loading of CuO catalyst was 0.5 mg cm^{-2} on the 1.0 × 2.0 cm^2 carbon paper substrate (working area of 1.0 × 1.0 cm^2), which was obtained by drop-casting 100 μL (20 μL, 5 times) of catalyst ink. After drop casting, the electrodes were baked at 80 °C in air for 10 min on a heating plate. The investigated Nafion weight ratios were 0 wt.%, 0.005 wt.%, 0.025 wt.%, 0.05 wt.%, 0.125 wt.%, 0.25 wt.% and 0.5 wt.%, and water contents were 0 vol.%, 25 vol.%, 50 vol.% and 75 vol.%. The samples are denoted by their water content-Nafion weight ratio (e.g., 50 vol.%-0.005 wt.%) throughout this work.

To prepare working electrodes on glassy carbon substrates, catalyst inks were deposited on glassy carbon substrates (diameter of 5 mm, Gauss Union). The mass loading of CuO catalyst was fixed at 0.255 mg cm^{-2} (working area of 0.196 cm^2), which was obtained by drop-casting 10 μL (2 μL, 5 times) of catalyst slurries. After drop casting, the electrodes were further baked at 80 °C in air for 10 min on a heating plate. The Nafion weight ratios studied in this work include 0 wt.%, 0.005 wt.%, 0.025 wt.%, 0.05 wt.%, 0.125 wt.%, 0.25 wt.% and 0.5 wt.%, and investigated water contents include 0 vol.%, 25 vol.%, 50 vol.% and 75 vol.%. These prepared Nafion films and catalyst layers are denoted by the format of water content-Nafion weight ratio (e.g., 75 vol.%-0.25 wt.%).

A.12 Basic Characterization

The morphologies of Nafion films and catalyst layers (CLs) were characterized by scanning electron microscopy (SEM, Zeiss NVision40 FIB-SEM) and atomic force microscopy (AFM, Bruker MultiMode 8 System, tapping mode, scan size of 1.0 × 1.0 μm). X-ray photoelectron spectroscopy (XPS) data were obtained using a Specs FlexPS system equipped with a monochromatized Al Kα source (hν = 1486.6 eV) and a Phoibos 150 analyzer coupled to a 2D CCD detector. XPS binding energies were calibrated using the C 1s core level position of 284.8 eV as a reference.
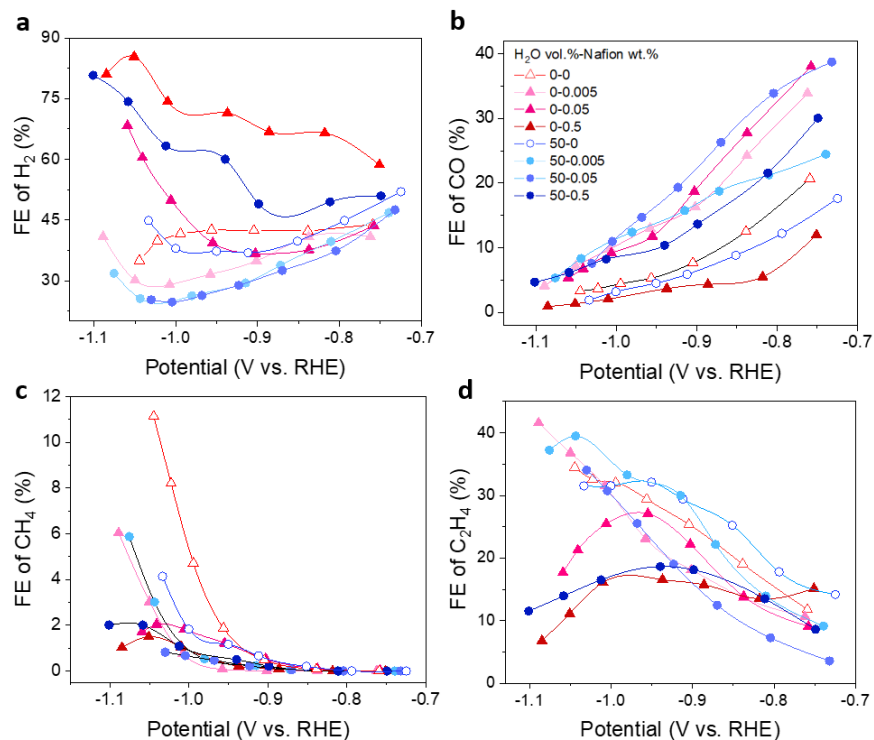
B. Supporting Information

Figure B1 Effect of Nafion/solvent formulations on potential-dependent CO_2 electrolysis. Catalytic performance of electrodes prepared by different Nafion/solvent formulations evaluated in terms of Faradaic efficiency (FE) of H_2 (**a**), CO (**b**), CH_4 (**c**) and C_2H_4 (**d**).
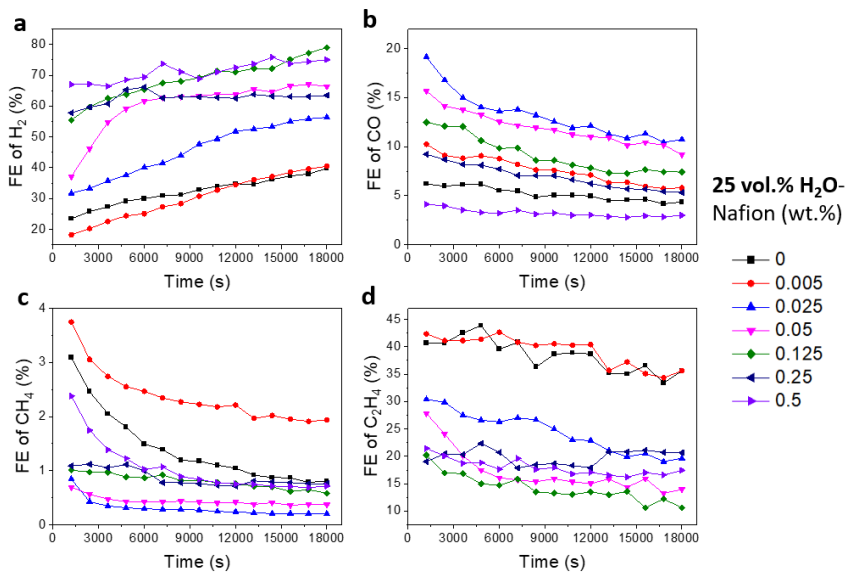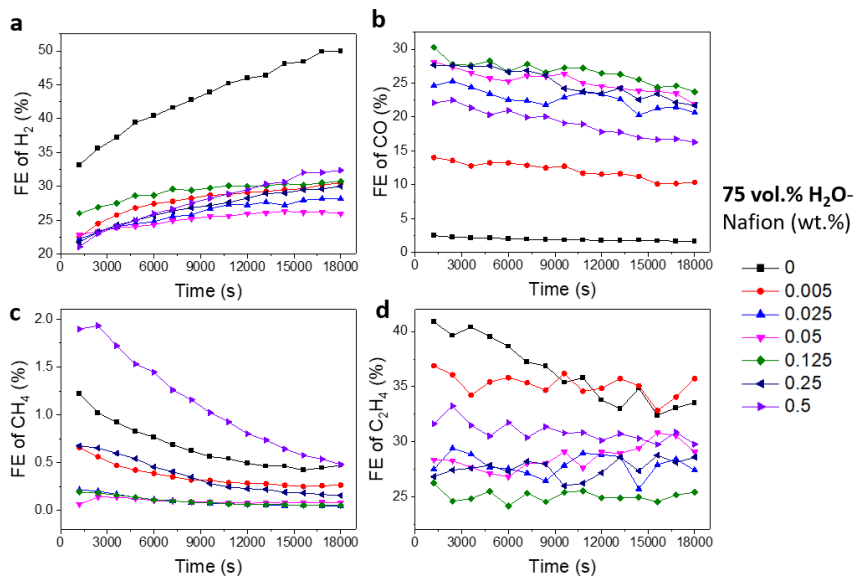
Figure B2 Effect of Nafion/solvent formulations on stability of chronopotentiometric CO_2 electrolysis at -50.0 mA cm^{-2} on carbon paper-based electrodes in CO_2 saturated 0.5 M $KHCO_3$. Dynamic changes of FEs of gaseous products: namely H_2 (**a**), CO (**b**), CH_4 (**c**), and C_2H_4 (**d**), over 5 h.

Figure B3 Effect of Nafion/solvent formulations on stability of chronopotentiometric CO_2 electrolysis at -50.0 mA cm^{-2} on carbon paper-based electrodes in CO_2 saturated 0.5 M $KHCO_3$. Dynamic changes of FEs of gaseous products: namely H_2 (**a**), CO (**b**), CH_4 (**c**), and C_2H_4 (**d**), over 5 h.
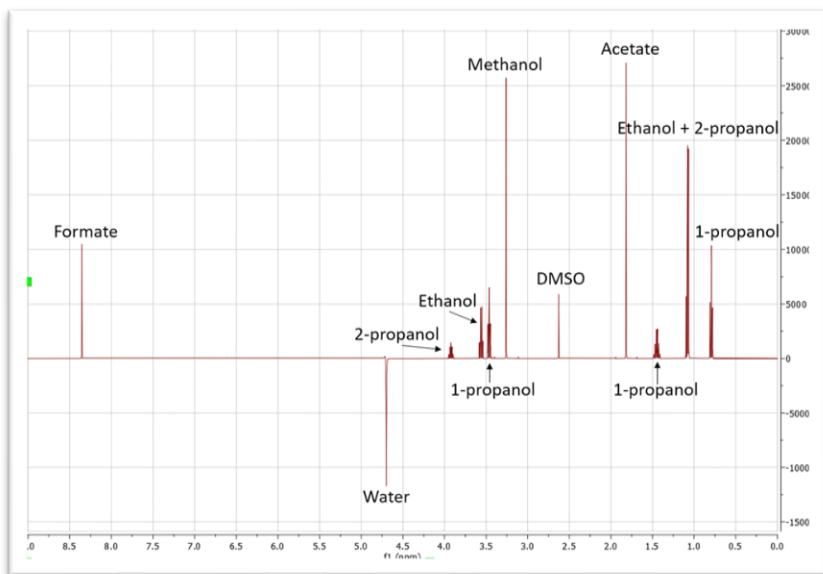
Figure B4 Example liquid product analysis using ^{1}H NMR, showing raw ^{1}H NMR data.

Table B1 A table of all liquid products detected by ^{1}H NMR in this work.

| Number	Structure	Formula	Name	Chemical shift (ppm)				Density g/mL	MW g/mol
1	OH	C3H8O	1-propanol	0.81 (t)	1.46 (sextet)	2.14 (s)	3.48 (t)	0.803	60.09
2	OH	C3H8O	2-propanol	1.16 (d)		3.86 (septet)		0.786	60.09
3		C3H6O	Propionaldehyde	0.805 (t)	0.97 (t)	1.48 (dt)			
4	OH	C2H6O	Ethanol	1.10 (t)	3.57 (q)			0.789	46.07
5	OH	C2H4O2	Acetic acid	1.83 (s)				1.05	60.052
6.1	CH3CH(OH)2	C2H4O	Acetaldehyde	1.21 (d)					
6.2		C2H4O	Acetaldehyde		2.12 (d)				
7		C3H6O	Acetone	2.15 (s)					
8	H—C—OH	CH4O	Methanol	3.28 (s)	3.64 (q)			0.792	32.04
9	HO O	C2H4O2	Glycolaldehyde	3.44 (d)					
10	HO OH	C2H6O	Ethylene glycol	3.59 (s)					
11	OH	C3H6O	Allyl alcohol	4.03 (dt)	5.107	5.204	5.935		
12	H OH	CH2O2	Formic acid	8.37 (s)				1.22	46.03

173
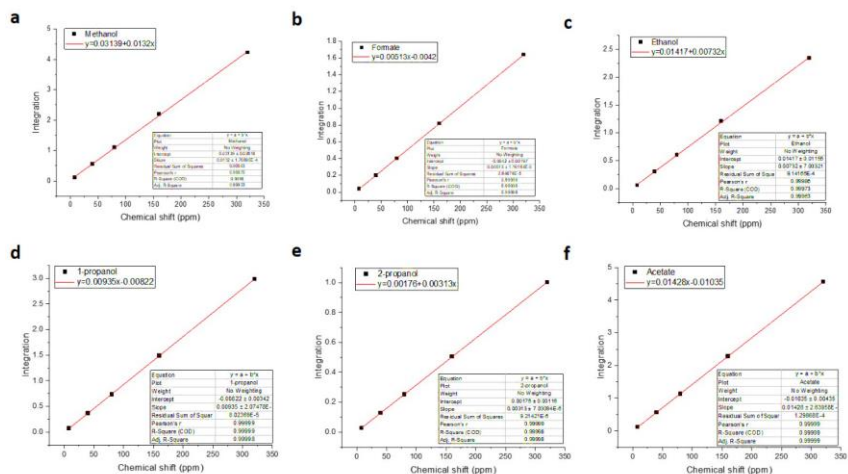
Figure B5 Calibration curves of 6 major liquid products determined by ^{1}H NMR. **a**, methanol. **b**, formate. **c**, ethanol. **d**, 1-propanol. **e**, 2-propanol. **f**, acetate. The Faradaic efficiency (FE) of n-propanol was calculated by adding up the FEs of both 1-propanol and 2-propanol in this work.
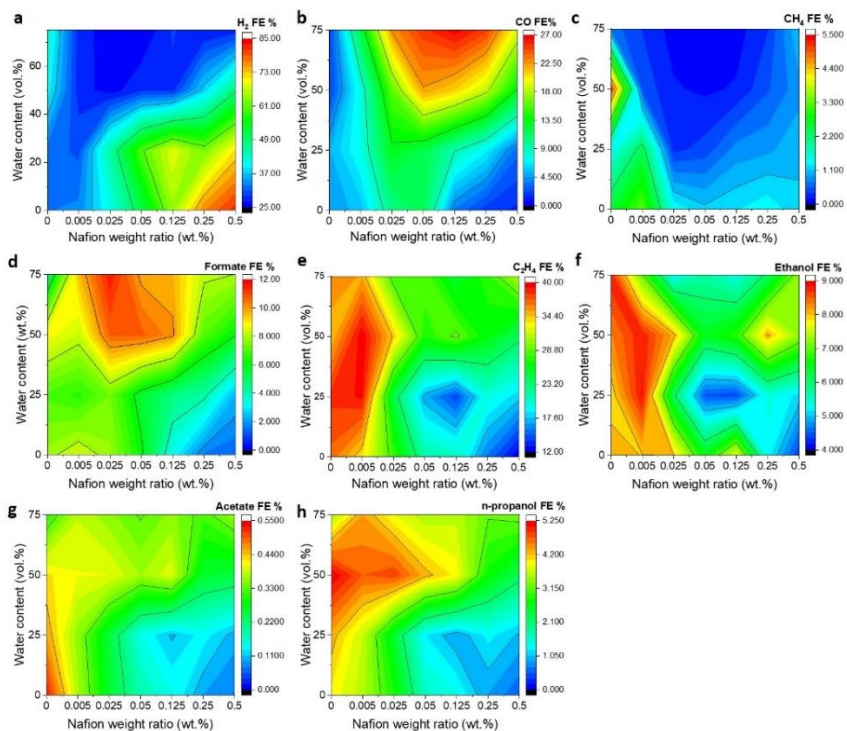
Figure B6 Effect of Nafion/solvent formulations on selectivity of chronopotentiometric CO_2 electrolysis at -50.0 mA cm^{-2} in CO_2 saturated 0.5 M $KHCO_3$. Heatmaps of Faradaic efficiency of H_2 (**a**), CO (**b**), CH_4 (**c**), formate (**d**), C_2H_4 (**e**), ethanol (**f**), acetate (**g**), and n-propanol (**h**).
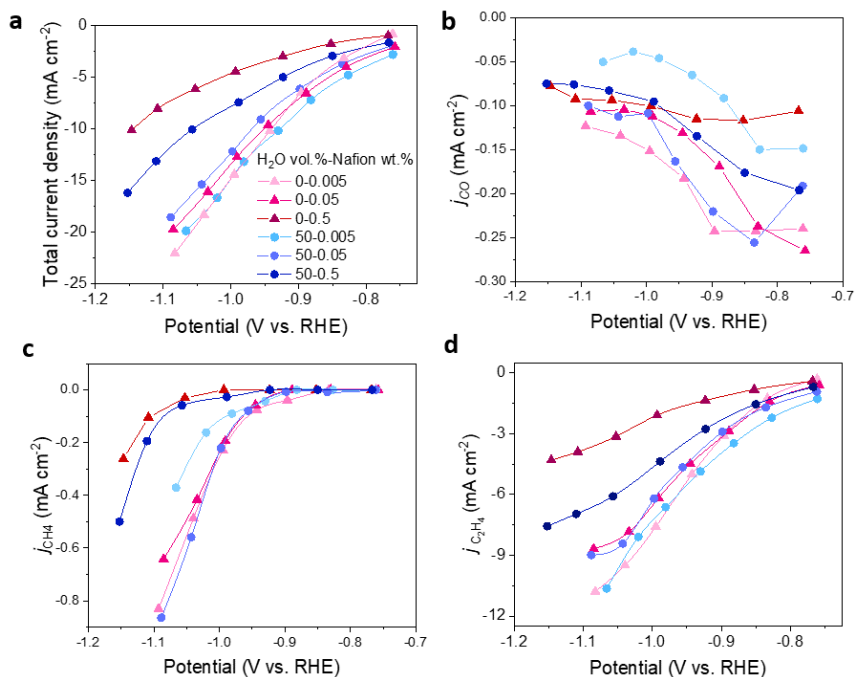
175

Figure B7 Effect of Nafion/solvent formulations on potential-dependent CO_2 electrolysis on glassy carbon-based electrodes. Catalytic performance of electrodes prepared by different Nafion/solvent formulations evaluated in terms of total current density (**a**) and partial current densities of CO (**b**), CH_4 (**c**) and C_2H_4 (**d**).
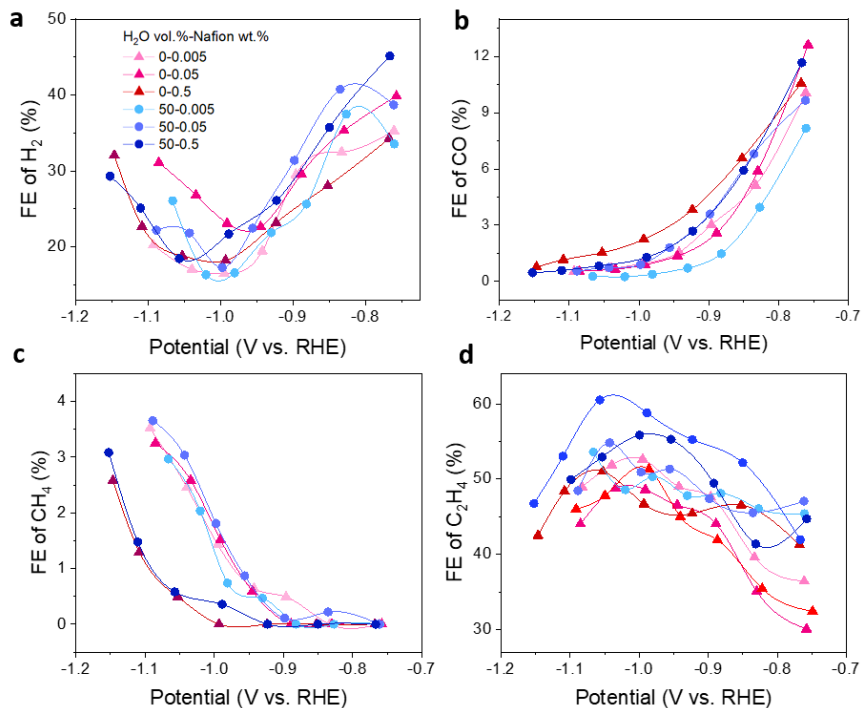
Figure B8 Effect of Nafion/solvent formulations on potential-dependent CO_2 electrolysis on glassy carbon-based electrodes. Catalytic performance of electrodes prepared by different Nafion/solvent formulations evaluated in terms of Faradaic efficiency (FE) of H_2 (**a**), CO (**b**), CH_4 (**c**) and C_2H_4 (**d**).
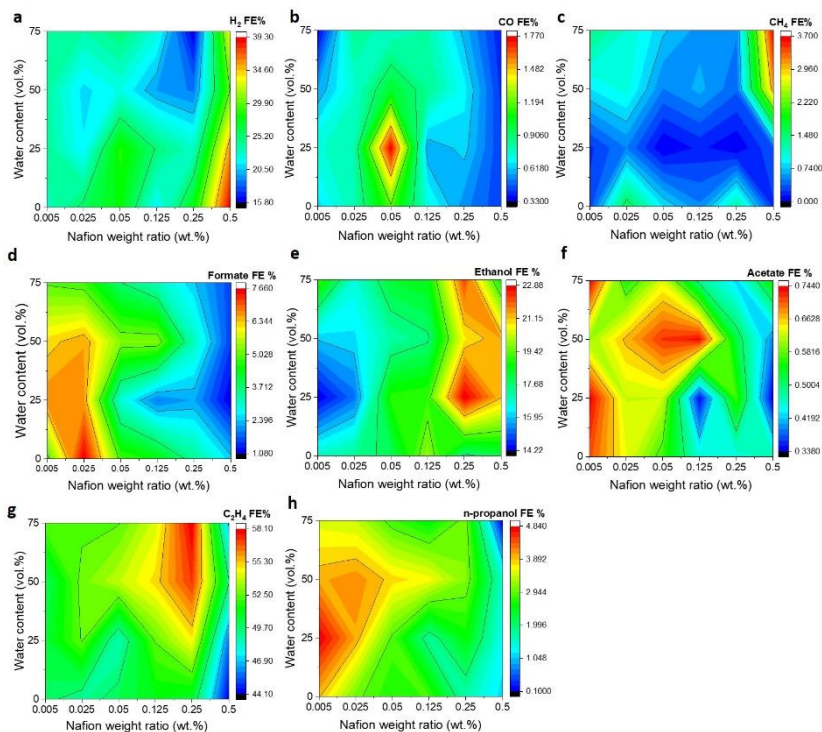
Figure B9 Effect of Nafion/solvent formulations on selectivity of chronopotentiometric CO_2 electrolysis on glassy carbon based-electrodes at -12.8 mA cm^{-2} in CO_2 saturated 0.5 M $KHCO_3$. Heatmaps of Faradaic efficiency of H_2 (**a**), CO (**b**), CH_4 (**c**), formate (**d**), ethanol (**e**), acetate (**f**), C_2H_4 (**g**), and n-propanol (**h**).

Glossary

List of symbols

nm	nanometer
Å	angstrom
wt %	weight percent
K_a	acid dissociation constant
T	temperature
μ_w	chemical potential gradient of water
α_T	transport coefficient
N_w	molar water flux
λ	hydration number
D_d	dynamic diffusivity
D	diffusion coefficient
κ	conductivity
L	length
A	area
R	resistance
φ_w	water volume fraction
P_i	permeability of a gas
S_i	solubility coefficien
pm	picometre
ppm	parts per million
E^o	standard reduction potential
R	gas constant
Q	reaction quotient
ΔG	Gibbs free energy
C_1	single carbon

C_{2+}	multicarbon
q	magnitude of the scattering vector
θ	scattering angle
μ	water content
α	swelling factor
Δ*T*	thickness
ρ	density

List of abbreviations

PFSA	perfluorinated sulfonic-acid
TFE	tetrafluoroethylene
PEM	proton exchange membrane
PTFE	polytetrafluoroethylene
EW	equivalent weight
MW	Molecular weight
SAXS	small-angle X-ray scattering
NMF	N-methylformamide
NMP	N-Methyl-2-pyrrolidone
SANS	small angle neutron scattering
NMR	nuclear magnetic resonance
DLS	dynamic light scattering
Cryo-TEM	Cryo-transmission electron microscopy
GIXS	grazing incident X-ray scattering
GISAXS	grazing-incidence small-angle X-ray scattering
GIWAXS	grazing-incidence wide-angle X-ray scattering
IPA	isopropanol
2D	two dimensional
MEA	membrane electrode assembly
AFM	atomic force microscopy
QCM	quartz Crystal Microbalance
QENS	quasi-elastic neutron scattering
DVS	dynamic-vapor-sorption
WU	water uptake
IEC	ion-exchange capacity
RH	relative humidity
DSC	differential scanning calorimetry
GC	gas chromatography
CO_2RR	CO_2 reduction reaction

OER	oxygen evolution reaction
HER	hydrogen evolution reaction
SHE	standard hydrogen electrode
RHE	reversible hydrogen electrode
vs.	vesus
GDE	gas-diffusion electrode
GDL	gas diffusion layer
EM	electronic modification
NCI	non-covalent interaction
LC	local concentration
FE	Faradaic efficiency
PrOH	n-propanol
CPET	concerted proton-electron transfer
CIBH	catalyst-Nafion ionomer bulk heterojunction
CL	catalyst layer
XRD	X ray diffraction
SEM	scanning electron microscopy
XPS	X ray photoelectron spectroscopy
ECSA	electrochemically active surface area
CV	cyclic voltammetry
EIS	electrochemical impedance spectroscopy
GC	gas chromatography
EtOH	ethanol
OCP	open circuit potential
NP	nanoparticle
FTIR	Fourier-transform infrared spectroscopy
TCD	total current density
ICP-MS	inductively coupled plasma mass spectrometry

Bibliography

[1]   D. L. Phil, H. Christopher, H. Drew, S. A. Jaffer, T. F. Jaramillo, E. H. Sargent, *Science* **2019**, *364 (6438)*, eaav3506.

[2]   O. S. Bushuyev, P. De Luna, C. T. Dinh, L. Tao, G. Saur, J. van de Lagemaat, S. O. Kelley, E. H. Sargent, *Joule* **2018**, *2*, 825–832.

[3]   J. Kim, W. Guo, H. Kim, S. Choe, S. Y. Kim, S. H. Ahn, *ACS Sustain. Chem. Eng.* **2022**, *10*, 14092–14111.

[4]   S. Nitopi, E. Bertheussen, S. B. Scott, X. Liu, A. K. Engstfeld, S. Horch, B. Seger, I. E. L. Stephens, K. Chan, C. Hahn, J. K. Nørskov, T. F. Jaramillo, I. Chorkendorff, *Chem. Rev.* **2019**, *119*, 7610–7672.

[5]   International Energy Agency, *Global Energy Review 2021 (IEA)*, Paris, **2021**.

[6]   F. Shen, M. Wang, L. Huang, F. Qian, *J. Ind. Eng. Chem.* **2021**, *93*, 394–406.

[7]   H. Shin, K. U. Hansen, F. Jiao, *Nat. Sustain.* **2021**, *4*, 911–919.

[8]   M. Jouny, W. Luc, F. Jiao, *Ind. Eng. Chem. Res.* **2018**, *57*, 2165–2177.

[9]   S. Wang, T. Kou, S. E. Baker, E. B. Duoss, Y. Li, *Mater. Today Nano* **2020**, *12*, 100096.

[10]   K. P. Kuhl, E. R. Cave, D. N. Abram, T. F. Jaramillo, *Energy Environ. Sci.* **2012**, *5*, 7050–7059.

[11]   A. Kusoglu, A. Z. Weber, *Chem. Rev.* **2017**, *117*, 987–1104.

[12]   C. Kim, J. C. Bui, X. Luo, J. K. Cooper, A. Kusoglu, A. Z. Weber, A. T. Bell, *Nat. Energy* **2021**, *6*, 1026–1034.

[13] A. Yasunishi, F. Yoshida, *J. Chem. Eng. Data* **1979**, *24*, 11–14.

[14] F. Lucile, P. Cézac, F. Contamine, J.-P. Serin, D. Houssin, P. Arpentinier, *J. Chem. Eng. Data* **2012**, *57*, 784–789.

[15] R. Pang, K. Teramura, H. Asakura, S. Hosokawa, T. Tanaka, *ACS Appl. Energy Mater.* **2019**, *2*, 5397–5405.

[16] Q. Gong, P. Ding, M. Xu, X. Zhu, M. Wang, J. Deng, Q. Ma, N. Han, Y. Zhu, J. Lu, Z. Feng, Y. Li, W. Zhou, Y. Li, *Nat. Commun.* **2019**, *10*, 2807.

[17] S. Liang, N. Altaf, L. Huang, Y. Gao, Q. Wang, *J. CO$_2$ Util.* **2020**, *35*, 90–105.

[18] K. Malik, S. Singh, S. Basu, A. Verma, *WIREs Energy Environ.* **2017**, *6*, e244.

[19] D. Pabsch, C. Held, G. Sadowski, *J. Chem. Eng. Data* **2020**, *65*, 5768–5777.

[20] T. Burdyny, W. A. Smith, *Energy Environ. Sci.* **2019**, *12*, 1442–1453.

[21] F. P. García de Arquer, C.-T. Dinh, A. Ozden, J. Wicks, C. McCallum, A. R. Kirmani, D.-H. Nam, C. Gabardo, A. Seifitokaldani, X. Wang, Y. C. Li, F. Li, J. Edwards, L. J. Richter, S. J. Thorpe, D. Sinton, E. H. Sargent, *Science* **2020**, *367*, 661–666.

[22] X. Zhang, S.-X. Guo, K. A. Gandionco, A. M. Bond, J. Zhang, *Mater. Today Adv.* **2020**, *7*, 100074.

[23] G. L. de Gregorio, T. Burdyny, A. Loiudice, P. Iyengar, W. A. Smith, R. Buonsanti, *ACS Catal.* **2020**, *10*, 4854–4862.

[24] W. Luo, X. Nie, M. J. Janik, A. Asthagiri, *ACS Catal.* **2016**, *6*, 219–229.

[25] Y. C. Tan, K. B. Lee, H. Song, J. Oh, *Joule* **2020**, *4*, 1104–1120.

[26]   A. Xu, N. Govindarajan, G. Kastlunger, S. Vijay, K. Chan, *Acc. Chem. Res.* **2022**, *55*, 495–503.

[27]   D. Gao, R. M. Arán-Ais, H. S. Jeon, B. Roldan Cuenya, *Nat. Catal.* **2019**, *2*, 198–210.

[28]   L. Fan, C. Xia, F. Yang, J. Wang, H. Wang, Y. Lu, *Sci. Adv.* **2022**, *6*, eaay3111.

[29]   Z. Sun, Y. Hu, D. Zhou, M. Sun, S. Wang, W. Chen, *ACS Energy Lett.* **2021**, *6*, 3992–4022.

[30]   A. Vasileff, X. Zhi, C. Xu, L. Ge, Y. Jiao, Y. Zheng, S.-Z. Qiao, *ACS Catal.* **2019**, *9*, 9411–9417.

[31]   J. A. Gauthier, J. H. Stenlid, F. Abild-Pedersen, M. Head-Gordon, A. T. Bell, *ACS Energy Lett.* **2021**, *6*, 3252–3260.

[32]   A. Wagner, C. D. Sahm, E. Reisner, *Nat. Catal.* **2020**, *3*, 775–786.

[33]   Y. Hori, K. Kikuchi, S. Suzuki, *Chem. Lett.* **1985**, *14*, 1695–1698.

[34]   C. G. Vayenas, R. E. White, M. E. Gamboa-Aldeco, *Mod. Asp. Electrochem. 42*, Springer Science & Business Media, **2008**.

[35]   S. Vijay, W. Ju, S. Brückner, S.-C. Tsang, P. Strasser, K. Chan, *Nat. Catal.* **2021**, *4*, 1024–1031.

[36]   R. Kortlever, J. Shen, K. J. P. Schouten, F. Calle-Vallejo, M. T. M. Koper, *J. Phys. Chem. Lett.* **2015**, *6*, 4073–4082.

[37]   P. Sabatier, *Berichte der deutschen chemischen Gesellschaft* **1911**, *44*, 1984–2001.

[38]   A. Bagger, W. Ju, A. S. Varela, P. Strasser, J. Rossmeisl, *ChemPhysChem* **2017**, *18*, 3266–3273.

[39]   Y. Hori, A. Murata, Y. Yoshinami, *J. Chem. Soc. Faraday Trans.* **1991**, *87*, 125–128.

[40]   H. Ooka, M. C. Figueiredo, M. T. M. Koper, *Langmuir* **2017**, *33*, 9307–9313.

[41]   Y. Y. Birdja, E. Pérez-Gallent, M. C. Figueiredo, A. J. Göttle, F. Calle-Vallejo, M. T. M. Koper, *Nat. Energy* **2019**, *4*, 732–745.

[42]   J. B. Greenblatt, D. J. Miller, J. W. Ager, F. A. Houle, I. D. Sharp, *Joule* **2018**, *2*, 381–420.

[43]   H. Mistry, A. S. Varela, S. Kühl, P. Strasser, B. R. Cuenya, *Nat. Rev. Mater.* **2016**, *1*, 16009.

[44]   Y. Liu, Y. Zhang, K. Cheng, X. Quan, X. Fan, Y. Su, S. Chen, H. Zhao, Y. Zhang, H. Yu, M. R. Hoffmann, *Angew. Chem. Int. Ed.* **2017**, *56*, 15474.

[45]   X. Chen, J. Chen, N. M. Alghoraibi, D. A. Henckel, R. Zhang, U. O. Nwabara, K. E. Madsen, P. J. A. Kenis, S. C. Zimmerman, A. A. Gewirth, *Nat. Catal.* **2021**, *4*, 20–27.

[46]   H. Xu, D. Rebollar, H. He, L. Chong, Y. Liu, C. Liu, C.-J. Sun, T. Li, J. v Muntean, R. E. Winans, D.-J. Liu, T. Xu, *Nat. Energy* **2020**, *5*, 623–632.

[47]   Y. Chen, Z. Fan, J. Wang, C. Ling, W. Niu, Z. Huang, G. Liu, B. Chen, Z. Lai, X. Liu, B. Li, Y. Zong, L. Gu, J. Wang, X. Wang, H. Zhang, *J. Am. Chem. Soc.* **2020**, *142*, 12760–12766.

[48]   D.-H. Nam, O. S. Bushuyev, J. Li, P. de Luna, A. Seifitokaldani, C.-T. Dinh, F. P. García de Arquer, Y. Wang, Z. Liang, A. H. Proppe, C. S. Tan, P. Todorović, O. Shekhah, C. M. Gabardo, J. W. Jo, J. Choi, M.-J. Choi, S.-W. Baek, J. Kim, D. Sinton, S. O. Kelley, M. Eddaoudi, E. H. Sargent, *J. Am. Chem. Soc.* **2018**, *140*, 11378–11386.

[49]   M. G. Kibria, C.-T. Dinh, A. Seifitokaldani, P. de Luna, T. Burdyny, R. Quintero-Bermudez, M. B. Ross, O. S. Bushuyev, F. P. García de Arquer, P. Yang, D. Sinton, E. H. Sargent, *Adv. Mater.* **2018**, *30*, 1804867.

[50]   D. Wakerley, S. Lamaison, F. Ozanam, N. Menguy, D. Mercier, P. Marcus, M. Fontecave, V. Mougel, *Nat. Mater.* **2019**, *18*, 1222–1227.

[51]   D. Cao-Thang, B. Thomas, K. M. Golam, S. Ali, G. C. M, G. de A. F. Pelayo, K. Amirreza, E. J. P, D. L. Phil, B. O. S, Z. Chengqin, Q.-B. Rafael, P. Yuanjie, S. David, E. H. Sargent, *Science* **2018**, *360*, 783–787.

[52]   F. Li, A. Thevenon, A. Rosas-Hernández, Z. Wang, Y. Li, C. M. Gabardo, A. Ozden, C. T. Dinh, J. Li, Y. Wang, J. P. Edwards, Y. Xu, C. McCallum, L. Tao, Z.-Q. Liang, M. Luo, X. Wang, H. Li, C. P. O'Brien, C.-S. Tan, D.-H. Nam, R. Quintero-Bermudez, T.-T. Zhuang, Y. C. Li, Z. Han, R. D. Britt, D. Sinton, T. Agapie, J. C. Peters, E. H. Sargent, *Nature* **2020**, *577*, 509–513.

[53]   C. Choi, S. Kwon, T. Cheng, M. Xu, P. Tieu, C. Lee, J. Cai, H. M. Lee, X. Pan, X. Duan, W. A. Goddard, Y. Huang, *Nat. Catal.* **2020**, *3*, 804–812.

[54]   M. Zhong, K. Tran, Y. Min, C. Wang, Z. Wang, C.-T. Dinh, P. de Luna, Z. Yu, A. S. Rasouli, P. Brodersen, S. Sun, O. Voznyy, C.-S. Tan, M. Askerka, F. Che, M. Liu, A. Seifitokaldani, Y. Pang, S.-C. Lo, A. Ip, Z. Ulissi, E. H. Sargent, *Nature* **2020**, *581*, 178–183.

[55]   B. Zhang, J. Zhang, M. Hua, Q. Wan, Z. Su, X. Tan, L. Liu, F. Zhang, G. Chen, D. Tan, X. Cheng, B. Han, L. Zheng, G. Mo, *J. Am. Chem. Soc.* **2020**, *142*, 13606–13613.

[56]   M. Luo, Z. Wang, Y. C. Li, J. Li, F. Li, Y. Lum, D.-H. Nam, B. Chen, J. Wicks, A. Xu, T. Zhuang, W. R. Leow, X. Wang, C.-T. Dinh, Y. Wang, Y. Wang, D. Sinton, E. H. Sargent, *Nat. Commun.* **2019**, *10*, 5814.

[57]   X. Su, Y. Sun, L. Jin, L. Zhang, Y. Yang, P. Kerns, B. Liu, S. Li, J. He, *Appl. Catal. B* **2020**, *269*, 118800.

[58]   N. Han, P. Ding, L. He, Y. Li, Y. Li, *Adv. Energy Mater.* **2020**, *10*, 1902338.

[59]   X. Zhang, Y. Wang, M. Gu, M. Wang, Z. Zhang, W. Pan, Z. Jiang, H. Zheng, M. Lucero, H. Wang, G. E. Sterbinsky, Q. Ma, Y.-G. Wang, Z. Feng, J. Li, H. Dai, Y. Liang, *Nat. Energy* **2020**, *5*, 684–692.

[60]   Q. Gong, P. Ding, M. Xu, X. Zhu, M. Wang, J. Deng, Q. Ma, N. Han, Y. Zhu, J. Lu, Z. Feng, Y. Li, W. Zhou, Y. Li, *Nat. Commun.* **2019**, *10*, 2807.

[61]   P. Ding, J. Zhang, N. Han, Y. Zhou, L. Jia, Y. Li, *J. Mater. Chem. A* **2020**, *8*, 12385–12390.

[62]   H. bin Yang, S.-F. Hung, S. Liu, K. Yuan, S. Miao, L. Zhang, X. Huang, H.-Y. Wang, W. Cai, R. Chen, J. Gao, X. Yang, W. Chen, Y. Huang, H. M. Chen, C. M. Li, T. Zhang, B. Liu, *Nat. Energy* **2018**, *3*, 140–147.

[63]   Y. Y. Birdja, E. Pérez-Gallent, M. C. Figueiredo, A. J. Göttle, F. Calle-Vallejo, M. T. M. Koper, *Nat. Energy* **2019**, *4*, 732–745.

[64]   Q. Zhu, X. Sun, D. Yang, J. Ma, X. Kang, L. Zheng, J. Zhang, Z. Wu, B. Han, *Nat. Commun.* **2019**, *10*, 3851.

[65]   Z. Sun, Y. Hu, D. Zhou, M. Sun, S. Wang, W. Chen, *ACS Energy Lett.* **2021**, *6*, 3992–4022.

[66]   K. Rossi, R. Buonsanti, *Acc. Chem. Res.* **2022**, *55*, 629–637.

[67]   H. Mistry, A. S. Varela, S. Kühl, P. Strasser, B. R. Cuenya, *Nat. Rev. Mater.* **2016**, *1*, 16009.

[68]   M. Zhong, K. Tran, Y. Min, C. Wang, Z. Wang, C.-T. Dinh, P. de Luna, Z. Yu, A. S. Rasouli, P. Brodersen, S. Sun, O. Voznyy, C.-S. Tan, M. Askerka, F. Che, M. Liu, A. Seifitokaldani, Y. Pang, S.-C. Lo, A. Ip, Z. Ulissi, E. H. Sargent, *Nature* **2020**, *581*, 178–183.

[69]   C. W. Lee, K. D. Yang, D.-H. Nam, J. H. Jang, N. H. Cho, S. W. Im, K. T. Nam, *Adv. Mater.* **2018**, *30*, 1704717.

[70] H. J. Erick, L. Fengwang, O. Adnan, S. R. Armin, G. de A. F. Pelayo, L. Shijie, Z. Shuzhen, L. Mingchuan, W. Xue, L. Yanwei, X. Yi, B. Koen, M. R. Kai, D. Cao-Thang, S. David, E. H. Sargent, *Science* **2021**, *372*, 1074–1078.

[71] X. Zhang, J. Li, Y.-Y. Li, Y. Jung, Y. Kuang, G. Zhu, Y. Liang, H. Dai, *J. Am. Chem. Soc.* **2021**, *143*, 3245–3255.

[72] T. Burdyny, W. A. Smith, *Energy Environ. Sci.* **2019**, *12*, 1442–1453.

[73] T. H. M. Pham, J. Zhang, M. Li, T.-H. Shen, Y. Ko, V. Tileli, W. Luo, A. Züttel, *Adv. Energy Mater.* **2022**, *12*, 2103663.

[74] Q. Chang, J. H. Lee, Y. Liu, Z. Xie, S. Hwang, N. S. Marinkovic, A.-H. A. Park, S. Kattel, J. G. Chen, *JACS Au* **2022**, *2*, 214–222.

[75] M. Y. Kariduraganavar, R. K. Nagarale, A. A. Kittur, S. S. Kulkarni, *Desalination* **2006**, *197*, 225–246.

[76] C. Heitner-Wirguin, *J. Memb. Sci.* **1996**, *120*, 1–33.

[77] C. R. Martin, T. A. Rhoades, J. A. Ferguson, *Anal. Chem.* **1982**, *54*, 1639–1641.

[78] C. Welch, A. Labouriau, R. Hjelm, B. Orler, C. Johnston, Y. S. Kim, *ACS Macro. Lett.* **2012**, *1*, 1403–1407.

[79] G. Gebel, B. Loppinet, H. Hara, E. Hirasawa, *J. Phys. Chem. B* **1997**, *101*, 3980–3987.

[80] Y. S. Kim, C. F. Welch, R. P. Hjelm, N. H. Mack, A. Labouriau, E. B. Orler, *Macromolecules* **2015**, *48*, 2161–2172.

[81] S. A. Berlinger, B. D. McCloskey, A. Z. Weber, *J. Phys. Chem. B* **2018**, *122*, 7790–7796.

[82] E. Szajdzinska-Pietek, S. Schlick, A. Plonka, *Langmuir* **1994**, *10*, 1101–1109.

[83]   S. Jiang, K.-Q. Xia, G. Xu, *Macromolecules* **2001**, *34*, 7783–7788.

[84]   S. J. Sondheimer, N. J. Bunce, M. E. Lemke, C. A. Fyfe, *Macromolecules* **1986**, *19*, 339–343.

[85]   H. Liu, L. Ney, N. Zamel, X. Li, *Appl. Sci.* **2022**, *12*, 3776.

[86]   S. A. Berlinger, P. J. Dudenas, A. Bird, X. Chen, G. Freychet, B. D. McCloskey, A. Kusoglu, A. Z. Weber, *ACS Appl. Polym. Mater.* **2020**, *2*, 5824–5834.

[87]   X. Gao, K. Yamamoto, T. Hirai, N. Ohta, T. Uchiyama, T. Watanabe, H. Imai, S. Sugawara, K. Shinohara, Y. Uchimoto, *ACS Omega* **2021**, *6*, 14130–14137.

[88]   A. Kusoglu, T. J. Dursch, A. Z. Weber, *Adv. Funct. Mater.* **2016**, *26*, 4961–4975.

[89]   A. Kusoglu, D. Kushner, D. K. Paul, K. Karan, M. A. Hickner, A. Z. Weber, *Adv. Funct. Mater.* **2014**, *24*, 4763–4774.

[90]   D. I. Kushner, A. Kusoglu, N. J. Podraza, M. A. Hickner, *Adv. Funct. Mater.* **2019**, *29*, 1902699.

[91]   M. A. Modestino, D. K. Paul, S. Dishari, S. A. Petrina, F. I. Allen, M. A. Hickner, K. Karan, R. A. Segalman, A. Z. Weber, *Macromolecules* **2013**, *46*, 867–873.

[92]   Y. Fan, D. Tongren, C. J. Cornelius, *Eur. Polym. J.* **2014**, *50*, 271–278.

[93]   H. F. M. Mohamed, Y. Kobayashi, C. S. Kuroda, A. Ohira, *J. Phys. Chem. B* **2009**, *113*, 2247–2252.

[94]   E. Planes, H.-D. Nguyen, T. K. Ly Nguyen, N. Charvin, L. Flandin, S. Lyonnard, C. Iojoiu, *ACS Appl. Energy Mater.* **2021**, *4*, 5809–5820.

[95]   B. MacMillan, A. R. Sharp, R. L. Armstrong, *Polymer* **1999**, *40*, 2481–2485.

[96]   J. R. Bontha, P. N. Pintauro, *Chem. Eng. Sci.* **1994**, *49*, 3835–3851.

[97]   M. Tuckerman, K. Laasonen, M. Sprik, M. Parrinello, *J. Phys. Chem.* **1995**, *99*, 5749–5752.

[98]   S. J. Paddison, D. W. Reagor, T. A. Zawodzinski Jr, *J. Electroanal. Chem.* **1998**, *459*, 91–97.

[99]   N. Agmon, *Chem. Phys. Lett.* **1995**, *244*, 456–462.

[100]   S. Slade, S. A. Campbell, T. R. Ralph, F. C. Walsh, *J. Electrochem. Soc.* **2002**, *149*, A1556.

[101]   E. L. Thompson, T. W. Capehart, T. J. Fuller, J. Jorne, *J. Electrochem. Soc.* **2006**, *153*, A2351.

[102]   T. H. M. Pham, J. Zhang, M. Li, T.-H. Shen, Y. Ko, V. Tileli, W. Luo, A. Züttel, *Adv. Energy Mater.* **2022**, *12*, 2103663.

[103]   G.-F. Li, D. Yang, P.-Y. Abel Chuang, *ACS Catal.* **2018**, *8*, 11688–11698.

[104]   S. A. Berlinger, B. D. McCloskey, A. Z. Weber, *J. Phys. Chem. B* **2018**, *122*, 7790–7796.

[105]   A. Tarokh, K. Karan, S. Ponnurangam, *Macromolecules* **2020**, *53*, 288–301.

[106]   G. de A. F. Pelayo, D. Cao-Thang, O. Adnan, W. Joshua, M. Christopher, K. A. R, N. Dae-Hyun, G. Christine, S. Ali, W. Xue, L. Y. C, L. Fengwang, E. Jonathan, R. L. J, T. S. J, S. David, E. H. Sargent, *Science* **2020**, *367*, 661–666.

[107]   I. Grigioni, L. K. Sagar, Y. C. Li, G. Lee, Y. Yan, K. Bertens, R. K. Miao, X. Wang, J. Abed, D. H. Won, F. P. García de Arquer, A. H. Ip, D. Sinton, E. H. Sargent, *ACS Energy Lett.* **2021**, *6*, 79–84.

[108]   N. Han, M. Sun, Y. Zhou, J. Xu, C. Cheng, R. Zhou, L. Zhang, J. Luo, B. Huang, Y. Li, *Adv. Mater.* **2021**, *33*, 2005821.

[109]   T. Möller, F. Scholten, T. N. Thanh, I. Sinev, J. Timoshenko, X. Wang, Z. Jovanov, M. Gliech, B. Roldan Cuenya, A. S. Varela, P. Strasser, *Angew. Chem. Int. Ed.* **2020**, *59*, 17974–17983.

[110]   C. Yang, B. H. Ko, S. Hwang, Z. Liu, Y. Yao, W. Luc, M. Cui, A. S. Malkani, T. Li, X. Wang, J. Dai, B. Xu, G. Wang, D. Su, F. Jiao, L. Hu, *Sci. Adv.* **2022**, *6*, eaaz6844.

[111]   R. Xia, S. Zhang, X. Ma, F. Jiao, *J. Mater. Chem. A* **2020**, *8*, 15884–15890.

[112]   W. Luc, B. H. Ko, S. Kattel, S. Li, D. Su, J. G. Chen, F. Jiao, *J. Am. Chem. Soc.* **2019**, *141*, 9902–9909.

[113]   W. Luc, X. Fu, J. Shi, J.-J. Lv, M. Jouny, B. H. Ko, Y. Xu, Q. Tu, X. Hu, J. Wu, Q. Yue, Y. Liu, F. Jiao, Y. Kang, *Nat. Catal.* **2019**, *2*, 423–430.

[114]   M. Jouny, W. Luc, F. Jiao, *Nat. Catal.* **2018**, *1*, 748–755.

[115]   W. Luc, C. Collins, S. Wang, H. Xin, K. He, Y. Kang, F. Jiao, *J. Am. Chem. Soc.* **2017**, *139*, 1885–1893.

[116]   W. Ma, S. Xie, T. Liu, Q. Fan, J. Ye, F. Sun, Z. Jiang, Q. Zhang, J. Cheng, Y. Wang, *Nat. Catal.* **2020**, *3*, 478–487.

[117]   W. Ma, S. Xie, X.-G. Zhang, F. Sun, J. Kang, Z. Jiang, Q. Zhang, D.-Y. Wu, Y. Wang, *Nat. Commun.* **2019**, *10*, 892.

[118]   Z. Tao, Z. Wu, Y. Wu, H. Wang, *ACS Catal.* **2020**, *10*, 9271–9275.

[119]   Y. Wu, Z. Jiang, X. Lu, Y. Liang, H. Wang, *Nature* **2019**, *575*, 639–642.

[120]   Z. Weng, Y. Wu, M. Wang, J. Jiang, K. Yang, S. Huo, X.-F. Wang, Q. Ma, G. W. Brudvig, V. S. Batista, Y. Liang, Z. Feng, H. Wang, *Nat. Commun.* **2018**, *9*, 415.

[121]   D. Wu, C. Dong, D. Wu, J. Fu, H. Liu, S. Hu, Z. Jiang, S. Z. Qiao, X.-W. Du, *J. Mater. Chem. A* **2018**, *6*, 9373–9377.

[122] H. Li, P. Yu, R. Lei, F. Yang, P. Wen, X. Ma, G. Zeng, J. Guo, F. M. Toma, Y. Qiu, S. M. Geyer, X. Wang, T. Cheng, W. S. Drisdell, *Angew. Chem. Int. Ed.* **2021**, *60*, 24838–24843.

[123] C. Choi, S. Kwon, T. Cheng, M. Xu, P. Tieu, C. Lee, J. Cai, H. M. Lee, X. Pan, X. Duan, W. A. Goddard, Y. Huang, *Nat. Catal.* **2020**, *3*, 804–812.

[124] D. M. Koshy, S. Chen, D. U. Lee, M. B. Stevens, A. M. Abdellah, S. M. Dull, G. Chen, D. Nordlund, A. Gallo, C. Hahn, D. C. Higgins, Z. Bao, T. F. Jaramillo, *Angew. Chem. Int. Ed.* **2020**, *59*, 4043–4050.

[125] T. Möller, F. Scholten, T. N. Thanh, I. Sinev, J. Timoshenko, X. Wang, Z. Jovanov, M. Gliech, B. Roldan Cuenya, A. S. Varela, *Angew. Chem. Int. Ed.* **2020**, *132*, 18130–18139.

[126] Q. Lu, J. Rosen, Y. Zhou, G. S. Hutchings, Y. C. Kimmel, J. G. Chen, F. Jiao, *Nat. Commun.* **2014**, *5*, 3242.

[127] D. Wu, C. Dong, D. Wu, J. Fu, H. Liu, S. Hu, Z. Jiang, S. Z. Qiao, X.-W. Du, *J. Mater. Chem. A* **2018**, *6*, 9373–9377.

[128] T. J. Zimudzi, M. A. Hickner, *ACS Macro. Lett.* **2016**, *5*, 83–87.

[129] M. Tesfaye, D. I. Kushner, A. Kusoglu, *ACS Appl. Polym. Mater.* **2019**, *1*, 631–635.

[130] T. Li, *Joule* **2020**, *4*, 980–982.

[131] Y. Lum, J. W. Ager, *Nat. Catal.* **2019**, *2*, 86–93.

[132] Y. Lum, B. Yue, P. Lobaccaro, A. T. Bell, J. W. Ager, *J. Phys. Chem. C* **2017**, *121*, 14191–14203.

[133] Y. Lum, J. W. Ager, *Angew. Chem. Int. Ed.* **2018**, *57*, 551–554.

[134] M. v Martínez de Yuso, L. A. Neves, I. M. Coelhoso, J. G. Crespo, J. Benavente, E. Rodríguez-Castellón, *Fuel Cells* **2012**, *12*, 606–613.

[135] P. Grosse, A. Yoon, C. Rettenmaier, A. Herzog, S. W. Chee, B. Roldan Cuenya, *Nat. Commun.* **2021**, *12*, 6736.

[136] R. E. Zeebe, *Geochim Cosmochim Acta* **2011**, *75*, 2483–2498.

[137] J. C. Bui, C. Kim, A. Z. Weber, A. T. Bell, *ACS Energy Lett.* **2021**, *6*, 1181–1188.

[138] X. Ren, T. D. Myles, K. N. Grew, W. K. S. Chiu, *J. Electrochem. Soc.* **2015**, *162*, F1221.

[139] C. Zhan, F. Dattila, C. Rettenmaier, A. Bergmann, S. Kühl, R. García-Muelas, N. López, B. R. Cuenya, *ACS Catal.* **2021**, *11*, 7694–7701.

[140] S. Jiang, K. Klingan, C. Pasquini, H. Dau, *J. Chem. Phys.* **2018**, *150*, 041718.

[141] M. Moradzaman, G. Mul, *ChemElectroChem* **2021**, *8*, 1478–1485.

[142] J. de Ruiter, H. An, L. Wu, Z. Gijsberg, S. Yang, T. Hartman, B. M. Weckhuysen, W. van der Stam, *J. Am. Chem. Soc.* **2022**, *144*, 15047–15058.

[143] H. An, L. Wu, L. D. B. Mandemaker, S. Yang, J. de Ruiter, J. H. J. Wijten, J. C. L. Janssens, T. Hartman, W. van der Stam, B. M. Weckhuysen, *Angew. Chem. Int. Ed.* **2021**, *60*, 16576–16584.

[144] Y. Zhao, X. Chang, A. S. Malkani, X. Yang, L. Thompson, F. Jiao, B. Xu, *J. Am. Chem. Soc.* **2020**, *142*, 9735–9743.

[145] G. Niaura, *Electrochim. Acta* **2000**, *45*, 3507–3519.

[146] J. Gao, H. Zhang, X. Guo, J. Luo, S. M. Zakeeruddin, D. Ren, M. Grätzel, *J. Am. Chem. Soc.* **2019**, *141*, 18704–18714.

[147] D. Quéré, *Annu. Rev. Mater. Res.* **2008**, *38*, 71–99.

[148] A. S. Varela, M. Kroschel, T. Reier, P. Strasser, *Catal. Today* **2016**, *260*, 8–13.

[149] X. Liu, P. Schlexer, J. Xiao, Y. Ji, L. Wang, R. B. Sandberg, M. Tang, K. S. Brown, H. Peng, S. Ringe, C. Hahn, T. F. Jaramillo, J. K. Nørskov, K. Chan, *Nat. Commun.* **2019**, *10*, 32.

[150] H. Jung, S. Y. Lee, C. W. Lee, M. K. Cho, D. H. Won, C. Kim, H.-S. Oh, B. K. Min, Y. J. Hwang, *J. Am. Chem. Soc.* **2019**, *141*, 4624–4633.

[151] A. Murata, Y. Hori, *Bull. Chem. Soc. Jpn.* **1991**, *64*, 123–127.

[152] Y. Lum, B. Yue, P. Lobaccaro, A. T. Bell, J. W. Ager, *J. Phys. Chem. C* **2017**, *121*, 14191–14203.

[153] H. Mistry, A. S. Varela, C. S. Bonifacio, I. Zegkinoglou, I. Sinev, Y.-W. Choi, K. Kisslinger, E. A. Stach, J. C. Yang, P. Strasser, B. R. Cuenya, *Nat. Commun.* **2016**, *7*, 12123.

[154] A. Zahid, A. Shah, I. Shah, *Nanomaterials* **2022**, *12*, 1380.

[155] J. Kim, W. Choi, J. W. Park, C. Kim, M. Kim, H. Song, *J. Am. Chem. Soc.* **2019**, *141*, 6986–6994.

[156] A. D. Handoko, C. W. Ong, Y. Huang, Z. G. Lee, L. Lin, G. B. Panetti, B. S. Yeo, *J. Phys. Chem. C* **2016**, *120*, 20058–20067.

[157] D. Kim, C. S. Kley, Y. Li, P. Yang, *Proc. Natl. Acad. Sci.* **2017**, *114*, 10560–10565.

[158] D. Gao, I. Zegkinoglou, N. J. Divins, F. Scholten, I. Sinev, P. Grosse, B. Roldan Cuenya, *ACS Nano* **2017**, *11*, 4825–4831.

[159] Y. Zhou, F. Che, M. Liu, C. Zou, Z. Liang, P. de Luna, H. Yuan, J. Li, Z. Wang, H. Xie, H. Li, P. Chen, E. Bladt, R. Quintero-Bermudez, T.-K. Sham, S. Bals, J. Hofkens, D. Sinton, G. Chen, E. H. Sargent, *Nat. Chem.* **2018**, *10*, 974–980.

[160] B. Zhang, J. Zhang, M. Hua, Q. Wan, Z. Su, X. Tan, L. Liu, F. Zhang, G. Chen, D. Tan, X. Cheng, B. Han, L. Zheng, G. Mo, *J. Am. Chem. Soc.* **2020**, *142*, 13606–13613.

[161] R. Duan, L. Luo, W. Qin, X. Xiao, R. Zhou, Z. Zheng, *J. Phys. Chem. C* **2022**, *126*, 20878–20885.

[162] X. K. Lu, B. Lu, H. Li, K. Lim, L. C. Seitz, *ACS Catal.* **2022**, *12*, 6663–6671.

[163] J.-J. Velasco-Velez, R. v Mom, L.-E. Sandoval-Diaz, L. J. Falling, C.-H. Chuang, D. Gao, T. E. Jones, Q. Zhu, R. Arrigo, B. Roldan Cuenya, A. Knop-Gericke, T. Lunkenbein, R. Schlögl, *ACS Energy Lett.* **2020**, *5*, 2106–2111.

[164] R. Bogue, *Industrial Robot: An International Journal* **2012**.

[165] A. Mistry, A. A. Franco, S. J. Cooper, S. A. Roberts, V. Viswanathan, *ACS Energy Lett.* **2021**, *6*, 1422–1431.

[166] A. Hexemer, P. Müller-Buschbaum, *IUCrJ* **2015**, *2*, 106–125.

[167] A. Buffet, A. Rothkirch, R. Döhrmann, V. Körstgens, M. M. Abul Kashem, J. Perlich, G. Herzog, M. Schwartzkopf, R. Gehrke, P. Müller-Buschbaum, S. v Roth, *J. Synchrotron Radiat.* **2012**, *19*, 647–653.

[168] G. Benecke, W. Wagermaier, C. Li, M. Schwartzkopf, G. Flucke, R. Hoerth, I. Zizak, M. Burghammer, E. Metwalli, P. Müller-Buschbaum, M. Trebbin, S. Foerster, O. Paris, S. v Roth, P. Fratzl, *J. Appl. Crystallogr.* **2014**, *47*, 1797–1803.

[169] J. Liu, D. Zhang, D. Yu, M. Ren, J. Xu, *Light Sci. Appl.* **2021**, *10*, 55.

[170] B. Campanella, V. Palleschi, S. Legnaioli, *ChemTexts* **2021**, *7*, 1–21.

List of publications

1. **Pan Ding**, Philipp Zellner, Tim Rieth, Johannes Dittloff, Jianyong Gao, Ian D. Sharp* "Tailoring Nafion/solvent formulations for enhanced electrocatalytic CO_2 reduction to multicarbon products.", **2023**, in preparation.

2. **Pan Ding**, Hongyu An, Philipp Zellner, Tianfu Guan, Jianyong Gao, Peter Müller-Buschbaum, Bert M. Weckhuysen*, Ward van der Stam, Ian D. Sharp* "Elucidating the roles of Nafion/solvent formulations in copper-catalyzed CO_2 electrolysis" *ACS Catalysis*, **2023**, doi.org/10.1021/acscatal.2c05235.

   Note: The majority data of Chapter 4 and all data of Chapter 5 are adapted from this publication.

3. **Pan Ding**, Tianhao Jiang, Nan Han, Yanguang Li* "Photocathode engineering for efficient photoelectrochemical CO_2 reduction" *Materials Today Nano*, **2020**, 10, 100077.

Acknowledgement

I also acknowledge:

- Prof. Ian D. Sharp for supervision of my PhD work and valuable suggestions.

- Financial support from China Scholarship Council (CSC).

- Joana Figueiredo, our secretary, for her extensive administrative support and extreme kindness and patiencience in every minor paper work.

- Prof. Bert M. Weckhuysen, Prof. Ward van der Stam, Dr. Hongyu An, Jim de Ruiter, Hui Wang, Jiaorong Yan and Shuang Yang from Utrecht University in the Netherlands for their help with Raman spectroscopy and experiments in the lab.

- Prof. Peter Müller-Buschbaum and Tianfu Guan for X-ray scattering tests.

2023.07

Garching bei München, Deutschland